

POLITECNICO DI TORINO

Corso di Laurea Magistrale
in Ingegneria Aerospaziale e Astronautica



Tesi di Laurea Magistrale

Experimental Investigation of a Single-Element Rocket Combustor operating with LOX/CH₄ and LOX/H₂

Relatore

Prof. Dario Giuseppe Pastrone

Co-Relatori

M. Sc. Nikolas Perakis

Prof. Dr.-Ing. Oskar J. Haidn

Candidata

Maria Sofia Di Rocco

Aprile 2020

Abstract

The aim of this work developed during a six months period at Technische Universität München is to investigate the combustion process in a single-element square combustion chamber which mainly operates with LOX/CH₄. For this thesis purpose a liquid oxygen supply line has been built and integrated with MoRaP facility.

A Cold Flow tests campaign with liquid oxygen has been performed to set the proper pressure during the following Hot Fire tests.

Although the shear coaxial injector element is specifically designed for oxygen/methane combination, a Hot Fire test campaign with gaseous hydrogen as fuel has been additionally performed to compare the different chemical timescales and the heat flux values.

In Chapter 3 the previous campaigns with GOX/GCH₄ are briefly summarized and compared. In Section 3.6 the LOX supply line upgrade within MoRaP is presented in details. The experimental procedure for operating the tests and the necessary pressure calculations are described in Chapter 5. The collected data have been analysed thanks to pressure and temperature sensors placed within the supply line and the combustion chamber.

The results for both fuels campaigns are presented in Chapter 6 in terms of pressure and temperature distribution over time and along chamber axis. In addition, the injector pressure drop is investigated as well as the obtained mass flow rates of liquid oxygen and fuel.

The tests have been performed for different load points, namely different combination of nominal chamber pressure and oxidizer to fuel ratio.

In order to ensure a long life to the optical glass window, a Hot Fire test campaign with copper window has been previously performed. Afterwards, an optical diagnostic via Chemiluminescence analysis has been carried out during the Hot Fire tests campaign with glass window. While running Hot Fire test campaign with glass window, a shorter burning time and a longer time delay between two consecutive tests have been adopted.

Therefore dealing with an experimental thesis lead one to face with delivery time of parts, after having ensured funds availability, as well as material deterioration, chamber and line leakages, geometry uncertainties, damaged equipment and possibly breaking of components.

Acknowledgement

First of all I would like to thank Professor Dario Giuseppe Pastrone for having been feeding my interest in propulsion science since the third year of Bachelor Degree in Aerospace Engineering and for giving me the opportunity to carry out my Master Thesis benefiting the *Thesis under request* project provided by Politecnico di Torino.

Thanks to Prof. Dr.-Ing. Oskar J. Haidn for welcoming me at the LTF of the Technische Universität München, for allowing me to face an experimental research without any previous experience and for being available to discuss each encountered problem.

A special thanks goes to Nikolas Perakis: without him, this work would not have even started. I would like to thank him for his patience and clarity in resolving any doubts and for the dedication to this project, up to sacrifice his weekends. He inspired me in always asking myself critical questions and in solving problems in the most efficient way.

I would also like to thank Christoph von Sethe who provided us with all the parts we needed and mostly with his experience in LOX/methane combustion. I value his keen enthusiasm for any successful ignition as well as his musical tastes.

I'm grateful to Samuel, Samuele and Simona, the closest new friends who shared with me the last six-months experience in München. Every day spent in Garching has been unique.

Thanks to my friends from Politecnico di Torino: Elena, Ludo, Poggio, Rebi, Salvo and Tommi. Without them all, I would probably have lost my determination.

Thanks for my long life friends Catta, Chiara, Chiaretta, Eleonora, Elisa, Giorgio, Manu, Marghe, Paolo and Sara for always being present and supportive.

Thanks to Francesco, for always being by my side.

Finally, I express my gratitude to my family for their support during my university course of study, especially during the periods abroad. The accomplishment of this work would not have been possible without them.

Thank you all, for the t(h)rust you gave me.

Contents

1	Introduction	17
2	Definitions and fundamentals	19
2.1	Performance definitions	19
2.2	Characteristic parameters and non-dimensional parameters	21
2.2.1	Characteristic Length	21
2.2.2	Non-dimensional parameters	21
2.3	LOX/LH2 propellants combination	22
2.4	Green propellants	22
2.4.1	Toxicity	22
2.4.2	Applications	23
2.4.3	Performance	23
2.5	OF ratio choice	26
2.5.1	LOX/CH4 combustion	26
2.5.2	LOX/H2 combustion	28
2.6	Shear coaxial injector	29
2.7	Flammability limit	31
2.8	Flame instability	31
2.9	Combustion process	32
3	Experimental Setup	33
3.1	Previous experimental campaigns	33
3.1.1	Comparison methodology	34
3.1.2	Single element GOX/GCH4 square combustion chamber	34
3.1.3	Single element GOX/GCH4 round combustion chamber	34
3.1.4	Comparison of a square and round single element GOX/GCH4 combustion chamber	35
3.1.5	Multi-injector GOX/GCH4 rectangular combustion chamber	36
3.1.6	Comparison of a single and multi-injector GOX-GCH4 rectangular combustion chamber	36
3.1.7	Multi-injector GOX/GCH4 round combustion chamber	36
3.2	MoRaP	38
3.2.1	MoRaP: GOX supply line	38
3.2.2	MoRaP: square combustion chamber	40
3.3	Measurement set up	41
3.3.1	Pressure Transducers	41
3.3.2	Thermocouples	41
3.4	Optical set up	43
3.4.1	ICCD Camera	43
3.5	Cold Flow Test Campaign Preparing	44
3.5.1	LOX supply line assembly	44
3.5.2	Pressure sensors calibration	44
3.5.3	Leakage Test before Cold Flow Test	44
3.5.4	Insulation for Cryogenic line	44
3.6	LOX supply line	44

3.6.1	Venturi meter	47
3.6.2	Venturi geometry optimization	47
3.7	Hot Flow Test Campaign Preparing	49
3.7.1	Combustion Chamber mounting	49
3.7.2	Thermocouples mounting	49
3.7.3	Pressure sensors mounting	49
3.7.4	Copper window positioning	49
3.7.5	Glass window positioning	49
3.7.6	Leakage Test before Hot Flow Test	49
4	Methods of Evaluation	51
4.1	Reference system	51
4.2	Auswertung routine	52
4.2.1	Fuel and Film Mass flow rate calculations	53
4.2.2	c_{th}^* calculation via CEA	53
4.3	Inverse Heat Transfer Method	55
4.4	Optical methods of evaluation	56
4.4.1	Radiation	56
4.4.2	Chemiluminescence Imaging	56
4.4.3	Averaged Images Routine	57
4.4.4	Abel Transform	58
4.4.5	Abel Transform Routine	59
5	Operating Conditions	61
5.1	Cold Flow Test Campaign	61
5.1.1	Cold Flow Evaluation	61
5.1.2	Cold Flow Procedure	63
5.2	Hot Fire Test Campaign LOX/CH4	64
5.2.1	Load Points	64
5.2.2	Igniter load point	65
5.3	Hot Fire Test Campaign LOX/GH2	65
5.3.1	Load Points	65
5.3.2	Igniter load point	65
5.3.3	Hot Fire Test Procedure	66
6	Results and Analysis	67
6.1	Cold Flow Test	67
6.2	Hot Fire Test Campaign LOX/CH4 with copper window	70
6.2.1	Pressure setting	70
6.2.2	Liquifier tanks measurements	71
6.2.3	Chamber temperature and pressure distribution	71
6.2.4	Chamber pressure and temperature distribution over length	72
6.2.5	Mass flow rate distribution	73
6.2.6	Film cooling pressure and temperature distribution	74
6.2.7	Oxidizer to fuel ratio	74
6.2.8	Heat flux distribution	75
6.2.9	Combustion efficiency η_{c^*}	77
6.3	Comparison among different OF ratios at same chamber pressure	78
6.3.1	Theoretical and experimental result	78
6.3.2	Velocity Ratio	78
6.3.3	Heat flux comparison	79
6.4	Hot Fire Test Campaign LOX/GH2 with copper window	80
6.4.1	Pressure setting	80
6.4.2	Chamber temperature and pressure distribution	81
6.4.3	Chamber temperature and pressure distribution over length	81
6.4.4	Mass flow rate distribution	82
6.4.5	Oxidizer to fuel ratio	82
6.4.6	Injector pressure drop	83

6.4.7	Heat flux distribution	84
6.4.8	Combustion efficiency η_{c^*}	85
6.5	Comparison among different OF ratios at same chamber pressure	86
6.5.1	Theoretical and experimental result	86
6.5.2	Velocity Ratio	86
6.5.3	Heat flux comparison	87
6.6	Hot Fire Test Campaign LOX/CH4 with glass window and Panasonic camera	88
6.7	Hot Fire Test Campaign LOX/CH4 with glass window and FlameStar2 camera	90
6.7.1	Chemiluminesce Technique	90
6.7.2	Abel Inverse Transform	94
6.7.3	OF comparison	95
6.8	Hot Fire results over Cold Flow curve	96
7	Conclusions	97
A	Uncertainty Analysis	99
A.0.1	Venturi mass flow rate uncertainty	99
A.0.2	OF uncertainty	100
A.1	MoRaP	101
A.2	Thrust chamber components	102
A.3	Calibration	104
A.4	Windows	105
A.5	LOX supply line components	108
A.6	Complete Cold Flow Set Up	110
A.7	Cold Flow Test Operating	111
A.8	Hot Fire	112
A.9	Optical Set Up	113
B	Measurement Set Up	115
B.1	Thermocouples	115
B.2	Pressure sensor distribution	116
B.3	Window Set up	116

List of Figures

2.1	Theoretical mass specific vacuum impulse as a function of OF ratios for various hydrocarbon propellants and for LOX/LH2.	23
2.2	Properties of combustion products at combustion chamber end section varying OF at $p_c = 20 \text{ bar}$, $\epsilon_c = 2.5$	26
2.3	Gibbs free energy of combustion products varying OF.	27
2.4	Properties of combustion products at chamber end section varying OF at $p_c = 20 \text{ bar}$, $\epsilon_c = 2.5$	28
2.5	Density specific impulse at sea level and effective exhaust velocity at $p_c = 20 \text{ bar}$, $\epsilon_c = 2.5$	28
2.6	Shear coaxial injector.	29
3.1	MoRaP facility assembly with rectangular thrust chamber.	38
3.2	MoRaP Fluid Plan with gaseous methane and gaseous oxygen.	39
3.3	Single injector element configuration for LOX/GCH4 propellants combination.	40
3.4	Top view of single element square combustion chamber with mounted window and igniter. Christoph von Sethe's Semester thesis (2016).	41
3.5	Top view of pressure sensors set up. Christoph von Sethe (2019).	42
3.6	Side view of thermocouples set up - Detail 2:1 scale of thermocouples at injection section. Christoph von Sethe's Semester thesis (2016)	42
3.7	Side view of the single element square combustion chamber complete assembly with window and igniter positioned at middle section. Christoph von Sethe's Semester thesis (2016).	42
3.8	Optical setup schematics for OH* emission imaging.	43
3.9	MoRaP Fluid Plan with gaseous methane and liquid oxygen.	45
3.10	Cold Flow evaluation for Venturi and turbine mass flow rate versus tank pressure relative to ambient pressure plotted with uncertainties	48
3.11	Parametric study for optimization of Venturi geometry	48
4.1	Reference system of the combustion chamber.	51
4.2	Schematics of rocket combustion chamber cross section. (a) Finite-area combustion chamber. (b) Infinite-area combustion chamber. - Gordon [1],1994	55
4.3	Inverse Heat Transfer Method iteration steps.	55
4.4	Image post-processing steps.	59
5.1	Liquid oxygen mass flow rate points over tank pressure relative to the ambient pressure	62
5.2	Liquid oxygen mass flow rate curve over tank pressure relative to the ambient pressure.	62
6.1	Temperature and pressure profile through the MVLOX valve	68
6.2	Saturation pressure curve for oxygen.	69
6.3	Liquid oxygen mass flow rate measured by Venturi meter during testing time.	69
6.4	Combustion chamber measurements versus running time.	71
6.5	Normalized pressure and temperature profile along chamber axis.	72
6.6	Mass flow rates	73
6.7	Pressure profile over testing time with DO signals.	73
6.8	Pressure and temperature measurements upstream and downstream nitrogen orifice.	74
6.9	Oxidizer to fuel ratio during burning time.	74
6.10	Heat flux and heat release profile over time.	75

6.11	Heat flux profile over length for different film cooling percentage.	76
6.12	Temperature footprint at combustion chamber end section for $t = 8.9$ s.	76
6.13	Signal registered by the dynamic pressure sensor for TMC-20-34-30-20-8 test.	77
6.14	Nominal and obtained mass flow rate over OF ratio at same chamber pressure $p_c = 20$ and 20 % of film cooling.	78
6.15	Heat flux over chamber length for different OF ratios and for different cooling percentages.	79
6.16	Combustion chamber measurements versus running time.	81
6.17	Normalized pressure and temperature profile along chamber axis.	81
6.18	Mass flow rates.	82
6.19	Oxidizer to fuel ratio during burning time.	82
6.20	Hydrogen pressure drop across the orifice and across the injector.	83
6.21	Heat flux and heat release profile over time.	84
6.22	Heat flux profile over length for different film cooling percentage.	84
6.23	Heat flux over chamber length comparison between H2 and CH4.	85
6.24	Nominal and obtained mass flow rate over OF ratio at same chamber pressure $p_c = 20$ and 20 % of film cooling.	86
6.25	Heat flux profile over length for different OF ratios.	87
6.26	Flame top view from glass window with Panasonic camera.	89
6.27	Raw images of flame emission captured by Flame Star 2 camera and OH* filter.	90
6.28	Raw image - Rotated image - Resized image.	91
6.29	Images obtained with <i>Image Processing</i> function AVERAGED IMAGES ROUTINE.	91
6.30	Images obtained with <i>Chemiluminesce</i> function in AVERAGED IMAGES ROUTINE.	92
6.31	Images obtained with <i>Chemiluminesce</i> function in AVERAGED IMAGES ROUTINE.	92
6.32	Mean brightness for several axial positions.	93
6.33	Visualization of the measured OH* emission.	94
6.34	3D visualization of the Abel inverse transform.	94
6.35	2D Abel inverse transform.	95
6.36	Flame OH* emission for different obtained OF ratios.	95
6.37	Heat flux profile over length for different film cooling percentage.	96
6.38	Injector pressure drop over LOX mass flow rate -Cold flow and Hot Fire - Comparison with previous tests performed by Christoph von Sethe.	96
A.1	MoRaP supply line: oxygen side.	101
A.2	Shear coaxial injector mounted with the injector head and faceplate during Cold Flow test.	102
A.3	Measurements set up configuration.	102
A.4	Igniter element and igniter switch.	103
A.5	Thermocouples type T.	103
A.6	Calibration facility.	104
A.7	Plug for pressurization.	104
A.8	Film applicator.	106
A.9	Window leakage.	106
A.10	Nozzle truncated trapezoidal prism.	107
A.11	Nozzle holding plate.	107
A.12	Venturi meter.	108
A.13	LN2 check valve.	108
A.14	Cold Flow complete set up.	110
A.15	Control room.	110
A.16	Experimental set up for oxygen liquification.	111
A.17	Experimental set up for precooling with LN2.	111
A.18	Hot Fire test LOX/CH4.	112
A.19	Hot Fire test LOX/H2.	112
A.20	Experimental set up for precooling with LN2.	113
B.1	Labview tool.	121
B.2	Calibration data file .txt: input to LabView.	121

List of Tables

2.1	Toxicity and Environmental Hazard Figure values for different type of liquid rocket propellants combination.	23
2.2	LOX-HC typical operating conditions.	24
2.3	Typical performance values for LOX/LCH4 and LOX/LH2.	24
2.4	Flammability limits for air-fuel mixture at atmospheric pressure.	31
3.1	Performance values for LOX/GCH4 and GOX/GCH4 propellants combinations calculated with CEA at $p_c = 20$ bar, OF=2.6, $\epsilon_c = 2.5$	33
3.2	Single element GOX/GCH4 square combustion chamber geometry.	34
3.3	Single element GOX/GCH4 round combustion chamber geometry.	34
3.4	Multi-injector GOX/GCH4 rectangular combustion chamber geometry.	36
3.5	Multi-injector GOX/GCH4 round combustion chamber geometry.	37
3.6	Combustion chamber geometry.	40
3.7	Single injector element geometry.	40
3.8	Oxygen line components.	46
3.9	Venturi meter geometry.	47
3.10	Venturi meter geometry after optimization.	48
5.1	Cold Flow evaluated tests without the combustion chamber.	61
5.2	Nominal load points for LOX/CH4 Test Campaign.	64
5.3	Nominal load point for spark torch igniter	65
5.4	Nominal load points for LOX/H2 Test Campaign.	65
5.5	Nominal load point for spark torch igniter for LOX/H2 Test Campaign.	65
6.1	Nominal load point for TMC-20-34-30-20-5 test.	70
6.2	Nominal mass flow and pressure values for TMC-20-34-30-20-5 test.	70
6.3	Ideal and obtained quantities for TMC-20-34-30-20-5 test at the evaluation time.	75
6.4	Combustion efficiency for test TMC-20-34-30-20-5.	77
6.5	Nominal and obtained velocity ratios for a sample of test performed at different OF ratios but same nominal chamber pressure $p_c = 20$ bar.	78
6.6	Nominal load point for THC-20-68-30-20-1 test.	80
6.7	Nominal mass flow and pressure values for THC-20-68-30-20-1 test.	80
6.8	Ideal and obtained quantities for THC-20-68-30-20-1 test at the evaluation time.	83
6.9	Combustion efficiency for test THC-20-68-30-20-1.	85
6.10	Nominal and obtained velocity ratios for a sample of test performed at different OF ratios but same nominal chamber pressure $p_c = 20$ bar.	86
6.11	Nominal load point for TMW-20-34-30-20-7 test with glass window.	88
6.12	Obtained mass flow, pressure and temperature values for TMW-20-34-25-20-7 test.	88
B.1	Type T thermocouples.	115
B.2	Type K thermocouples.	115
B.3	Thermocouples label.	115
B.4	Pressure sensors position within the combustion chamber.	116
B.5	Glass window specifications.	116
B.6	Graphite foils instruction for copper window.	116
B.7	Graphite foils instruction for glass window.	116

Nomenclature

Acronyms

CEA	Chemical Equilibrium with Applications
CET	Chemical Equilibrium with Transport Properties
CFD	Computational Fluid Dynamics
ESA	European Space Agency
FAC	Finite Area Combustor
GEO	Geostationary Earth Orbit
GH ₂	Gaseous Hydrogen
GOX	Gaseous Oxygen
HCH ₄	Gaseous Methane
ICCD	Intensified Charge Coupled Device
IHTM	Inverse Heat Transfer Method
JAXA	Japan Aerospace Exploration Agency
LOX	Liquid Oxygen
LFL	Lower Flammability Limit
LTF	Lehrstuhl für Turbomaschinen und Flugantriebe
MCP	Micro Channel Plate
MMH	Monomethyl Hydrazine
MoRaP	Mobiler Raketen Prüfstand
NASA	National Aeronautics and Space Administration
OF	Oxidizer to Fuel
OH*	Hydroxyl Radicals excited
RP1	Rocket Propellant/Refined Petroleum
TEHF	Toxicity and Environmental Hazard Figure
TUM	Technische Universität München
UFL	Upper Flammability Limit
VR	Velocity Ratio

Latin Symbols

A	Area	$[m^2]$
a	Sound speed	$[m/s]$
c	Exhaust velocity	$[m/s]$
c^*	Characteristic velocity	$[m/s]$
C_D	Discharge coefficient	$[-]$
c_p	Specific heat at constant pressure	$[J/kg \cdot K]$
d	Diameter	$[m]$
Da_I	First Damköhler group	$[-]$
Da_{III}	Third Damköhler group	$[-]$
F	Thrust	$[N]$
g_0	Standard acceleration of gravity	$[m/s^2]$
h	Enthalpy per unit of mass	$[J/kg]$
h	Height	$[m]$
I_s	Specific Impulse	$[s]$
I_t	Total Impulse	$[N \cdot s]$
J	Momentum flux ratio	$[-]$
k	Specific heat ratio	$[-]$
L^*	Characteristic length	$[m]$
M	Molar mass	$[kg/mol]$
M	Mach number	$[-]$
\dot{m}	Mass flow rate	$[kg/s]$
p	Pressure	$[bar]$
Pr	Prandtl number	$[-]$
Q	Heat release	$[W]$
\dot{q}	Heat flux	$[kW/m^2]$
r	Radius	$[m]$
R	Ideal gas constant	$[J/K \cdot mol]$
Re	Reynolds number	$[-]$
Sc	Schmidt number	$[-]$
t	Time	$[s]$
T	Temperature	$[K]$
u	Velocity	$[m/s]$
v	Velocity	$[m/s]$
V_c	Combustion chamber volume	$[m^3]$
w	Width	$[m]$
We	Weber number	$[-]$
x	Reference coordinate	$[m]$
y	Reference coordinate	$[m]$
z	Reference coordinate	$[m]$

Greek Symbols

α	Diffusivity	$[W/(m^2K)]$
β	Contraction diameter ratio	$[-]$
γ	Isentropic specific heat ratio	$[-]$
ϵ	Contraction area ratio	$[-]$
η_{c^*}	Combustion c^* efficiency	$[-]$
λ	Thermal conductivity	$[W/(mK)]$
μ	Dynamic viscosity	$[Pa \cdot s]$
ρ	Density	$[kg/m^3]$
σ	surface tension	$[N/m]$
τ^*	Characteristic resident time	$[s]$

Chapter 1

Introduction

Liquid propellant rocket engines persist as the foremost chemical rocket propulsion systems, from attitude control thrusters and landers applications to first stage engine for space launch vehicles [2]. Many research activities focus on reducing toxic propellant usage together with improving reliability, handling and performances of the propulsive system.

Green propellants such as LOX/CH₄ combination has been being recently considered as an alternative to toxic propellants and to high-cost production of liquid hydrogen.

The technological challenges linked to the aforementioned goals result in many efforts, such as redesigning injectors geometry and configuration, testing at higher pressure chamber, investigating different combination of mixture ratio and more effective cooling strategies.

To fulfill the gap of knowledge about combustion performance and heat release process linked to oxygen/methane combination, the LTF of the Technische Universität München (TUM) has been working experimentally and numerically since 2012. Four subscaled combustion chambers have been operated with gaseous methane and gaseous oxygen with different cross sectional areas and different number of injector elements at high chamber pressures. Injector geometry, contraction ratio, chamber nominal pressure and mixture ratio have been kept equal to carry out a comparative analysis.

An optical access has been subsequently added to the rectangular cross sectional chambers to perform an optical diagnostic of the flame: spreading angle may be hence detected and experimental results may be compared with numerical CFD simulations.

For this present work purpose the test facility has been upgraded to operate with liquid oxygen. Liquid oxygen has been produced in situ by means of a liquifier and injected into the chamber after having properly modified the supply line.

Chapter 2

Definitions and fundamentals

2.1 Performance definitions

The total impulse I_t is proportional to the total energy released by all the propellant and it is found from the thrust force F integrated over the time of its application t :

$$I_t = \int_0^t F dt \quad (2.1)$$

The specific impulse I_s is an important figure of merit of the performances of any rocket propulsion system as it represents the thrust per unit propellant weight flow rate. If the total propellant mass flow rate is \dot{m} and the standard acceleration of gravity is g_0 , then:

$$I_s = \frac{\int_0^t F dt}{g_0 \int_0^t \dot{m} dt} \quad (2.2)$$

For constant propellant mass flow \dot{m} , constant thrust F , Eq. (2.2) simplifies as follows:

$$I_s = \frac{F}{g_0 \dot{m}} \quad (2.3)$$

The effective exhaust velocity c represents an average of mass-equivalent velocity at which propellant is being ejected from the vehicle:

$$c = I_s g_0 = F / \dot{m} \quad (2.4)$$

Since c and I_s differ by the constant g_0 , either one can be used as a measure of rocket performance. The characteristic velocity c^* is used for comparing the relative performance of different propulsion systems and propellants, defined as follows:

$$c^* = \frac{p_1 A_t}{\dot{m}} \quad (2.5)$$

The characteristic velocity c^* is only a function of propellants characteristics and combustion chamber properties, independent of nozzle, while I_s and c remain functions of nozzle geometry [3]. If the following assumptions are valid:

1. The working fluid is an adiabatic flow and an homogeneous gas, both in composition and in thermodynamic properties, obeying the perfect gas law.
2. A frozen flow composition is established along each section of the combustion chamber.
3. The expansion is uniform and steady.

thus, a theoretical value of the characteristic velocity c_{th}^* is determined:

$$c_{th}^* = \sqrt{\frac{T_c R}{M \gamma} \left(\frac{\gamma + 1}{2} \right)^{\frac{\gamma + 1}{\gamma - 1}}} \quad (2.6)$$

It is a function of working fluids thermodynamic properties, namely the specific heats ratio γ , chamber temperature T_c and effective molecular mass M . Moreover T_c is related to the gas internal stagnation enthalpy, giving a measure of the energy content of the rocket gases, by:

$$\Delta h_t = \int_{T_0}^{T_t} C_p dT \quad (2.7)$$

For bipropellants, the mixture ratio OF defines the ratio at which the oxidizer and fuel flow are mixed in the chamber, thus the ratio of oxidizer mass flow rate \dot{m}_o to the fuel mass flow rate \dot{m}_f :

$$OF = \frac{\dot{m}_o}{\dot{m}_f} \quad (2.8)$$

In this present study only combustion chamber performance are investigated, thus nozzle-related performance as specific impulse, thrust and exhaust velocity will not be taken into account. The contraction ratio, namely A_c/A_{th} is the ratio between the combustion chamber cross section and the nozzle throat section, hence no divergent geometry parameters will be considered. Therefore characteristic velocity c^* and combustion efficiency η_{c^*} will be considered as relevant performance.

Due to imperfect mixing, chamber heat-loss and incomplete combustion, the realized rocket performance is less than that computed theoretically. This will be reflected in the rocket thrust, effective velocity c and characteristic velocity c^* .

The ratio between the measured characteristic velocity c^* and the theoretical characteristic velocity c_{th}^* results in the c^* -efficiency η_{c^*} , defined in Eq. (2.9), expressing the degree of completion of the combustion process to convert the internal mixture energy into high-pressure and high-temperature gases.

$$\eta_{c^*} = \frac{c^*}{c_{th}^*} \quad (2.9)$$

2.2 Characteristic parameters and non-dimensional parameters

2.2.1 Characteristic Length

The characteristic chamber length L^* is an important parameter for the design of the combustion chamber. It is defined as the ratio between the chamber volume V_c and the nozzle throat area A_{th} :

$$L^* = \frac{V_c}{A_{th}} \quad (2.10)$$

Since the characteristic length L^* is directly related to the chamber pressure p_c as in Eq. (2.11), generally for higher chamber pressure, the chemical kinetics, i.e the characteristic residence time τ^* , shows an improved behavior. Hence generally for higher chamber pressure, smaller combustion chambers may be designed.

$$L^* = \frac{V_c}{A_{th}} \propto \frac{m_c}{\rho_c} \propto \frac{p_c \tau^*}{\rho_c c^*} \quad (2.11)$$

Typical values of L^* for bipropellants ranges between 0.8 m and 3.0 m.

2.2.2 Non-dimensional parameters

In scaling of chemical reactor, similarity criteria have been adopted [4] for flow system with conductive heat transfer occurring to chamber walls.

$$Re = \frac{\rho u L}{\mu} \quad (2.12)$$

$$Pr = \frac{c_p \mu}{\lambda} \quad (2.13)$$

$$Sc = \frac{\mu}{\rho D} \quad (2.14)$$

$$M = \frac{v}{a} \quad (2.15)$$

$$Da_I = \frac{L}{u \tau_i} \quad (2.16)$$

$$Da_{III} = \frac{q' L}{u c_p T \tau_i} \quad (2.17)$$

Reynolds number Re is the ratio of inertial forces to viscous forces. Schmidt number Sc is defined as the ratio between the kinematic viscosity and mass diffusivity. Prandtl number Pr is the ratio of momentum diffusivity and thermal diffusivity. Mach number M is the ratio of flow velocity to the speed of sound. First Damköhler group Da_I is the ratio of characteristic flow time scale to the chemical time scale. Third Damköhler group Da_{III} is defined as the ratio of heat release by chemical reaction to the heat lost by convection.

2.3 LOX/LH2 propellants combination

LOX/LH2 propellants combination is considered as a reference for comparison with *Green propellants* due to the existing state of art of well know engines as Vulcain and HM7B. Due to its high specific impulse, the cryogenic combination of LOX/LH2 is one of the most widely used for transfers into orbit. However since this combination of propellants is not storable in space, it is not used for in-orbit operations.

Hydrogen when burned with oxygen gives high performances, as shown in Table 2.3, and it is an excellent regenerative coolant. The extremely low fuel density requires large fuel tanks, hence large vehicle volume, as well as the extremely low storage temperatures limit available materials for pumps, cooling jackets, tanks and piping. Vacuum jacket and insulating material have to be used to minimize hydrogen evaporation and line purging is need to avoid orifice plugging by liquid or solidified particles. The combustion products are mainly water vapour, though the ice formation at high altitude may impact atmospheric chemistry. Liquid hydrogen is used with liquid oxygen in the Ariane V and delta IV launch vehicles and upper stage engines developed in Japan, Russia and China.

Nevertheless, LOX/LH2 combination requires high costs in production and operational phases and H2 production is high energy consuming. H2 storage requires costly cooling technologies and hazardous operations.

2.4 Green propellants

The term *Green Propellants* refers to a family of propellants, be they liquid, solid, hybrid, mono or bi-propellant which promise benefits in terms of overall life-cycle cost reduction, here lower cost of access to space and reduction of environmental impact [5].

The main features characterizing a green propellant are listed below:

1. Low toxicity: reduced hazard of operation by safe handling, hence reduced safety precautions, and storage of non-toxic fluids.
2. Low pollution impact: reduced pollution of environment on ground such as launch sites, stage impact area test benches and production facilities as well as pollution of atmosphere and in space.
3. Good performance: both mass-specific and volume-specific.
4. Good storability and lower cooling effort.
5. Wide material compatibility.

The fulfill of the aforementioned criteria leads to low costs, thanks to the reduced complexity and reduced production and operational efforts.

2.4.1 Toxicity

The TEHF (Toxicity and Environmental Hazard Figure) is the figure of merit used to assess the toxicity of green propellants. It combines the severity of handling danger of the propellants and the necessary mass to fulfill a reference mission to GEO. With equal TEHF, storables were preferred to cryogenes.

In Table 2.1 it is clear that completely non-toxic bipropellants rely on LOX and hydrocarbons, though are mostly semi-cryogenic.

Hydrazines do not fulfill the toxicity criterion, though the TEHF is lower than hydrogen peroxide-based bipropellants.

Oxidizer	Fuel	TEHF	Notes
O_2	Hydrogen	0	semi-cryogenic
O_2	Methane	0	semi-cryogenic
O_2	Propane	0	semi-cryogenic
N_2O	Ethanol	0.03	earth storable
N_2O	Kerosene	0.09	earth storable
O_2	Ethanol	0.15	semi-cryogenic
O_2	Kerosene	0.19	semi-cryogenic
O_2	NH_3	0.60	semi-cryogenic
O_2	UDMH	3.62	semi-cryogenic
H_2O_2	Kerosene	4.58	earth storable
H_2O_2	Methane	4.66	earth storable
N_2O_4	MMH	26.26	earth storable

Table 2.1: Toxicity and Environmental Hazard Figure values for different type of liquid rocket propellants combination.

2.4.2 Applications

Choosing the suitable propellants combination, two range of application are considered:

1. High thrust for first and second stage of launch vehicles, as well as booster stages.
2. Low thrust for orbital transfer, orbital manoeuvring and reaction control of stages, planet ascent/descent.

Regarding the high thrust range, green propellants thanks to their high specific impulse and no toxic combustion production are of interest to replace solid propellants commonly used for boosters.

2.4.3 Performance

The theoretical vacuum impulse I_{vac} of several propellants combinations is plotted in Figure 2.1 shows methane, propane and kerosene as the best performing among hydrocarbon fuels.

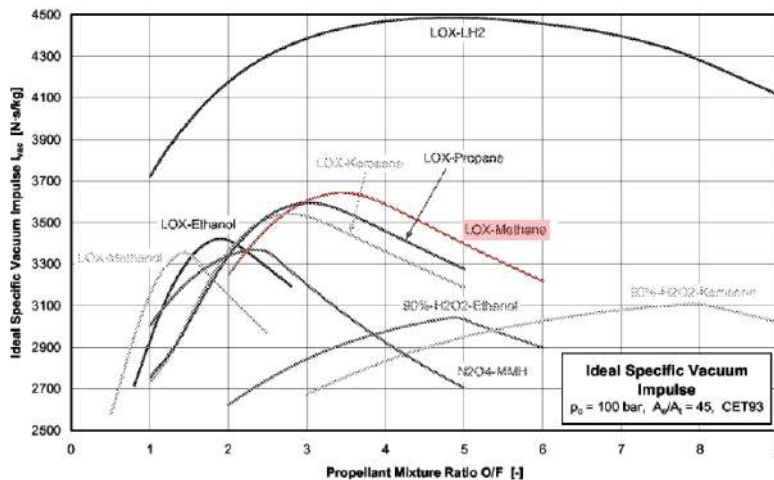


Figure 2.1: Theoretical mass specific vacuum impulse as a function of OF ratios for various hydrocarbon propellants and for LOX/LH2.

During the design phase, the injector element geometry has to be attentively considered since it has a strong impact on performance parameters.

Several types of injection elements for LOX-methane have been designed in the frame of TEHORA 2 research program in cooperation with CADB (Chemical Automatics Design Bureau) in Russia. Three injection element type were tested demonstrating successful and reliable ignition and operation, leading to efficiencies comparable to the experience from LOX-LH2 thrust chambers. A slight soot layer was observed which did not grow with increasing test duration and which could be easily cleaned.

The mixture ratio range of minimal carbon deposition and the resulting preburner temperature are given in Table 2.2. Hydrocarbons decompose above T_{coking} leading to a formation of a carbon layer which has an insulating effect reducing the heat transfer from the cooled chamber into the coolant increasing the temperature of the wall material. The maximum coolant-side wall temperature of 730 K for copper is below the coking limit of pure methane, thus coking is no limitation for methane cooling, which implies the lowest pressure loss for thrust chamber design with a copper liner.

The EADS (European Aeronautic defence and Space company) Germany subsidiary is focusing its Tehora program on liquid oxygen rocket engines to power the European Space Agency's next generation launcher, following studies into the use of methane as propellant [6].

	OF	T_{gas}	T_{coking}
	[-]	[K]	[K]
LOX-RP1	2.6-2.75	870-950	560-730
LOX-CH4	3.2-3.6	680-1170	980

Table 2.2: LOX-HC typical operating conditions.

The using of hydrocarbons, in particular methane instead of hydrogen, is now under consideration since the main advantages are the low operational costs and the much higher density than hydrogen, resulting in a lighter structure.

Studies have shown that, when burned with liquid oxygen, hydrocarbons such as RP-1 or methane give a small advantage in space launch vehicle fist stages: the higher density allows a less weighted vehicle and lower drag, which compensate for the for the lower specific impulse.

Oxidizer	Fuel	c^*	I_s
		[m/s]	[s]
Oxygen	Methane	1835	296
Oxygen	Hydrogen	2428	386

Table 2.3: Typical performance values for LOX/LCH4 and LOX/LH2.

The LOX/LCH4 propellant combination appears to be a good alternative to LOX/LH2 combination due to its good performance when compared to others hydrocarbons [7], such as an higher specific impulse and higher thermal conductivity, as well as cooling capability, low viscosity and low soot formation.

Researches and testings have been performed by the NASA Propulsion and Cryogenic Advanced Development (PCAD) [8] demonstrating reliable ignition of the LOX/LCH4 engine over a wide range of inlet temperatures, with the purpose of being applicable to reaction control systems or lander spacecrafts.

JAXA conducted experiments on LOX/GCH4 rocket engine for upper stage system of a middle class launch vehicle [9]. The new propellant combination brings new challenges and researches must be carried out on mixing process, flame anchoring and stability.

Within the ESA FLPP (Future Launcher Preparatory Programme), future reusable launch vehicles will require rocket engines with high performance capabilities, which are met by staged combustion cycle engines (as SSME and RD-0120).

However, european heritage is built on gas generator cycle, AS HM-7 and Vulcain family. Engines must be designed also for use over a large number of missions, implying long-life components development, as well as more robust turbomachinery and reusable igniters [10]. Reusability concept is linked to the demonstration of life limits both for low cycle and high cycle fatigue, along with scheduled maintenance, reduced operation costs and vehicle availability.

In order to acquire experience and knowledge on staged combustion cycle, the demonstrator will focus on LOX-methane propellants.

The technology development needs for bi-propellants mostly concern oxidizer issues as cryogenic storage for longer periods (e.g. Mars transfers) and ignition, that is replacing current electrical spark by alternatives, like laser catalytic, resonant igniter or additives to achieve hypergolicity.

2.5 OF ratio choice

2.5.1 LOX/CH4 combustion

Because of its particular molecular structure with large C-H bonds energies, methane exhibits some unique combustion characteristics such as high ignition temperature, low flame speed and low reactivity compared to other hydrocarbons. Methane kinetics are the most widely researched and most well understood, bringing on an optimized kinetic mechanism which considers 325 elementary reactions involving 53 species [11]. Stoichiometric OF ratio between oxygen and methane is equal to 4, as derivable from the chemical reaction in Eq. (2.18).



However the OF value is kept among 2.2-3.4 for different reasons.

First an oxygen rich mixture would lead to an undesired reaction between oxygen radicals and the copper molecules present in the wall chamber.

Secondly, a fuel rich mixture allows low molecular mass molecules of methane to remain unreacted. Thus the molecular mass of the reaction products is reduced and the characteristic velocity is increased (despite a small drop in combustion temperature T_c) according to Eq. (2.19).

$$c^* \propto \sqrt{\frac{T_c}{M}} \cdot \frac{1}{f(k)} \quad (2.19)$$

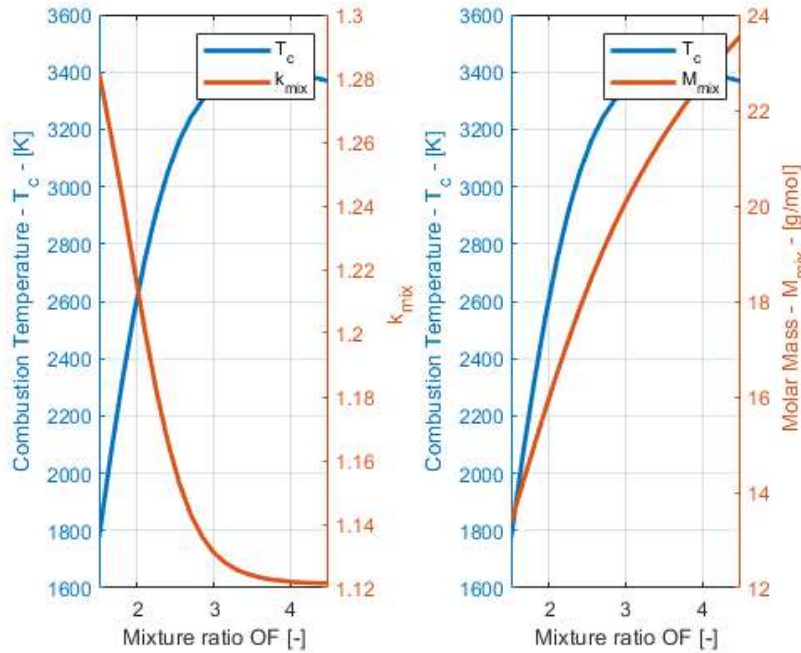


Figure 2.2: Properties of combustion products at combustion chamber end section varying OF at $p_c = 20bar$, $\epsilon_c = 2.5$

Furthermore, a fuel rich mixture provides available coolant for the chamber.

Among the disadvantages one may list the soot formation, although carbon-hydrogen bonds are weak compared to kerosene aromatic bond.

To calculate the theoretical combustion temperature T_c and the mixture molecular mass M , a macroscopic approach is adopted rather than focusing on the intermediate reactions. Gibbs criteria is based on minimizing the system's energy. Gibbs free energy is defined for a single specie i as in Eq. (2.20). It is related to the enthalpy h , temperature T , entropy S and determined as a function of two independent properties, here temperature and pressure.

$$G_i = h_i - T_i S_i \quad (2.20)$$

The change in free energy ΔG is defined as the difference between products chemical potential and reactants chemical potential:

$$\Delta G = \sum_i^m [(n_i(\Delta_f G^0)_i)]_{products} - \sum_i^r [(n_i(\Delta_f G^0)_i)]_{reactants} \quad (2.21)$$

where n_i is the molar concentration.

A curve of molar concentration n versus ΔG displays a minimum at equilibrium:

$$\left(\frac{d\Delta G}{dn} \right)_{eq} = 0 \quad (2.22)$$

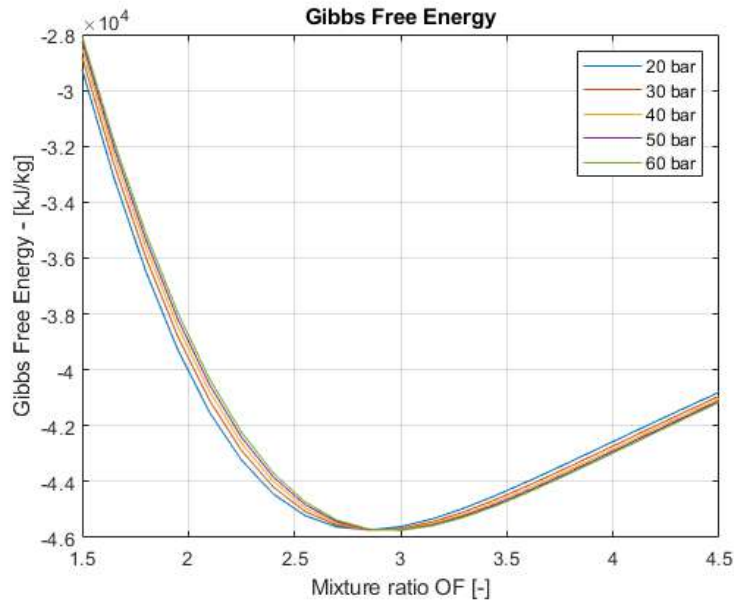


Figure 2.3: Gibbs free energy of combustion products varying OF.

Solving ¹ the Eq. (2.22) allows to determine the theoretical combustion temperature T_c and the properties of the combustion gases, here M_{mix} , $(C_p)_{mix}$, k_{mix} .

¹A Lagrangian multiplier, which represents the degree of completion of the reaction, is often used as described in detail by Gorgon-McBride [1].

2.5.2 LOX/H2 combustion

The aforementioned approach is applied to hydrogen and oxygen propellants combination as well. The chemical reaction for gaseous reactants and products is presented in Eq. (2.23): the stoichiometric OF ratio is equal to 8. However the best operative mixture ratio for high performances rocket engines ranges between 4.5 and 6.0.

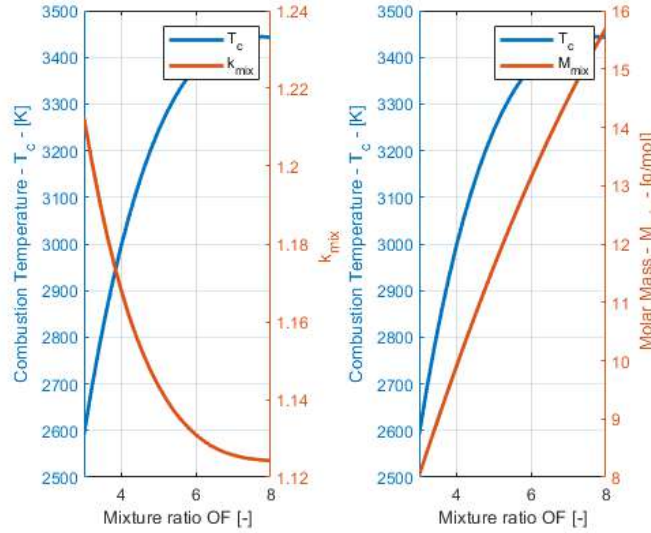


Figure 2.4: Properties of combustion products at chamber end section varying OF at $p_c = 20 \text{ bar}$, $\epsilon_c = 2.5$.

Focusing on combustion temperature profile T_c and on heat capacity ratio k_{mix} , the characteristic velocity, which in turns determine the minimum propellants consumption, has a maximum for OF equal to 4. However when hydrogen is used as fuel, the occupied volume has to be taken into account. Hence the density specific impulse I_{sp} is analyzed in Figure 2.5. The average density is defined as follows:

$$\rho = \frac{\rho_o \rho_f \cdot (1 + OF)}{OF \cdot \rho_f + \rho_o} \quad (2.24)$$

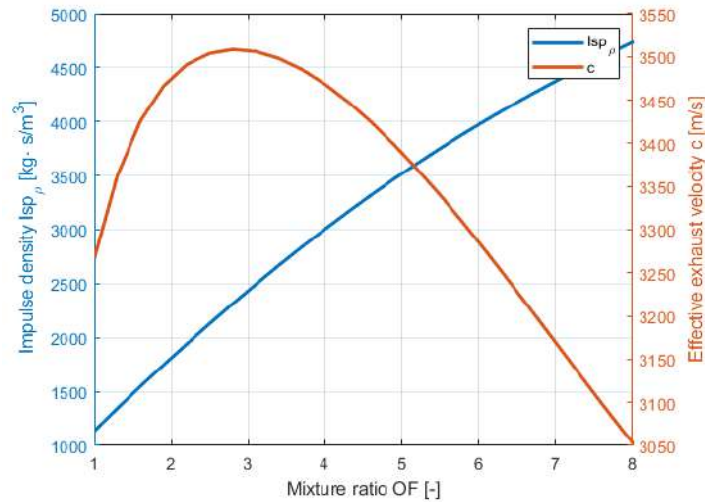


Figure 2.5: Density specific impulse at sea level and effective exhaust velocity at $p_c = 20 \text{ bar}$, $\epsilon_c = 2.5$.

2.6 Shear coaxial injector

Since the combustion performances and heat transfer characteristics are strongly influenced by injector geometry through its influence on the flame, flow dynamics and stability behaviour, the proper design is pivotal in the liquid rocket engine development.

Shear coaxial injector are commonly used in liquid rocket engine combustion chambers due to the efficient atomization and mixing mechanism which leads to high performances and stability [12].

Various other type of injector are usually used in liquid rocket engines, including centrifugal, impinging jet and shear coaxial [13].

The centrifugal injectors achieve the mixing process by swirling, whereas impinging injector implement stream collision between fuel and oxidizer. These type of injector are suitable for liquid-liquid combinations, however may present instability problems due to the backward flow and the unstable sheet shedding strands which in turn break up to forms droplets.

The shear coaxial injectors accomplish the mixing process through the shear-mixing of propellants. This configuration consists of an inner duct from which the oxygen is injected into the combustion chamber and an external coaxial duct from which the gaseous methane is expelled.

For the present aim, shear coaxial injectors are used due to the suitability for propellants with large density ratio, here liquid-gas interaction. This configuration is the also the most simplified one, allows a CFD modeling and simulations. The injector is designed specially for OX/GCH₄ combustion, therefore better performance are expected with respect to OX/GH₂ propellants combinations.

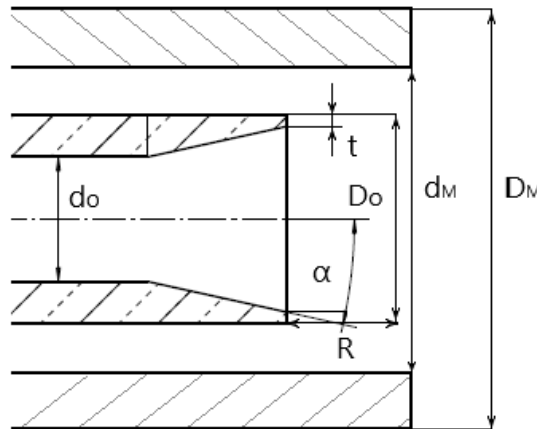


Figure 2.6: Shear coaxial injector.

In a coaxial injector the shear forces between the propellants determines the mixing efficiency and consequently the flow conditions and the flame behavior. In order to characterize the different operating points, non-dimensional quantities are employed. The velocity ratio VR is the ratio between the fuel and the oxidizer stream velocities, as in Eq. (2.25), giving a measure of the shear forces:

$$VR = \frac{v_{GCH_4}}{v_{GOX}} \quad (2.25)$$

The momentum flux ratio J is defined in Eq. (2.26):

$$J = \frac{(\rho v)_{GCH_4}}{(\rho v)_{GOX}} \quad (2.26)$$

Both the velocity ratio and the momentum flux ratio are based on propellants temperatures and pressure measurements at injection conditions.

Reynolds number and Weber number are the characteristic number applied for coaxial injector, giving respectively the ratio of inertial forces to viscous forces and the ratio of inertia to surface tension:

$$Re = \frac{\rho u d}{\mu} \quad (2.27)$$

$$We = \frac{\rho u^2 d}{\sigma} \quad (2.28)$$

Reynolds number is calculated both for fuel and oxidizer and Weber number characterizes the atomizing quality of a spray, if at least one of the propellant is in the liquid phase. Weber and Reynolds characteristic numbers are used to characterize the injector, here define the atomization regime and the turbulent regime respectively. The Weber number can be expressed as in Eq. (2.29), if the velocity of the liquid propellant is not negligible.

$$We = \frac{\rho(u_g - u_l)^2 d}{\sigma} \quad (2.29)$$

The mass flow rate for an incompressible flow, here liquid oxygen, through orifices is given by:

$$\dot{m} = C_d A \sqrt{2\rho\Delta p} \quad (2.30)$$

where C_d is a dimensionless discharge coefficient, ρ the propellant density, A the cross sectional area and Δp the pressure drop across the injector.

For a given pressure drop, injector elements usually establish mixture ratio. Using Eq. (2.8) and (2.30), the OF ratio becomes:

$$ROF = \frac{\dot{m}_o}{\dot{m}_f} = \frac{(C_d)_o A_o}{(C_d)_f A_f} \sqrt{\frac{\rho_o (\Delta p)_o}{\rho_f (\Delta p)_f}} \quad (2.31)$$

Recalling Eq. (2.30), the injection velocity is given by:

$$v = C_d \sqrt{2\Delta p/\rho} \quad (2.32)$$

2.7 Flammability limit

With hydrogen fuel the flame anchors properly at the injector exit and flame stabilization occurs during the steady state phase of combustion [14].

For LOX/CH₄ combustion the flame behaviour is influenced by injection conditions. Indeed, methane flame can be anchored or detached for subcritical ² conditions due to its flammability limit. The flammability range is defined as the concentration span expressed as percent fuel by volume of mixture or as a percentage of equivalence ratio. Above the upper flammable limit (UFL) the mixture is too fuel rich to burn, while below the (LFL) the mixture lacks fuel and does not ignite as well.

The flammability span for methane is way more restricted than one for hydrogen, as shown in Table 2.4.

	LFL	UFL
	Φ_{min}	Φ_{max}
CH ₄	0.46	1.64
H ₂	0.14	2.54

Table 2.4: Flammability limits for air-fuel mixture at atmospheric pressure.

Even when ignition has been achieved, the flame can be detached. Hence when operating with oxygen and methane combination, despite LOX high density, too high shear forces can lead to flame anchoring problems.

2.8 Flame instability

At least two types of combustion instability are recognized, in both of which the combustion reactions deliver the energy necessary to sustain the combustion: low-frequency and high-frequency instabilities.

Low-frequency instability, also know as *chugging* resulting from interactions of propellant-feed system oscillations and combustion-chamber gas vibrations: the variations in combustion chamber pressure appear to be a forced vibration driven by the pulsations of the propellant flow. Because of the inertia of the mass of liquid propellant participating in the vibrations, the frequency of the pressure oscillations is relatively low, here 10-400 Hz. It may originate from pump cavitation, fluctuations in tank pressurization or by the coupling of structural and feed system frequencies.

High-frequency combustion oscillations, from 4 to 20 kHz also called *screaming*, are confined to the gases in the combustion chamber, whose inertia is small compared to that of the liquid propellant in the feed lines. It is accompanied by a significant increase in the amount of heat transferred from the combustion gases to the walls of the chamber and to the injector face. According to Rayleigh's theory, vibrations in a confined mass of gas may be sustained by a periodic release of heat in the gas, if the oscillating component of heat release is in phase with the oscillating component of pressure (positive feed feedback). On the other hand, the gas vibrations will be impeded if the fluctuations in heat release and pressure are out of phase (negative feedback). Screaming is driven by variation in droplet vaporization or acoustic changes in combustion rates.

The instability phenomenon results in pressure waves coupled with heat peaks, oscillating depending of the vibrational modes.

The flame instability is detectable by a severe decrease of the boundary layer, a compression in the oxygen jet and a rise in the in the heat flux. The increase of the heat flux and the temperature field can lead to a structural damage of the nozzle.

Flame instability occurs easily in large-sized engine due to a minor natural frequency: the *Rocketdyne F-1* first stage of Saturn V failures are related to combustion instability. A solution adopted in Soyuz rocket for RD-107 engine is to split the single combustion chambers in four unities.

²Oxygen critical pressure: 50.5 bar.
Methane critical pressure: 46.1 bar. [15]

There are two critical flow conditions related to flame stability: liftoff and blowout. Liftoff should be avoided so that the flame is close to the burner and its position is independent of the flowrate. This allows positive ignition by a spark and assures that the flame condition is controlled. In some applications a certain amount of liftoff may be desirable to prevent overheating of injectors.

2.9 Combustion process

Combustion processes for liquid propellants combustion are typically non-steady, with local fluctuations in pressure, temperature, mixture ratio and radiant emissions. It is helpful to divide the thrust chamber into a series of discrete zone, that are: injection/atomization zone, rapid combustion zone, streamtube combustion zone, transonic-flow zone and supersonic expansion zone.

In the first zone, injected liquid oxygen atomizes, yielding large numbers of small droplets. Heat is transferred to these droplets by radiation from the very hot rapid-combustion zone. As the droplets evaporate, they create local region rich in either fuel and oxidizer vapor. This zone is highly heterogeneous, containing liquid and vaporized propellant, inducing large gradients in all direction with respect to propellants mass fluxes. The heat generation is relatively low because cold temperatures and fuel-rich or fuel-lean zones which do not burn. The gaseous methane contains no droplets and enters at higher injection velocity. The shear forces created on liquid jets produce rapid droplet formation and gasification.

In the rapid combustion zone, intense and rapid chemical reaction occur at increasingly temperatures. Here the remaining liquid droplets are vaporized by convective mechanism and mixing process is achieved by three-dimensional turbulent diffusion. The rapidly expanded heated gases create local transverse gas flow and even temporary back flows.

In the streamtube combustion zone, oxidation continue at a lower rate while some additional heat is release. Chemical reaction continue and streamlines form, characterized by high axial velocities.

Chapter 3

Experimental Setup

3.1 Previous experimental campaigns

The aim of the research is to simulate the combustion in a liquid rocket engine, operating in a low pressure range, i.e 10-20 bar. For the present pressure values, small satellite in 1-2 kN thrust range are taken into account as possible applications.

Due to the complexity linked to cryogenic propellants the problem has been initially simplified by injecting into the combustion chamber gaseous oxygen and gaseous methane. Among the complex flow phenomena one may list the phase change, hence the variation of flow properties and steep temperature gradients, the atomization process itself as well as two-phase flow coexistence and condensation shock waves. Among handling difficulties, tank pressurization, storage, feeding line design and liquefaction must be taken into account [16].

Hence, the research started with a simplified configuration: gas-gas propellants in a single element square combustion chamber. In this phase, different mixture ratios are evaluated as well as the cooling mass flow percentage and the recess length. The square section allows an optical access for OH* emissions evaluation method. The injector performance are evaluated and the proper design geometry is selected. CFD models and heat conduction methods are implemented and validated.

Afterwards, a multi injectors configuration is implemented to investigate the injector-injector interactions in a rectangular combustion chamber. A comparison with the single element combustion chamber has been carried out. A round section combustion chamber is tested and compared with the square one. The round chamber provides a models for a real combustion chamber even though an optical access is not possible due to curvature distortion.

The subsequent step is the liquid oxygen introduction.

The aim of implementing liquid oxygen is to analyze the combustion process and obtain the performance for a more realistic subscaled models. Despite a lower characteristic velocity is attended, as presented in Table 3.1, liquid oxygen implementation is pivotal to simulate a real propulsive system which gains overall performance from the higher density of the cryogenic oxidizer when compared to the gaseous one.

Oxidizer	Fuel	c^* [m/s]
Liquid Oxygen	Gaseous Methane	1869.2
Gaseous Oxygen	Gaseous Methane	1890.7

Table 3.1: Performance values for LOX/GCH4 and GOX/GCH4 propellants combinations calculated with CEA at $p_c = 20$ bar, OF=2.6, $\epsilon_c = 2.5$.

The higher performance of gaseous oxygen are explicable by the fact that the mixing process is better and faster accomplished for a gas-gas interaction. Furthermore, the flame temperature is higher for gaseous oxygen. Finally the injector element has been designed for gaseous oxygen, hence a further optimization would be necessary for LOX usage.

3.1.1 Comparison methodology

Geometric scaling aims to capture the full-scale geometrical features within the subscaled model [17]. Geometrically subscale models are based on a linear reduction of a full-scale length scales, that are chamber length and diameters, injector face plate diameters and nozzle dimensions. A non-length parameter is for example the number of injection elements. To scale between a full-size and a smaller-size combustor a practical approach considers identical injector elements, so that injector parameter and Mach number will match.

Since the possibility to scale chamber is a powerful tool for developing new combustion devices, some non-dimensional parameters listed in Section 2.2.2 are taken into account: Reynolds and Prandtl number, Schmidt number, Mach number, first and third Damköhler group.

To perform a comparison between several subscale hardware, combustion parameter in terms of pressure and mixture ratio have to be kept equal.

3.1.2 Single element GOX/GCH4 square combustion chamber

The square setup allowed to perform an optical diagnostic, that is an high speed camera used to detect the flame anchoring near the oxygen injection region. Furthermore, OH* spontaneous emissions have been investigated to analyze the flame front and the combustion process for different OF ratios. Moreover, a characterization of the injector design and validation of the simulation tool THERMTEST over a range of pressure and mixture ratio was carried out, having shown good agreement with experimental data. Thanks to this campaign, detailed temperatures measurements have been carried out and specific methods have been elaborated due to the transient nature and geometry of the hardware to derive heat flux data sets. The design of the multi element hardware will be based on final single-injector results.

Combustion chamber height	h_c	[mm]	12
Combustion chamber width	w_c	[mm]	12
Contraction ratio	ϵ_c	[-]	2.5
Combustion chamber length	L	[mm]	290
Combustion chamber wall thickness	w	[mm]	36.5

Table 3.2: Single element GOX/GCH4 square combustion chamber geometry.

3.1.3 Single element GOX/GCH4 round combustion chamber

The present combustion chamber was operated to investigate the effect of the oxidizer recess length in a shear coaxial injector. With a total length of 305 mm and an inner diameter of 12 mm, the chamber was been designed for a maximum pressure of 20 bar and a 4 s running time. The conical nozzle had a contraction ratio of 2.5. Post recess length was varied from 0 mm to 12 mm, having kept constant and equal to 0° the taper angle. It has been proved that GOX post recess enhances the mixing of propellants. The longer the recess length, the higher is the effect on the injector pressure drop and on the heat loads to the wall in the near injection region [18].

Combustion chamber inner diameter	d_c	[mm]	12
Contraction ratio	ϵ_c	[-]	2.5
Combustion chamber length	L	[mm]	305
Combustion chamber wall thickness	w	[mm]	19

Table 3.3: Single element GOX/GCH4 round combustion chamber geometry.

3.1.4 Comparison of a square and round single element GOX/GCH4 combustion chamber

To allow good comparison between the two chambers, the same geometry was kept constant in terms of inner dimension and total length, as well as the contraction ratio, equal to 2.5. Same Schmidt and Prandtl number have been ensured, having used the same propellant. The injected mass flow is scaled to ensure the same pressure level, according to Eq. (2.5).

In both chamber configurations the igniter is located in the middle of the combustion chamber and the instrumentation set up is composed by pressure transducers and thermocouples of type K and T. It has been observed that increasing the recess, i.e the distance between the end of the oxygen injector duct and the end of the methane coaxial injector, led to a decrease in the mass flow rate and to an increase in the mean combustion pressure. In particular, for the square chamber higher values in the mass flow rate are registered, such as in the pressure values.

The square chamber presented:

- Higher temperature and heat flux profile along axial length due to a better mixing process.
- Higher pressure drop because of minor area occupied by the flame resulting in higher velocity.
- Among the disadvantages, an higher pressure fluttering, due to cylindrical flame adapting to the square duct.

The chamber temperature is higher in the square chamber because the presence of the corners allows a better mixing in the recirculation zone. The pressure and the mass flow rate both are higher in the square chamber, but their ratio has to be lower to ensure the same characteristic velocity, since the rectangular cross section is larger.

$$c^* = \underbrace{A_{th,square}}_{\uparrow} \left(\frac{p_{th,tot}}{\dot{m}_{th}} \right)_{\downarrow square}$$

However, the following common features have been observed:

- The temperatures rise along the axial position, while the flow accelerates along the duct and the pressure decreases up to the 6%.
- The combustion process is achieved before the nozzle section.
- The stagnation point, that is the peak in the pressure when the flame impacts the wall, occurs for the same axial position.
- The heat flux has a steady rise along the duct and reaches a constant value before the nozzle section.
- Increasing OF leads to an higher heat flux values and higher temperatures.
- Increasing the recess length increases heat flux values and the combustion efficiency.
- Fluttering in heat flux, temperature and pressure distribution occurs when the combustion process is ended.

3.1.5 Multi-injector GOX/GCH4 rectangular combustion chamber

An Inverse Heat Transfer Method was developed and applied for the calculation of the heat flux and temperature field in a five elements rectangular combustion chamber, operated with GOX-GCH4 at a pressure of 20 bar in a range of mixture ratios from 2.6 to 3.4. The goal was to determine the combustion properties and injector/injector interactions, by means of the IHCM which used the thermocouple measurements to deduce the heat flux. The resulting temperature profile demonstrate a good agreement with the measurements as well as transient effect during start up are successfully captured. The transient profiles of pressure signal and heat release showed a similar trends. The temperature measurements and the resulting heat flux showed a reduced stratification among the five injectors with increasing distance from faceplate.

Combustion chamber height	h_c	[mm]	12
Combustion chamber width	w_c	[mm]	48
Contraction ratio	ϵ_c	[-]	2.5
Combustion chamber length	L	[mm]	277
Combustion chamber wall thickness	w	[mm]	36.5
Number of injector elements		[-]	5

Table 3.4: Multi-injector GOX/GCH4 rectangular combustion chamber geometry.

3.1.6 Comparison of a single and multi-injector GOX-GCH4 rectangular combustion chamber

The two combustors kept the same injector element as well as the contraction ratio, hence the same Mach number, and since identical propellant was used, Prandtl number was kept identical. The campaign tested the two combustors at the same OF and at equal nominal pressure of 20 bar, thus, since the contraction ratio is the same, the mass flow had to be scaled proportionally to the difference in cross sectional nozzle area, as follows:

$$P_c = \left(\frac{\dot{m}_c^*}{A_t} \right)^2 \quad (3.1)$$

In conclusion, a shorter flame length and a faster combustion process have been observed for the multi-element chamber. The interaction between the injectors and the merging of the flame enhanced the mixing process leading to higher temperature zones and a consequently major acceleration of hot gases. Moreover, the lower mass flow rate injected, according to Eq. (3.1), hence the lower velocity at the injection, produced a faster acceleration of the flow [19]. Due to the different acceleration, it resulted in a difference in flame turbulence which contributed to local mixing of the species and completeness of the reaction.

3.1.7 Multi-injector GOX/GCH4 round combustion chamber

The hardware had an inner diameter of 30 mm, a contraction ratio of 2.5 and an ignition system of 7 elements, being designed up to a chamber pressure of 100 bar and maximum temperature of 3600 K. The main goal of this investigation was to determine the thermal loads and the pressure distribution along the combustion chamber axial direction and azimuthal direction.

The experiment led also to a flame instability study, characterized by fluctuation in the dynamic pressure along time. When the combustion instability took place, the static pressure instantly dropped and the temperature profile in azimuthal direction increased in case of anchored flame or decreased in case of lifted flame [20].

Therefore, due to the low ignition limits of methane/oxygen propellant combination, it has been found that not all the seven injectors ignite simultaneously. In case of not successful flame anchoring, the flame could have reattached or brought to combustion instabilities.

Two regime of heat release have been distinguished. A near injectors zone where the mixing had a dominating effect and a downstream zone where heat release was dominated by combustion itself.

Combustion chamber inner diameter	d_c	[<i>mm</i>]	30
Contraction ratio	ϵ_c	[–]	2.5
Combustion chamber length	L	[<i>mm</i>]	345
Combustion chamber wall thickness	w	[<i>mm</i>]	80
Number of injector elements		[–]	7

Table 3.5: Multi-injector GOX/GCH4 round combustion chamber geometry.

3.2 MoRaP

The MoRaP (Mobiler Raketen-Prüfstand) is a mobile, easy handling test bench used for short test operations and equipped with a control and data acquisition systems. It allows the installation of a combustion chamber, a feeding system, an ignition system and a purge system.

The test bench experiments with a capacitive thrust chambers at low thrust levels ($\approx 500N$).

The MoRaP can operate with gaseous oxygen and gaseous methane, as well as hydrogen and oxygen propellants combination.



(a) Left view: fuel supply line.

(b) Front view: AO and Do ports.

Figure 3.1: MoRaP facility assembly with rectangular thrust chamber.

3.2.1 MoRaP: GOX supply line

The fluid plan for the GOX and methane supply line is depicted in Figure 3.2.

The yellow branch refers to gaseous methane, supplying the combustion chamber within fuel, as well as the grey line refers to gaseous oxygen, supplying within oxidizer. Green line represents gaseous nitrogen supply line composed by four branches: two aimed to purge both fuel and oxidizer branches, one to provide film cooling to the glass window and to feed the igniter.

Fuel flows from the methane tank through a filter and then is split into two branches: one for the main line feeding the fuel injector and one feeding the igniter. The main line is composed by a pressure regulator, followed by a main valve, pressure and temperature sensors and a sonic orifice right before the combustion chamber propellant manifolds.

The igniter branch line consists of a pressure regulator and a main valve as well, followed by a check valve, a pressure sensor and a sonic orifice. A branch line for discharging the propellant is ensured by a bypass valve.

The same scheme concept is implemented for oxidizer line.

The supply line is explained in detail in Figure A.1 and Figure A.2a.

In case of Hot Fire tests with hydrogen, the methane tank bottle is simply replaced with a hydrogen tank bottle.

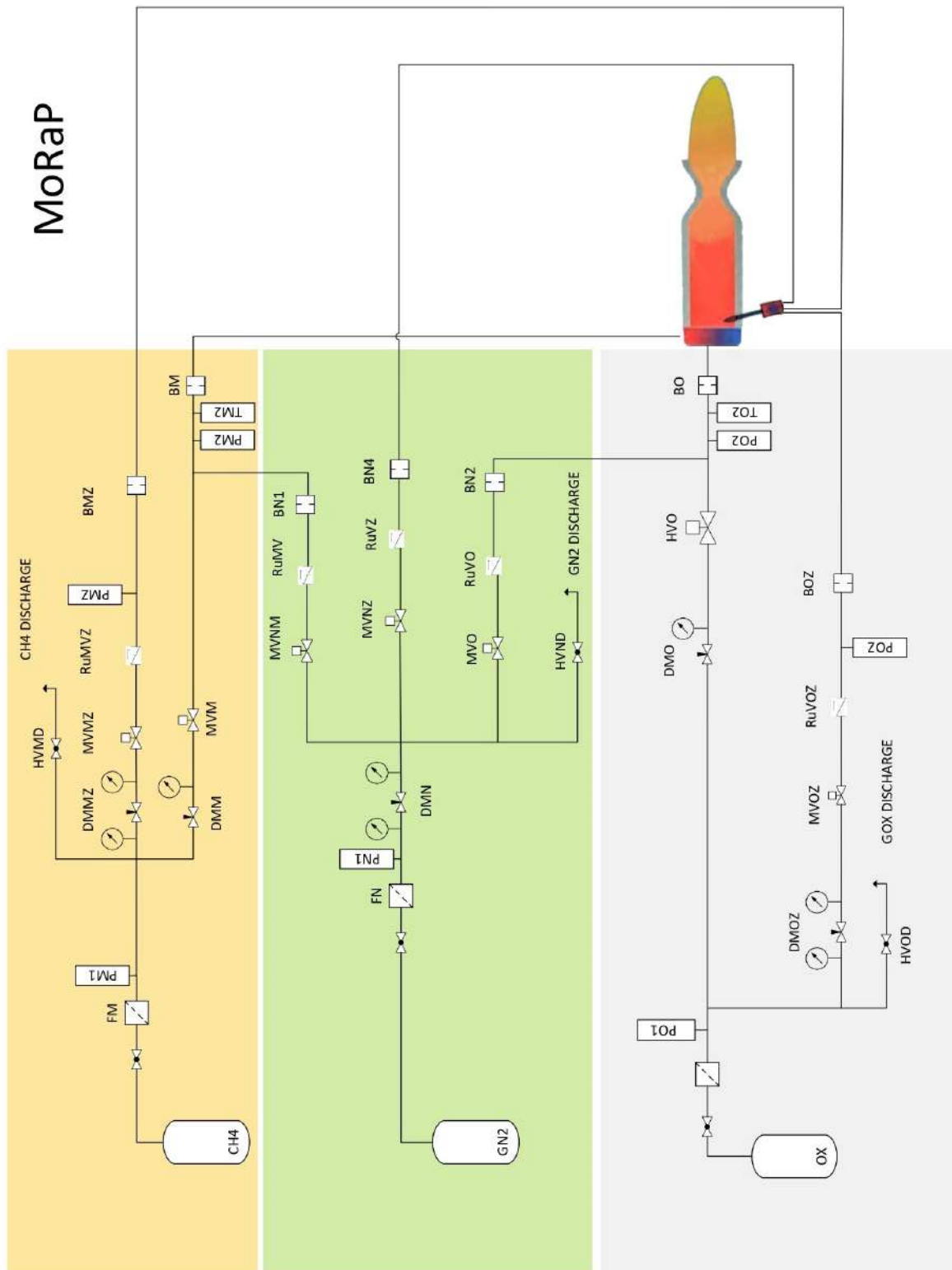


Figure 3.2: MoRaP Fluid Plan with gaseous methane and gaseous oxygen.

3.2.2 MoRaP: square combustion chamber

The current test campaign is performed with a modular square combustion chamber represented in Figure 3.7, made of oxygen-free copper Cu-HPC. Due to copper high thermal conductivity properties, the chamber cooling is achieved by a passive cooling technique, that is natural heat dissipation. Among the advantages one may list no power consumption, lighter weight and lower costs, despite the short time available for running the test. Thus the combustion chamber is designed for a testing time of up to 3 seconds at the maximum chamber pressure of 20 bar.

The combustion chamber geometry is presented in Table 3.6.

Length	Cross section area	Throat section area	Contraction ratio
[mm]	[mm ²]	[mm ²]	[-]
290	12x12	12x4.8	2.5

Table 3.6: Combustion chamber geometry.

The combustion chamber is mounted with an injector system composed by a single element shear coaxial injector presented in Figure 3.3 and operated with LOX/GCH4 or LOX/GH2 as propellants combination.

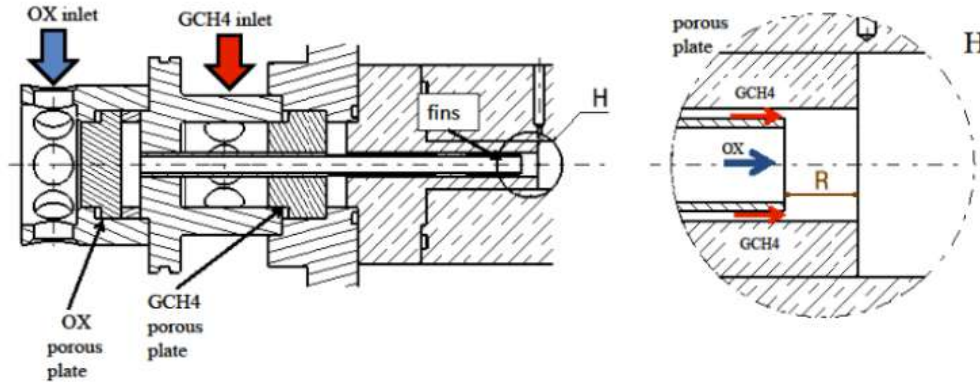


Figure 3.3: Single injector element configuration for LOX/GCH4 propellants combination.

Oxidizer injection outer diameter	D_O	[mm]	3
Oxidizer porous plate outer diameter	D_{pM}	[mm]	4.8
Fuel injection inner diameter	d_M	[mm]	5
Fuel injection outer diameter	D_M	[mm]	6
Fuel porous plate inner diameter	d_{pM}	[mm]	21.5
Fuel porous plate outer diameter	D_{pM}	[mm]	6
Number of fins at fuel injection area	n_{fM}	[-]	4

Table 3.7: Single injector element geometry.

The chamber is cooled by liquid nitrogen and a quartz-glass flat window allows an optical access to the flame in the near injector area. The test campaign is initially performed with a copper window and afterwards with a glass window mounted as shown in Figure 3.4. The glass window is mounted on the upper wall of the combustion chamber in order to perform an optical diagnostics of the flame in the near injector area via *Chemiluminescence Analysis*.

A film cooling system with gaseous nitrogen is provided to protect the quartz-glass window from the heat loads and graphite foils are placed to protect both glass and copper windows from high temperature loads. A purge system for both oxygen and methane is supplied by a gaseous nitrogen line.

The combustor has a square cross section of $12 \times 12 \text{ mm}^2$, two chamber segments with a total length of 290 mm and a contraction ratio of 2.5, providing an average Mach number equal to 0.24.

The nozzle is a truncated trapezoidal prism with a rectangular cross section of $4.8 \times 12 \text{ mm}^2$. Although the unusual cross section geometry used for the combustion chamber and the nozzle, a rectangular configuration allows a correct optical visualization. Indeed, a window mounted in a round combustion chamber would lead to optical distortion and aberrations.

A test sequence is programmed in LabView and divided into three main periods: start up and ignition, main combustion operation and shut down.

A spark torch igniter ignites the propellant mixture. A branch of oxygen and methane line converges as depicted in Figure 3.2 to the igniter where the two propellants are premixed, ignited and injected in the combustion chamber. Two possible positions are available for the igniter as depicted in Figure 3.5: at the injection section and at middle section of the combustion chamber. The combustion chamber is provided with pressure sensors and with type T and K thermocouples.

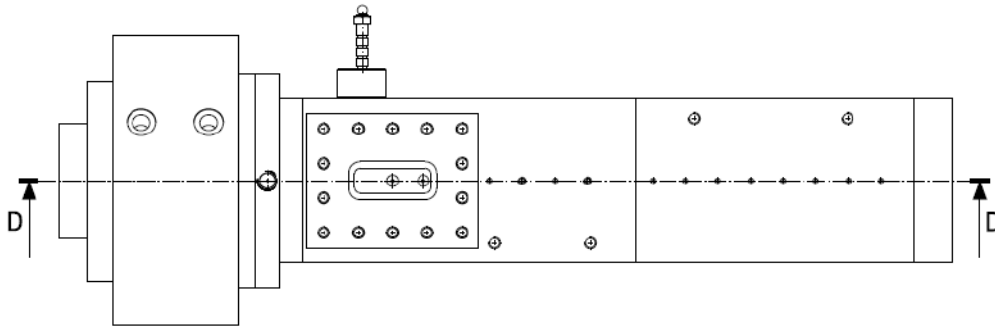


Figure 3.4: Top view of single element square combustion chamber with mounted window and igniter. Christoph von Sethe's Semester thesis (2016).

3.3 Measurement set up

3.3.1 Pressure Transducers

WIKA A10 pressure sensors are placed in the chamber manifolds prior two porous plates, one for oxidizer and one for fuel, which allow homogeneous injection conditions.

The combustion conditions are evaluated by 9 pressure transducers (PC0, PC1, PC2, PC3, PC4, PC5, PC6, PC7, PC8) sat on the side wall and spaced every 34 mm as depicted in Figure 3.5.

3.3.2 Thermocouples

The combustion conditions are evaluated through type T thermocouples with 0.5 mm inner diameter positioned at 1 mm , 2 mm and 3 mm from the hot wall. The distance from hot gas side and the axial positions are shown in Figure 3.6. The thermocouples are placed on the bottom wall. Each thermocouple is kept in position by a spring and each thermocouple end is connected to the cart as shown in Figure A.5a.

Thermocouples type T are place within the LOX supply line as described is Scheme 3.9 and one thermocouple type K with 1 mm inner diameter is placed inside the liquid nitrogen bath.

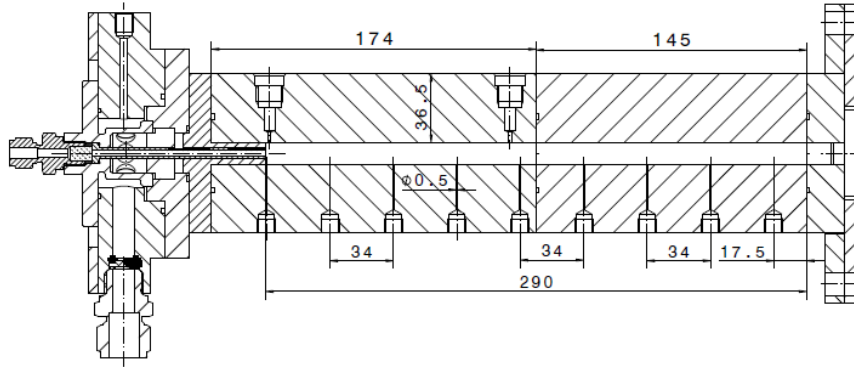


Figure 3.5: Top view of pressure sensors set up. Christoph von Sethe (2019).

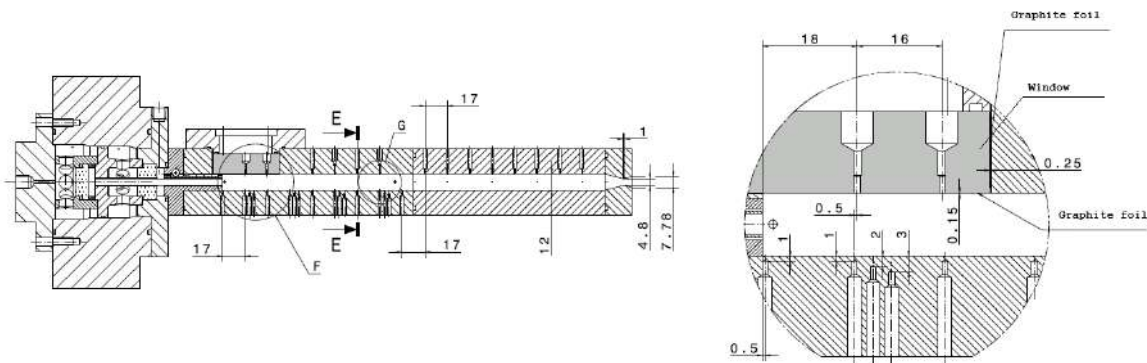


Figure 3.6: Side view of thermocouples set up - Detail 2:1 scale of thermocouples at injection section. Christoph von Sethe's Semester thesis (2016)

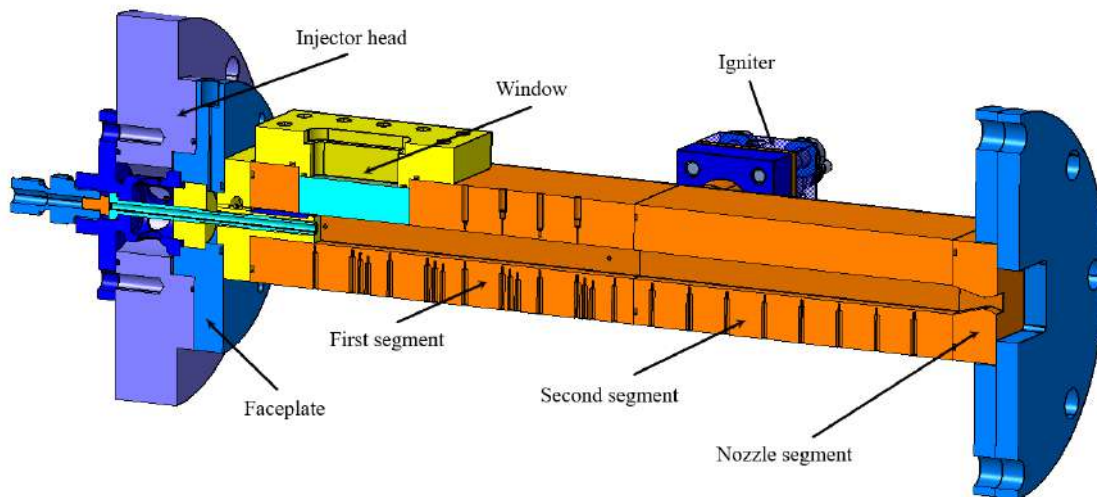


Figure 3.7: Side view of the single element square combustion chamber complete assembly with window and igniter positioned at middle section. Christoph von Sethe's Semester thesis (2016).

3.4 Optical set up

The ICCD camera (*Intensified Charge Coupled Device*) is mounted above the test bench, aiming to record the OH* emission which leaves the top wall window of the combustion chamber. The image of the flame within the combustion chamber is reflected by a planar mirror positioned at 45° above the the window as schematized in Figure 3.8 and shown in Figure A.20d.

3.4.1 ICCD Camera

The ICCD FlameStar2 camera is design to detect weak light emission phenomena with high accuracy and resolution. It covers the wavelength range from 190-800 nm. An intensified CCD camera when compare to a simple CCD, allows to:

- Measure single photons.
- Extend the spectral sensitivity down to 180 nm.
- Operate with an extremely short shutter of several ns.

The intensifier is fiber optically coupled to the CCD sensor. The image intensifier is a vacuum tube containing three elements. A photo cathode transmits light over the range near UV visible and near IR, a micro channel plate (MCP) provides electron gain and a phosphor element.

The image is focused onto the photo cathode plane: the impinging photons generate electrons which in turns are accelerated by applying an electric potential difference to the photo cathode. The electrons hitting the MPC walls generate secondary electrons thanks to the applied high voltage and are accelerate onto the phosphor plate generating photons. The emitted light is hence collected by the CCD and converted in a electronic output. The analogue signal is digitized by A/D converter, integrated in pixels and transferred to the computer memory.

To detect the spontaneous OH* emission a narrow band-pass filter is placed in front of the sensor of the ICCD camera, which captures the light emitted by excited by hydroxyl radicals. From the front panel of the Image Intensifier Control Unit the time delay Δd and the gate width δt are manually adjustable with a knurl switch. The delay with the respect of the input pulse is set at 500 μs , while the gate time, during which the light enters the camera, is selected at 300 μs .

The camera set up, i.e. the FlameStar2 camera, the spectral filter and the planar mirror have been protected with an absorptive black sheet.

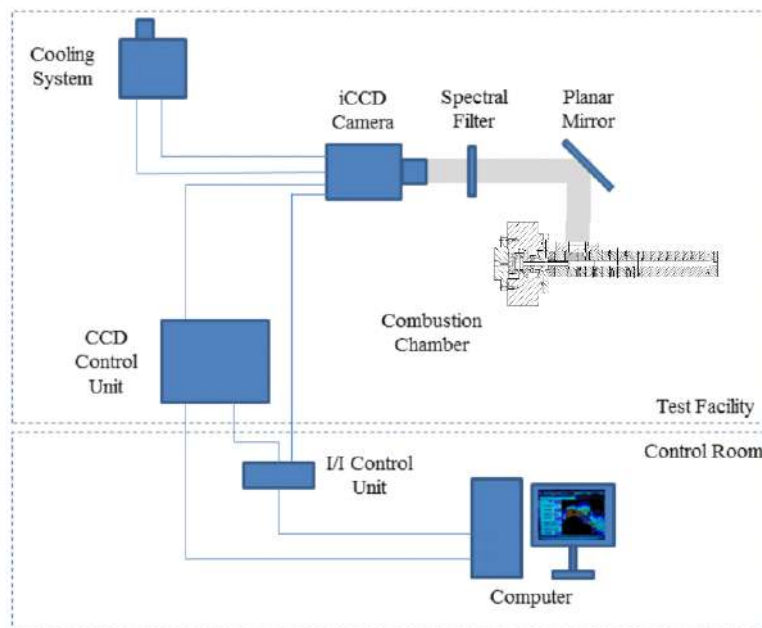


Figure 3.8: Optical setup schematics for OH* emission imaging.

3.5 Cold Flow Test Campaign Preparing

Before carrying out Cold Flow test several consecutive activities have to be performed.

3.5.1 LOX supply line assembly

The previous GOX/GCH₄ feeding system has been modified with a LOX supply line which was built from the beginning for this thesis purpose.

A feeding supply line for liquid oxygen is first designed as showed in Figure 3.9, by referencing previous works at LTF [21]. Each component is selected according to pressure, temperature, mass flow and voltage constrains. Before assembling the line, all components which would deal with liquid oxygen, hence valves, pipes, bolts or t-parts, are cleaned with acetone to avoid oxygen reactivity with any organic residues.

3.5.2 Pressure sensors calibration

Pressure sensors are calibrated so that a 3-grade polynomial converts the output electrical signal showed by LabView in voltage or current units in equivalent pressure values in bar units.

A pressure supply is needed, provided by a portable pneumatic pressure system shown in Figure A.6. It is composed by a nitrogen bottle, a pressure regulator with two pressure gauges for upstream and downstream conditions monitoring and a PC6 pressure calibrator. The pressure transducer to be calibrated is connected to exit on the left and plugged into MoRaP.

The signal in mA or V corresponding to 0 bar is recorded. The nominal value is equal to 0.004 mA and to 0.03 V , however the real value is recorded and set as zero.

Therefore other pressure values are read from the PC6 screen placed in a nitrogen pressurized line, while the corresponding electrical values are registered via LabView. After a sample of 8 measurements from 0 to 30 bar, the polynomial coefficients are computed and saved in *Calibration.txt* file.

3.5.3 Leakage Test before Cold Flow Test

The leakage test is performed by injecting gaseous nitrogen through the new-built line for liquid oxygen, up until the MVLOX. The pressure values are read from LabView: when no drop in pressure is registered the tightness is ensured.

A further leakage check is carried out by distributing soap water whereas junctions are present: when no bubbling is detected the tightness is ensured.

To ensure the pressurization, the discharge line on top of liquifier inner tank is closed and the main oxygen valve is kept closed.

3.5.4 Insulation for Cryogenic line

Only after having ensured no line leakage, the liquid oxygen branch of the supply line is insulating with cryogenic insulation. From Figure A.14c one may see that the LOX line is completely insulated, from the liquifier external tank up to faceplate of the combustion chamber. Liquid nitrogen branch line is insulated as well.

3.6 LOX supply line

Liquid oxygen is produced by gaseous oxygen, provided by MoRaP's gaseous oxygen tank, by means of a liquefier: the gaseous oxygen enters from the top of an inner tank immersed in a liquid nitrogen bath placed into an outer one. At ambient pressure, liquid nitrogen has its boiling point at 77 K, lower than oxygen's 90 K. Hence the liquefied oxygen is produced and is flowed down to the main line. Liquification process is explained in detail in section 5.1.2.

An over pressure valve is placed on top to protect oxygen tank from exceeding pressure values, preceded by a pressure sensor. A check valve and a relief valve are placed to avoid suction by exit valve opening. Liquid oxygen flows from the bottom of the inner tank, screwed to the outer, where a temperature sensor is placed. A Venturi meter allows the mass flow computation. After having run into high

Branch line	Name	Component	Comment	Symbol
GOX Igniter	DMOZ	Pressure regulator		
	MVOZ	Main valve		
	RuVOZ	Check valve		
	POZ	Pressure sensor		
	BOZ	Orifice		
GOX	PO1	Pressure sensor		
	HVOD	Exit valve		
	DMO	Pressure regulator		
		Relief valve		
		Check valve		
FO	Filter			
LOX		Overpressure valve		
	PTANK	Pressure sensor		
	TLOXVEN1	Thermocouple	Type T	
		Exit valve	NO Manual	
	PLOXVEN1	Pressure sensor		
	PLOXVENT	Pressure sensor		
	PLOXVEN2	Pressure sensor		
		Venturi meter		
		Turbine		
	TLOXVEN2	Thermocouple	Type T	
		Supply valve	NC Manual	
	TO2	Thermocouple	Type T	
	PO2	Pressure sensor		
	MVLOX	Main valve	NC Pneumatic	
		Bypass valve	NO Manual	
TO3	Thermocouple	Type T		
PO3	Pressure sensor			
LN2		Check valve		
	TLN2	Thermocouple	Type K	

Table 3.8: Oxygen line components.

3.6.1 Venturi meter

The Venturi meter is equipped with three pressure sensors, placed upstream, downstream and at the throat section, together with upstream and downstream temperature sensors.

Using continuity equation and energy conservation for upstream and throat section locations, mass flow calculation is obtained in Eq. (3.6):

$$\begin{aligned} \dot{m}_{line} &= \dot{m}_{th} \\ \rho_{line} V_{line} A_{line} &= \rho_{th} V_{th} A_{th} \end{aligned} \quad (3.2)$$

$$h_{line} + \frac{1}{2} V_{line}^2 = h_{th} + \frac{1}{2} V_{th}^2 \quad (3.3)$$

Assuming the geometry presented in Table 3.9, the flow velocity at the Venturi throat is hence computed as:

$$V_{th} = \sqrt{\frac{2 \cdot (h_{line} - h_{th})}{[1 - (\frac{\rho_{th}}{\rho_{line}})^2 \beta^4]}} \quad (3.4)$$

where the density ratio and the enthalpy difference are computed by means of REFPROP2D function in MATLAB[®] using NIST REFPROP database. Inputting pressure and temperature values read from measurements for both upstream and throat conditions, corresponding density and enthalpy values are computed. The parameter β is the contraction ratio, namely:

$$\beta = \frac{d_{th}}{d_{line}} \quad (3.5)$$

where d_{line} and d_{th} are the line and Venturi's throat diameters, respectively. Hence the LOX mass flow rate across Venturi meter is obtained as follows:

$$\dot{m} = C_d A_{th} \rho_{th} V_{th} \quad (3.6)$$

where C_d is Venturi discharge coefficient obtained from a cold-flow water calibration.

Line diameter	Throat diameter	Discharge coefficient
[mm]	[mm]	[-]
6	2.5	0.988

Table 3.9: Venturi meter geometry.

3.6.2 Venturi geometry optimization

Venturi meter geometry has been initially assumed from [21] as in Table 3.9. After observing high noise level, as detectable in Figure 6.3 and significant uncertainties in mass flow calculation, a volumetric turbine was placed after Venturi meter to ensure the reliability of calculations.

Hence Cold Flow test evaluation is carried out both with turbine measurements and with Venturi calculation for LOX mass flow rate and results are compared in Figure 3.10.

Therefore an optimization of Venturi geometry is carried out in order match turbine measurements. The turbine provides volumetric flow measurements which are multiplied for LOX density to obtain mass flow rate values. Density is in turns calculated via REFPROP2D function. Hence when comparing Venturi and turbine mass flow rates, they both are affected by errors and uncertainties.

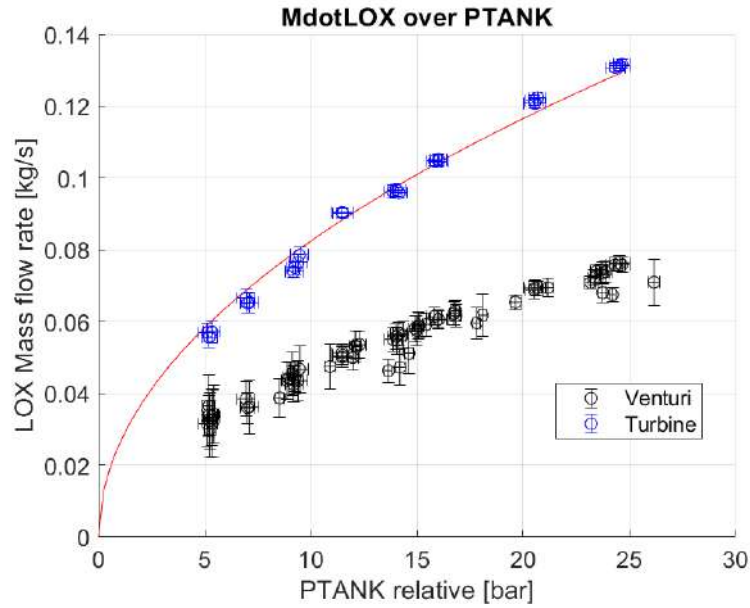


Figure 3.10: Cold Flow evaluation for Venturi and turbine mass flow rate versus tank pressure relative to ambient pressure plotted with uncertainties

A parametric analysis is carried out varying both line diameter d_{line} and throat diameter d_{th} . Results show a no significant dependence of mass flow rate on line diameter. Figure 3.11 shows the best throat diameter that match turbine and Venturi mass flow rate.

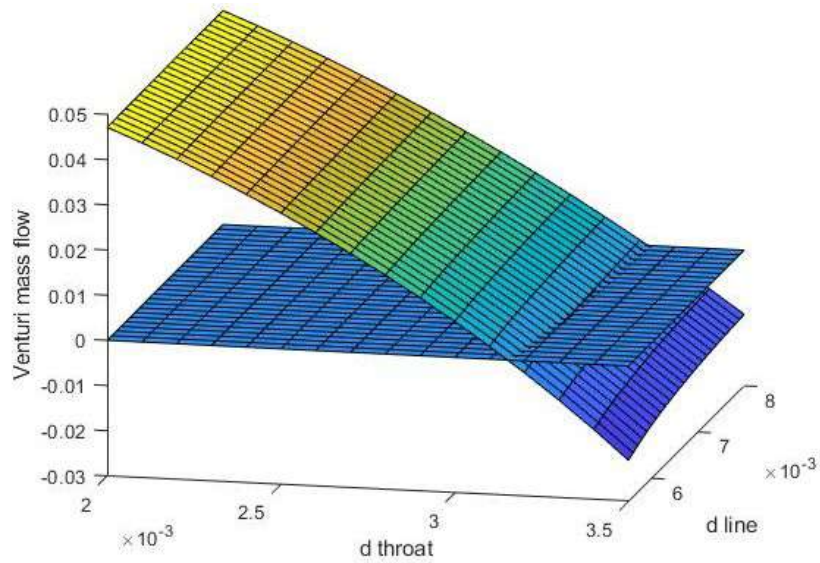


Figure 3.11: Parametric study for optimization of Venturi geometry

After that the optimization has been carried out for all Cold Flow tests performed with both turbine and Venturi meter, a new geometry is chosen and presented in Table 3.10.

Line diameter	Throat diameter	Discharge coefficient
[mm]	[mm]	[-]
6	3.25	0.95

Table 3.10: Venturi meter geometry after optimization.

3.7 Hot Flow Test Campaign Preparing

After having performed the Cold Flow campaign, the Hot Flow test campaign needs to be prepared. In this phase, the combustion chamber is mounted onto MoRaP facility. Temperature and pressure sensors are added and mounted within the chamber and connected to MoRaP's module and analog cart.

3.7.1 Combustion Chamber mounting

The thrust chamber consists of two segments of the combustion chamber and of the nozzle segment. The three components are initially aligned and coupled, hence are held together by four rods equipped with a spring each. Each spring positioned at one end of the road is loaded by screwing a bolt at the other end in contact with the nozzle plate. Each spring is loaded for the same axial distance, known from previous work to be equal to 28 mm from injector head to the spring. In Figure A.4b springs and roads are visible.

Between the nozzle segment and the nozzle plate, a graphite foil of thickness 0.26 mm is positioned.

3.7.2 Thermocouples mounting

The combustion chamber thermocouples are inserted into the holding plate by inserting each spring positioned at one end. Hence the holding plate is positioned at the bottom wall of the combustion chamber. The other end of each thermocouple is inserted into the cart module. White cable end corresponds to '-', while brown or green cable end corresponds to '+'. The thermocouples plugging into cart is shown in Figure A.5a and the cart is inserted into MoRaP as in Figure A.5b.

The final configuration of the thermocouples positioning is explained in Section 3.3.

Each thermocouple is labeled at both ends.

3.7.3 Pressure sensors mounting

Nine pressure are placed on one side wall of the combustion chamber, as described in Section 3.3. Each pressure sensors is attached to MoRaP as in Figure A.3a and connected to the chamber by means of a pipe. Before the connection, each pipe is cleaned with acetone and pressurized air and each pressure sensor entrance is filled up with anti-frost fluid.

3.7.4 Copper window positioning

The copper (Cu-HCP) window is 49.5 mm long, 32.5 mm wide and 14.8 mm high. It is positioned into an appropriate slot onto the top wall of the first segment of the combustion chamber. Graphite foil are positioned afterwards to avoid the displacement of the window and to protect the window itself from high temperature loads. Graphite foils instructions are specified in B.6. On top of the window, a window holder provided with 14 screws as in Figure A.8b.

3.7.5 Glass window positioning

Before the Hot Test campaign with glass window, the copper window is removed and replaced with quartz glass window. Graphite foils instructions are specified in B.7.

While mounting the plate holding on top of the glass window, special care should be taken to avoid the glass-typical fragile breaking. Hence the screws placed at the corner are not completely tight, despite a small amount of leaking would occur. From Figure A.8 the film applicator is visible before having placed the window.

3.7.6 Leakage Test before Hot Flow Test

The leakage test is performed once again the combustion chamber and the copper or the glass window have been mounted. The thrust chamber is closed by means of a plug, hence the line is pressurized at 20 bar. Cross-checks with pressure values and soap water are carried out as previously described in section 3.5.3. An example of leakage is shown in Figure A.9.

Chapter 4

Methods of Evaluation

Pressure and temperature sensors are installed along the propellants supply line and within the combustion chamber walls, providing inputs to calculate combustion performance via the AUSWERTUNG MATLAB routine explained in Section 4.2. Moreover combustion chamber pressure distribution and propellants injection pressures are plotted versus time and chamber axial length. Thanks to pressure and temperature sensors placed at fuel orifice and Venturi inlet and throat, mass flow rate calculations are carried out. LOX mass flow rate is computed as described in Section 3.6.1. Fuel mass flow rate and nitrogen film cooling mass flow rate as described in 4.2.1.

Wall temperature measurements are plotted versus time and chamber length, hence together with pressure values, enthalpies are calculated.

Corrected enthalpies are calculated with Eq. (4.6), knowing the heat release from INVERSE METHOD described in Section 4.3.

Finally theoretical and evaluated combustion efficiency c^* values are determined, resulting in combustion efficiency η_{c^*} , according to Eq. (2.9).

Since the flat window allows an optical diagnostics, here Chemiluminescence Imaging, the images taken by the ICCD camera are processed through AVERAGED IMAGES MATLAB routine reported in Section 4.4.3.

The averaged OH* emission is analyzed in the near injection area by ABEL MATLAB routine described in Section 4.4.5.

4.1 Reference system

For this present aim, z axis is referred to chamber axial length, while x and y axes define the cross sectional plane as in Figure 4.1.

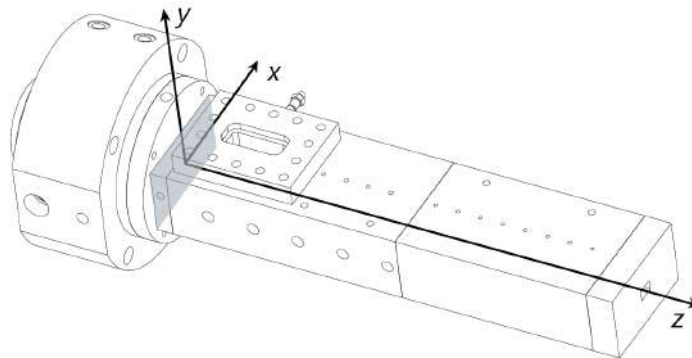


Figure 4.1: Reference system of the combustion chamber.

4.2 Auswertung routine

AUSWERTUNG MATLAB routine has been previously implemented to handle the raw data provided by pressure and temperature sensors and to create plots both over running time and chamber length. Moreover the measured parameters are given as input for mass flow rates, enthalpies, heat flux and performance calculations.

The previous code version is modified for this thesis purpose in order to implement a version suitable for liquid oxygen for both Cold Flow and Hot Fire test cases.

LOAD THE GEOMETRY. Combustion chamber geometry, Venturi geometry, methane and nitrogen film orifices geometry are loaded. Discharge coefficients for Venturi and orifices are loaded and cross sectional areas are computed.

RAW DATA TO PHYSICAL VALUES. Raw data, both analog and digital output, are collected. Digital output correspond to valves opening/closing, while analogs show mA or V units for pressure sensors and K for temperature sensors. Analog data are read from *Sequenz.txt* file generated by LabView and saved in a matrix. From *Calibration.txt* file, polynomial coefficients for each sensor are read and saved in 'Multipliers' matrix. The two matrices are hence multiplied, having powered the coefficients from 3 to 0 grade. Note that for thermocouples measurements, all the coefficients are equal to 0 except the one powered to 1.

MASS FLOW CALCULATIONS. LOX volumetric flow rate is measured by the turbine and converted in mass flow rate using the density computed with REFPROP function. LOX mass flow rate is calculated with Venturi meter as explained in Section 3.6.1. Mass flow rates for methane and nitrogen film are computed as described in Section 4.2.1. For Cold Flow test case only LOX mass flow rate is computed.

EVALUATION TIME. For Cold Flow test case the evaluation time is chosen after having run once the code and having ensured the liquid phase of oxygen through the main valve. The evaluation window time, centered in the evaluation time, is chosen equal to 0.5 seconds for all tests. For Hot Fire test case the chamber start up time is found whereas the chamber pressure averaged for all the pressure sensors PC displays the highest values during time. Performing the average among all chamber pressure sensor avoids the overshoot of one sensor. The chamber shut down time is found whereas the first pressure sensor PC0 show a decay of more than 20%. The difference between start up and shut down time give the burning time window. The ignition is verified ensuring that both igniter pressure sensors POZ and PMZ are higher than 5.5 bar. Hence the evaluation time is calculated as follows:

$$t_{eval} = t_{start} + \frac{2}{3}\Delta t_{burning}$$

The evaluation window is chosen equal to 0.5 seconds for all tests. Hence for both Hot Fire and Cold Flow cases the mean values of all measured and calculated quantities are computed over the evaluation window. The uncertainties for the measured and calculated values are computed over the evaluation window as explained in Appendix A.

PLOTS GENERATION. Plots are generated for all calculated and measured value over time and chamber length. Uncertainty are added to plots relative to chamber length. In Hot Fire test case plots for digital signals are added.

ENTHALPIES COMPUTATION. Total LOX injection enthalpy is computed using REFPROP database: the reference enthalpy of oxygen at standard conditions is removed to match CEA value of liquid oxygen. Fuel total injection enthalpy is calculated via *GetPropG* function according to [1]p.19. Hence enthalpies are corrected as explain in Section 4.2.2 using the Inverse Method.

PERFORMANCE CALCULATION. Theoretical performance are calculated using *SimpleRocket1Fluid* function based on Gordon [1] inputting total enthalpies, OF ratio, chamber total pressure and geometry values. The calculated combustion efficiency c^* is computed by Eq. (2.5) inputting the value from the

experimental test. Therefore the combustion efficiency is obtained by Eq. (2.9) dividing the calculated c^* by the theoretical c_{th}^* .

4.2.1 Fuel and Film Mass flow rate calculations

Mass flow calculations for gaseous fuel and for film cooling are computed within AUSWERTUNG using an optimizing function. The initial mass flow rate is defined as:

$$\dot{m} = A \cdot \rho \cdot v \quad (4.1)$$

An initial try for the mass flow rate is given as input, hence the stream velocity v is computed, knowing the feedline area A upstream the orifice and having calculated density ρ with REFPROP function. Knowing the stream velocity v and the speed of sound a , the Mach number is derived and used to compute total temperature and total pressure:

$$\begin{aligned} T^* &= T \cdot \left(\frac{1 + \frac{k-1}{2} M^2}{1 + \frac{k-1}{2}} \right) \\ p^* &= p \cdot \left(\frac{T^*}{T} \right)^{\frac{k}{k-1}} \end{aligned} \quad (4.2)$$

Where T^* is the temperature at the throat of the orifice, whereas Mach number is equal to 1. Knowing pressure coefficient c_p , molar mass M and the gas constant R from REFPROP function, mass flow is given by:

$$\dot{m} = c_d \cdot A^* \cdot p^* \cdot \sqrt{\frac{k^*}{R \cdot T^*}} \quad (4.3)$$

where A^* is the orifice throat area. The specif heat ratio k^* is optimized as well, using the pressure coefficient c_p^* computed with REFPROP using an average value of temperatures and pressures:

$$k^* = \frac{c_p^*}{c_p^* - R} \quad (4.4)$$

4.2.2 c_{th}^* calculation via CEA

In this present aim the theoretical characteristic velocity c_{th}^* is calculated with CEA assuming a non-adiabatic process. Thanks to IHTM, the inlet temperatures T_{ox} and T_{fuel} are scaled according to the heat losses \dot{Q} , obtained from heat flux \dot{q} integration on chamber walls surface. Hence, the corrected heat flux is calculated separately for fuel and oxidizer as follows:

$$H_{o,corr} = H_o - \frac{\dot{Q}}{\dot{m}_{tot}} \quad (4.5)$$

$$H_{f,corr} = H_f - \frac{\dot{Q}}{\dot{m}_{tot}} \quad (4.6)$$

Thanks to the correction in Eq. (4.6), the heat losses are removed from the combustion efficiency. The resulting theoretical characteristic velocity is lower, leading to a higher combustion efficiency.

LOX enthalpy computation is first carried out by means of REFPROP function; hence the reference enthalpy at 300 K and 1 bar has been removed to match CEA values.

The CEA developed by NASA Lewis Research center is based on the minimization-of-free-energy approach to chemical equilibrium calculations. The equilibrium calculations include complex formulas for obtaining thermodynamic and transport mixture properties and thermodynamic derivatives, criteria for condensed phases, calculation at a triple point, ionized species. After Gordon and McBride publication (1998), a calculation of rocket performance for a finite area combustor (FAC) was added to the Chemical Equilibrium with Transport Properties (CET) program [1]. The difference between an infinite and a finite area combustor is presented in Figure 4.2.

The assumptions for the FAC model are one-dimensional form of the continuity, energy and momentum equations, zero velocity at the combustion chamber inlet, complete and adiabatic combustion, isentropic expansion in the nozzle, homogeneous mixing and ideal gas law. The chamber is assumed to have a constant cross-sectional area and the combustion process is a non-isentropic and irreversible.

For FAC model, CEA program allows the equilibrium performance, based on the assumption of *instantaneous chemical equilibrium* during expansion in the nozzle.

Rocket performance is based on the following conservation equation, here Continuity (4.7), Momentum (4.8), Energy (4.9):

$$\rho_2 A_2 u_2 = \rho_1 A_1 u_1 \quad (4.7)$$

$$p_2 + \rho_2 u_2^2 = p_1 + \rho_1 u_1^2 \quad (4.8)$$

$$h_2 + \frac{u_2^2}{2} = h_1 + \frac{u_1^2}{2} \quad (4.9)$$

From the Eq. (4.9), assuming the velocity at the combustion chamber inlet to be negligible to the exit velocity, the exit velocity is computed as:

$$u_e = \sqrt{2 \cdot (h_{inj} - h_e)} \quad (4.10)$$

The procedure involves determining combustion properties using two points, the combustor inlet and the fictitious point 'inf'; the conditions at the end of the combustor and at the throat are determined by an iteration loop. Throat conditions are determined by locating the pressure ratio for which the velocity of flow is sonic; the initial estimate is obtained from the approximate formula:

$$\frac{p_{inf}}{p_t} = \left(\frac{\gamma_s + 1}{2} \right)^{\gamma_s / (\gamma_s - 1)} \quad (4.11)$$

where γ_s is not the specific heat ratio but is defined as:

$$\gamma_s = - \frac{\gamma}{\left(\frac{\partial \ln V}{\partial \ln p} \right)_T} \quad (4.12)$$

From equilibrium properties, u_e^2 using Eq. (4.10) and a_e^2 are calculated and the following convergence test is made:

$$\left| \frac{u_e^2 - a_e^2}{u_e^2} \right| \leq 0.4 \cdot 10^{-4} \quad (4.13)$$

with a_e defined as:

$$a_e = \sqrt{n R T_e \gamma_s} \quad (4.14)$$

In order to obtain the equilibrium Rocket performance, an iteration procedure is required to satisfy the followings:

$$p_{inj} = (p + \rho u^2)_c = \left(p + \frac{\dot{m} u}{A} \right)_c \quad (4.15)$$

obtained by continuity and momentum equation, assuming negligible the injector velocity. For an the present aim, the contraction ratio is assigned and four points are involved in the iteration procedure: injection, infinity, combustion end and throat. Starting with an estimated p_{inf} , calculations are carried out for the others points and a check is made to see if Eq. (4.15) is satisfied with the following tolerance:

$$\frac{p_{inj} - (p + \rho u^2)_c}{p_{inj}} \leq 2 \cdot 10^{-5} \quad (4.16)$$

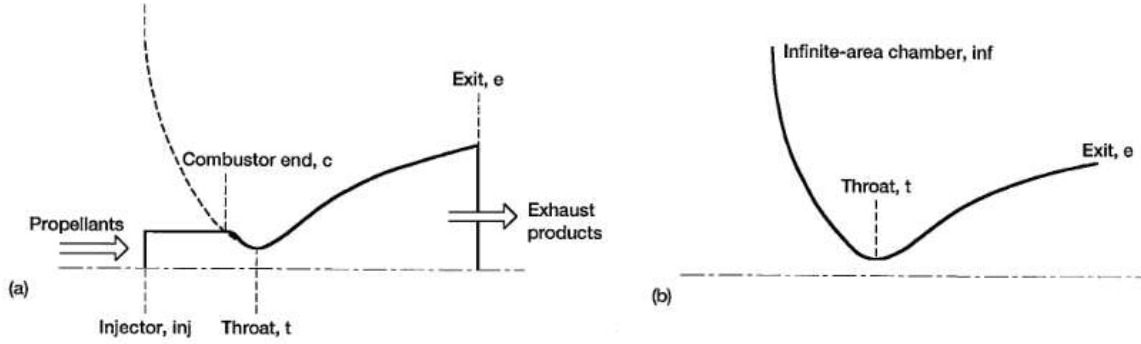


Figure 4.2: Schematics of rocket combustion chamber cross section. (a) Finite-area combustion chamber. (b) Infinite-area combustion chamber. - Gordon [1],1994

4.3 Inverse Heat Transfer Method

The goal of the inverse method for heat conduction is to determine the combustion performance, knowing the heat flux distribution on chamber wall. The algorithm aims to determinate the heat flux boundary condition which best fit the measured temperatures.

Initial temperature is given as input together with a guessed heat flux. After having solved the direct problem, a temperature field is calculated and compared with the measured values. The difference between measured and computed temperatures is given by a residual function. Minimization of the residual leads to optimization of the heat flux problem. The process is iterated until convergence is achieved, hence until the residual decreases under a prefixed value ϵ . The direct problem is solved with a 3D Finite Difference Method and the time integration is carried out with an implicit Euler scheme. The IHTM allows to obtain a time-dependent profile of heat flux and temperature.

The heat conduction PDE is given as follows:

$$\frac{\partial T}{\partial t} = \frac{\lambda}{\rho c_p} \nabla^2 T \tag{4.17}$$

where the constants refer to oxygen-free copper material ($\rho = 8940 \text{ kg/m}^3$, $c_p = 393 \text{ J/(kg} \cdot \text{K)}$, $\lambda = 385 \text{ W/(m}^2 \cdot \text{K)}$). The optimization method is carried put by means of the conjugate gradient optimization so that the heat flux is optimized only at specific locations and at the thermocouples' positions [22].

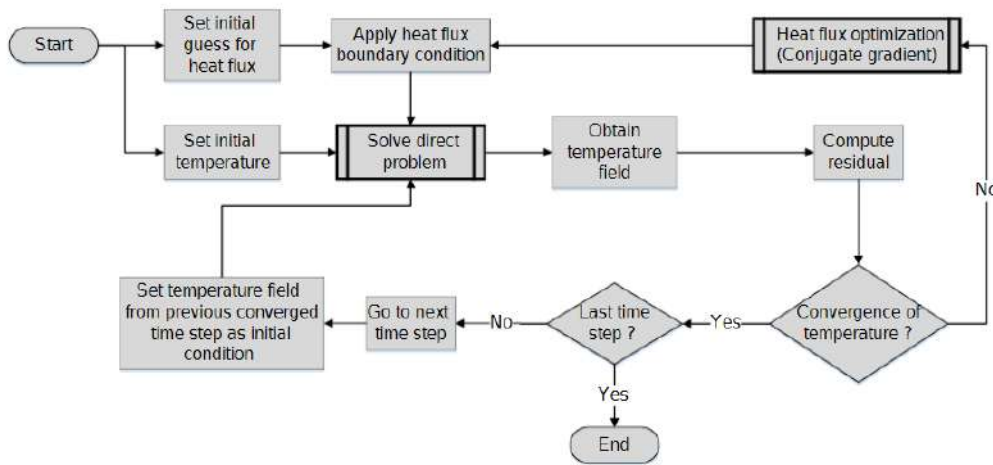


Figure 4.3: Inverse Heat Transfer Method iteration steps.

4.4 Optical methods of evaluation

A wide range of measurement solution are available for combustion and heating process diagnostic. The optical techniques are non-intrusive, high spatial and temporal resolution, modular-structure allowing easy upgrading [23]. One may lists Particle Image Velocimetry (PIV), Laser Induced Fluorescence (LIF), Schlieren method and Chemiluminescence Imaging.

4.4.1 Radiation

Radiation emission is known as a measurable property of a flame. In particular, O_2/H_2 non-premixed flame emit UV radiations from excited OH^* hydroxyl radicals.

Many optical techniques have been implemented for combustion analysis, as mentioned before. In the majority of cases, the access to the flame by laser or illumination sources is hard to achieve. For this reason, the radiation, which is naturally emitted by the flame, is a non-invasive preferred technique. However this method presents some disadvantages: it is a line-of-sight measurement, meaning that a post processing is needed, as well as being not directly associated with a single thermodynamic property.

The flame radiation in terms of OH^* and CH^* radicals is correlated to the heat release rate in non-premixed flames at high pressure and temperature. These radicals are present especially in liquid rocket engine combustors due to the elevate burning temperature [24].

Hence radiation emission is a valuable resource for the study of combustion instability, during which the heat release interacts with the acoustics field, featured by density and pressure fluctuations. Combustion noise is undesirable due to vibrations and thermal loads; pressure oscillation together with the high temperature field leads to a severe structural stress for the combustion chamber. Effective cooling strategies, numerical simulation in early design phases and experimental studies are necessary. If the temperature field and the emission coefficients are known, the emission spectrum, which is the distribution of the emitted radiance depending by the wavelength, may be calculated for a specific molecule. A general excited molecule M^* may be produced by thermal collision with another molecule, absorption of a photon or by a chemical reaction of two substances forming the OH^* species in the excited state, as in Eq. (4.18).

The radiation from the latter case is called *Chemiluminescence*, typical for cold flame up to 2500 K.

Hydrogen flames emit a spectrum which peaks in the blue band; a well known example is the bluish plume of the Space Shuttle Main Engine or the Vulcain Engine. For hydrogen flames the dominant reaction is:



OH^* is know to be in thermal equilibrium above 2700 K and to suffer of severe self absorption at elevate pressure. The intensity of OH^* radiation emitted by a flame is linearly proportional to the pressure and exponentially dependent on temperature.

4.4.2 Chemiluminescence Imaging

Chemiluminesce is hence the emission of light which occurs in presence of a chemical reaction. OH^* emissions are captured by the ICCD camera which set up is described in Section 3.4 and post processed with AVERAGED IMAGES routine.

4.4.3 Averaged Images Routine

The raw images collected by the ICCD camera during the stable burning phase are post processed in order to improving the quality of information that will be extracted.

First, the images are angularly corrected since the overall set up is not perfectly aligned. Hence a resizing of the images is carried out in order to removed everything but the flame itself.

The resizing is a pivotal step which impacts on the averaged image and on the average brightness profile for different axial positions. The code has been implemented by [25] and [26] and modified in some parts for this thesis purpose.

IMAGE IMPORTING The raw images collected by the ICCD camera are imported are post-processed in MATLAB. For a single test, $N = 5$ images taken each 0.5 seconds during the burning time of 2.5 seconds are available for the processing. All N images of a single test are corrected angularly and resized, hence an angle and *BottomLeft* and *TopRight* coordinates are chosen if necessary. Images in 24 bit format need to be indexed to a 8 bit format in order to obtain the colormap; eventually a grayscale conversion and graymap are applied. The indexing, which represent the conversion to an index of brightness, is performed via *rgb2gray* function.

IMAGE PROCESSING An evaluation time and an evaluation window are chosen, which correspond respectively to an n image centered in the evaluated time and to two limiting images which define the range of evaluation. The first image is usually chosen as the *Reference* image.

CHEMILUMINESCE ANALYSIS The reference image is subtracted from all the evaluated images in order to reduce the noise which would compromise the quality of the final analysis, obtaining the *Difference* image. Anyway, this step is not fundamental as explained in Section 4.4.4.

A mean image is calculated among the evaluated images, obtaining an *Average* image and the mean brightness is calculated.

The *Variance* is calculated to show the deviation of the mean image from the raw images and a contour is depicted. The mean, reference, difference and variance images are plotted in the same figure.

Finally the mean brightness (or mean emission intensity) is plotted for different axial distances.

4.4.4 Abel Transform

The inverse Abel transform allows to project an axial-symmetric function onto a plane. If the radial distance r belongs to xy plane, Abel transform is defined as follows:

$$h(y) = \int_{-\infty}^{\infty} f(r) dx = 2 \cdot \int_y^{\infty} \frac{f(r)}{\sqrt{r^2 - y^2}} r dr \quad (4.19)$$

where $h(y)$ is the one dimensional projection which represents the observed/measured data and $f(r)$ is the 2D axial-symmetric function to be determined. After having applied convolution property and Fourier transform, the inverse Abel transform is obtained [27]:

$$f(r) = -\frac{1}{\pi} \int_r^{\infty} \frac{dh(y)/dy}{\sqrt{y^2 - r^2}} dy \quad (4.20)$$

The Abel transform may be analytically extended to three dimensions, obtaining the same formulation as in Eq. (4.20) with $f(r, \rho)$ depending on the cylindrical radius ρ . However it is possible to numerically calculate the radial distribution $f(r)$ for each station along axial direction.

The unknown radial distribution $f(r)$ is expanded in a Fourier-type series:

$$f(r) = \sum_{lof}^{upf} A_n \cdot f_n(r) \quad (4.21)$$

where A_n are the coefficients, lof and upf are the lower and upper frequency of expansion and $f_n(r)$ is a cosine-function:

$$f_n(r) = 1 - (-1)^n \cos\left(n\pi \frac{r}{R}\right) \quad (4.22)$$

Substituting Eq. (4.21) in Eq. (4.19) leads to:

$$H(y) = 2 \sum_{lof}^{upf} A_n \int_y^{\infty} \frac{f_n(r)}{\sqrt{r^2 - y^2}} r dr \quad (4.23)$$

A_n coefficients are calculated by least-squares-fitting of the Abel-transformed series $H(y)$ to the measured data $h(y)$ at each z point along chamber axial direction and for each expansion frequency m . Eq. (4.24) may be written as the linear system in Eq. (4.25):

$$\sum_{lof}^{upf} A_n \cdot \sum_{z=1}^Z (h_z(y) \cdot h_m(y)) = \sum_{z=1}^Z (h(y) \cdot h_m(y)) \quad (4.24)$$

$$[A] \cdot [L] = [B] \rightarrow [A] = [B] \cdot [L]^{-1} \quad (4.25)$$

Among the advantages of this method one may list the followings [28]:

- The method use a derivative-free approach.
- Neither noise smoothing nor any other kind of pre-treatment of the measured data $h(y)$ is necessary.

For this present aim, the resulting images from the inverse Abel transform provide the projected emission intensity distribution along radial distance for different axial positions. In fact the flames emits the light which assume a radial distribution. The radial distribution is hence projected along parallel lines of sight at a certain distance from the origin.

4.4.5 Abel Transform Routine

The *Average* and windowed image for a single test obtained as explained in Section 4.4.3 is given as input to the routine. After having extracted the z axial and x vertical dimensions (previously set as *BottomLeft* and *TopRight*), a 2D mesh is created. Hence the measured of both upper and down half of the image is shown in surface plot; an averaged projection is shown as well.

After having chosen the minimum and the maximum frequency of expansion, namely *lof* and *upf*, the $[A]$ matrix is computed as in Eq. (4.25) separately for top and bottom half and for the average projection.

Hence the inverse Abel transform $f(r)$ is calculated by Eq. (4.21) for each axial point and for upper, down half and average part. A normalization is carried out with the maximum emission intensity of all tests at 20 bar pressure level.

Although the test have been performed at the same nominal OF value equal to 3.4, the obtained values range between 3.0 and 3.6: hence a comparison among different mixture ratio may be carried out.

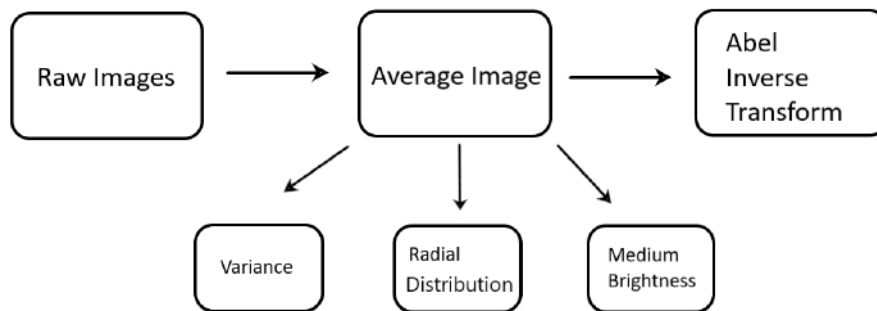


Figure 4.4: Image post-processing steps.

Chapter 5

Operating Conditions

5.1 Cold Flow Test Campaign

The aim of the Cold Flow tests campaign is to obtain the LOX mass flow rate plotted over the oxygen tank relative pressure. The oxygen tank relative pressure value has to be known in order to perform the Hot Fire tests. For a specific nominal chamber pressure and OF ratio, knowing the throat area A_{th} and the nozzle discharge coefficient c_D , LOX mass flow rate for Hot Fire test is given by Eq. (5.1). The characteristic velocity c^* is known from the from NASA CEA calculations selecting ROCKET Problem type at the corresponding conditions of nominal chamber pressure p_c , OF, contraction ratio ϵ_c and injection temperature of both fuel and oxidizer.

$$\dot{m}_{LOX} = \left(\frac{1 + OF}{OF} \right) \cdot \frac{p_c \cdot A_{th}}{c^*} \cdot c_D \quad (5.1)$$

The relative tank pressure $p_{tank,r}$ is read from the plot presented in Figure 5.2, thus the tank absolute pressure is computed by Eq. (5.2) and manually set by means of the oxygen pressure regulator during the Hot Fire tests.

$$p_{tank,a} = p_{tank,r} + \eta_{c^*} p_c - p_{amb} \quad (5.2)$$

The pressure $p_{tank,a}$ is the tank absolute pressure ¹, $p_{tank,r}$ is the tank pressure relative to $PC0$, the first pressure measurement at the combustion chamber injection section. For Cold flow tests $PC0$ is equal to the ambient pressure. The nominal chamber pressure is p_c and p_{amb} is the ambient pressure. The c^* -efficiency η_{c^*} is estimated at 0.975% for all tests.

5.1.1 Cold Flow Evaluation

The Cold Flow tests provide experimental data points represented in Figure 5.1. Each point represents a single test performed at different $p_{tank,a}$ ranges between 6 and 28 bar. A single point corresponds to the mean LOX mass flow rate measured value and the mean static tank pressure relative to the ambient pressure averaged over the evaluated time window. Each operating pressure is run more than once to ensure the reliability of the data. Some of the run tests have not been chosen for the evaluation due to insufficient liquid oxygen: thus the liquification process had to be restarted at the proper tank pressure. The Cold Flow tests presented in Table 5.1 have been carried out and chosen for the evaluation.

Nominal total tank pressure	PTANK0	[bar]	6	10	13	15	17	18	20	22	23	25	28
Number of repetitions	N	[-]	6	5	4	5	5	4	1	2	1	6	3

Table 5.1: Cold Flow evaluated tests without the combustion chamber.

¹ $p_{tank,a}$ pressure is absolute in the meaning that is the sum of chamber pressure and tank pressure. However the tank absolute pressure is still relative to the ambient pressure

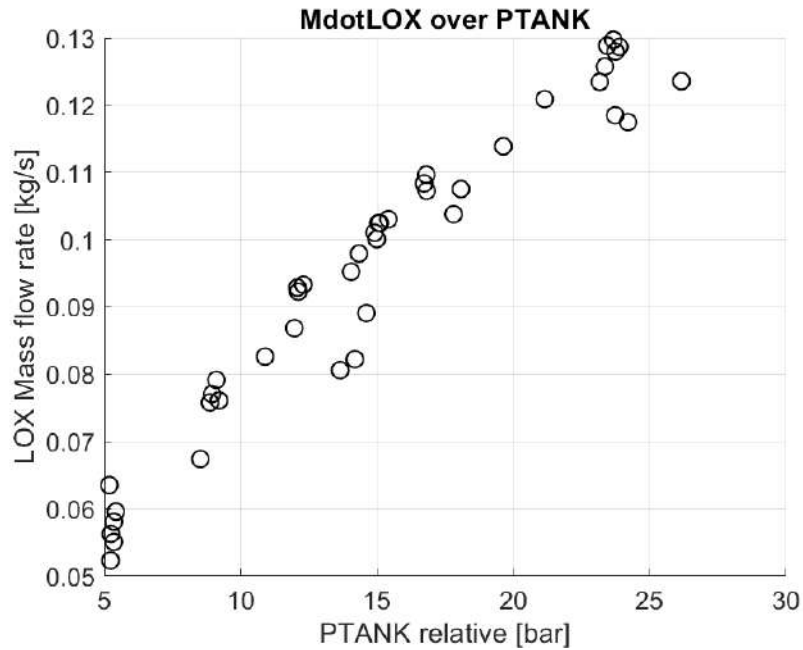


Figure 5.1: Liquid oxygen mass flow rate points over tank pressure relative to the ambient pressure

The evaluated time window is fixed time interval equal to 0.5 s, whereas the evaluated time is chosen wherein the correct temperatures are reached. To ensure the correct temperature values, LOX main valve upstream and downstream temperatures, namely $TO2$ and $TO3$, are checked for each single test. The values of the temperature are compared to the oxygen phase-diagram: if temperature and pressure values across the main valve MVLOX ensure a liquid phase across the main valve, the test is evaluated.

After the suitable evaluation time has been chosen and the LOX mass flow rate has been computed for each test, all values are plotted. The LOX mass flow rate curve over the oxygen tank relative pressure is obtained with a least squares fitting of a square distribution of the experimental data. Pressure is square-root dependent variable of mass flow rate, as expected from Eq. (2.30). Hence the curve in Figure 5.2 is obtained.

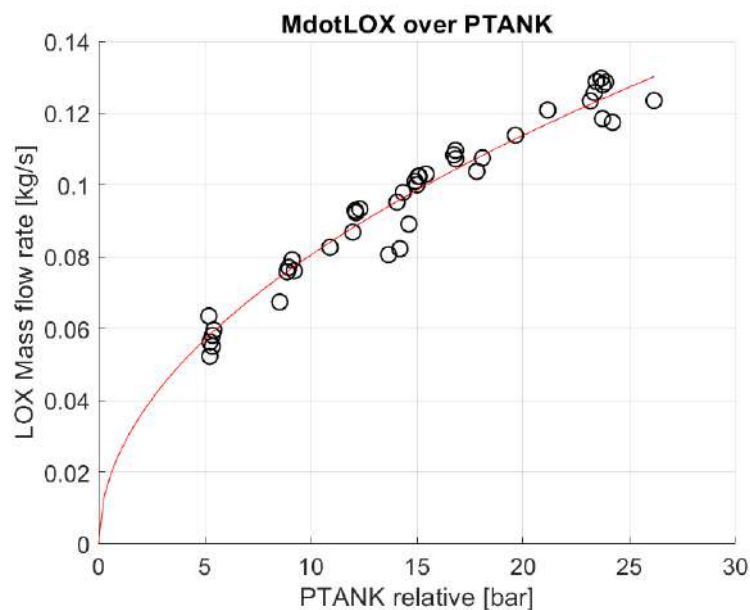


Figure 5.2: Liquid oxygen mass flow rate curve over tank pressure relative to the ambient pressure.

5.1.2 Cold Flow Procedure

Liquification process

The first step consists in producing liquid oxygen by means of the liquifier. One liquid nitrogen tank is connected to air supply and pressurized at 1 *bar*, as shown in Figure A.16a. Liquid nitrogen completely fills the outer tank of the liquifier to ensure a sufficient amount of liquid oxygen produced inside the inner tank depicted in Figure A.16b. The gaseous oxygen tank pressure for the liquification process is set at 4*bar* by means of the handle wheel of the oxygen pressure regulator. Once that the outer tank is filled with liquid nitrogen, the air cable is decoupled from the liquid nitrogen tank.

Liquid nitrogen precooling

The second dewar of liquid nitrogen depicted in Figure A.17 is self-pressurized and set at 1.5 bar, aiming to precool the main line.

The yellow handle allows gaseous nitrogen to be released at the end of the test session, the green handle allows the desired pressurization level, whose value is readable on the pressure gauge. The second gauge indicates the remained volume of liquid nitrogen. The red handle allows liquid nitrogen to flow through the line. Once that the pressurization level is reached the green handle is closed.

With the supply valve closed and both the main valve and the bypass valve closed, the line is initially pre-cooled up until the main valve. Then both the main valve and the bypass valve are opened to precool the injection section and the bypass line, respectively.

When temperature measurements show a sufficient low value, i.e. $TO2 \sim TO3 \approx 90 K$, the precooling phase is concluded. To end the precooling phase, liquid nitrogen and pressurization valve are closed. Gaseous nitrogen valve is opened to release nitrogen after the last has been performed. LOX main valve and the bypass valve are closed to proceed with following phase.

Cold Flow test

In this phase, the supply valve is opened to let liquid oxygen flow down until the main valve. Liquid oxygen main valve is initially closed, hence the Cold Flow test can start.

A short precooling with liquid oxygen is performed by opening and closing the main valve.

Test data are collected starting LabView recording. Main valve is opened for approximately 3 s. After closing the main valve, LabView data collection is ended. The sequence file is generated by LabView and given as input to the MATLAB routine.

5.2 Hot Fire Test Campaign LOX/CH4

To set the desired propellants mass flow rates, hence the selected OF ratio, the pressure regulators are manually operated both for oxygen and methane supply line.

The operative sequence is programmed in LabView shown in Appendix B.3.

5.2.1 Load Points

The present test campaign is performed for the following values of nominal chamber pressure and nominal OF ratios:

p_c	[bar]	5	5	5	5	10	10	10	10	20	20	20	20
OF	[-]	2.2	2.6	3	3.4	2.2	2.6	3	3.4	2.2	2.6	3	3.4

Table 5.2: Nominal load points for LOX/CH4 Test Campaign.

The theoretical characteristic velocity c_{th}^* , which is a function of the nominal pressure and OF ratio, is calculated with NASA CEA tool and used for the total mass flow calculation as follows:

$$\dot{m} = \frac{p_c \cdot A_{th} \cdot c_{D,N}}{c^*} \quad (5.3)$$

where p_c is the nominal value of the chamber pressure, A_{th} is the throat section area of the thrust chamber and $c_{D,N}$ is the nozzle discharge coefficient.

From the OF definition, fuel mass flow rate is computed as:

$$\dot{m}_f = \frac{\dot{m}}{OF + 1} \quad (5.4)$$

Using the ideal gas law and assuming Mach number equal to 1 at the fuel orifice throat, the total absolute pressure is calculated:

$$p_{f,a} = \frac{\dot{m}_f}{c_{D,f} \cdot A_f} \cdot \sqrt{\frac{R_f \cdot T}{k_f}} \cdot \left(\frac{k_f + 1}{2} \right)^{\frac{k_f + 1}{2(k_f - 1)}} \quad (5.5)$$

with $c_{D,f}$ and A_f that are the orifice discharge coefficient and the orifice throat area, respectively. The heat capacity ratio k_f is computed at the nominal pressure p_c and at the ambient pressure T . Hence the relative total pressure is calculated and given as input to the fuel pressure regulator valve:

$$p_{f,r} = p_{f,a} - p_{amb} \quad (5.6)$$

The same procedure is implemented for the nitrogen film cooling mass flow rate, knowing that the film mass flow rate \dot{m}_F is a percentage of the fuel mass flow rate \dot{m}_f . Film orifice geometry is known, the discharge coefficient $c_{D,F}$ of the film orifice is set equal to 1 and the heat capacity ratio is calculated for the nominal conditions and gaseous nitrogen properties.

$$\dot{m}_F = \%_F \cdot \dot{m}_f \quad (5.7)$$

Hence the total absolute pressure is calculated as:

$$p_{F,a} = \frac{\dot{m}_F}{c_{D,F} \cdot A_F} \cdot \sqrt{\frac{R_F \cdot T}{k_F}} \cdot \left(\frac{k_F + 1}{2} \right)^{\frac{k_F + 1}{2(k_F - 1)}} \quad (5.8)$$

The relative total pressure obtained from Eq. (5.9) is set by means of the handle wheel of the nitrogen pressure regulator.

$$p_{F,r} = p_{F,a} - p_{amb} \quad (5.9)$$

The relative total pressure is computer for each load point presented in Table 5.2 both for fuel and film cooling. The relative total pressure for liquid oxygen is obtained as described in Section 5.1.

5.2.2 Igniter load point

The igniter operates with oxygen and methane as described in subsection 3.2.2. Hence for the nominal conditions presented in Table 5.3, the relative total pressure for both fuel and oxygen are computed and set by means of the corresponding pressure regulators.

p_c	[bar]	7
OF	[-]	2.5

Table 5.3: Nominal load point for spark torch igniter

5.3 Hot Fire Test Campaign LOX/GH2

The approach described in 5.2 is implemented for LOX/GH2 test campaign as well.

5.3.1 Load Points

The present test campaign is performed for the nominal load points presented in Table 5.4.

p_c	[bar]	5	5	5	5	10	10	10	10	20	20	20	20
OF	[-]	4.4	5.2	6.0	6.8	4.4	5.2	6.0	6.8	4.4	5.2	6.0	6.8

Table 5.4: Nominal load points for LOX/H2 Test Campaign.

5.3.2 Igniter load point

The igniter operates with oxygen and hydrogen. Hence for the nominal conditions presented in Table 5.3, the relative total pressure for both fuel and oxygen are computed and set by means of the corresponding pressure regulators.

p_c	[bar]	7
OF	[-]	4

Table 5.5: Nominal load point for spark torch igniter for LOX/H2 Test Campaign.

5.3.3 Hot Fire Test Procedure

Pressure Setting

Gaseous oxygen, gaseous methane tanks bundle are opened, as well as the gaseous nitrogen tank. The maximum pressure within bundles are 300 bar.

For a selected load point, pressure is manually set as in Figure A.2b at nitrogen pressure regulator for film cooling (green down left), oxygen pressure regulator (black right), methane pressure regulator (black left), oxygen pressure regulator for igniter (green up left) and oxygen pressure regulator for igniter (green right). See Figure A.1 in Appendix A.0.2.

The line is hence purged with gaseous nitrogen.

Oxygen Liquification

Liquid oxygen is obtained with liquefaction as described in subsection 5.1.2.

Since the phases before the combustion chamber burn take a certain amount of time, the level of liquid nitrogen has to be monitored to ensure the liquid oxygen formation. In case of low level, the air cable is attached to pressurize the tank.

Liquid nitrogen precooling

The precooling phase is operated as described in subsection 5.1.2. At the end of the precooling, liquid nitrogen supply line is closed. The bypass valve and the main valve are closed.

Supply valve opening

The supply valve is opened and pressure values of the sensors PTANK and PO₂ are checked to verify that the pressure is equalized.

PTANK is increased from the liquification pressure of 4 bar to the desired pressure obtained in Eq. (5.2).

Ignition and burning

The igniter is manually switched on as showed in Figure A.4d. The camera record is started and the test sequence name is shown in front of the camera.

Two precooling are performed with liquid oxygen by opening LOX main valve.

The permission for Hot Fire is requested and the ignition sequence is started in LabView.

Conclusive Tasks

The camera record is stopped right before switching off the igniter.

The supply valve is closed and the by pass valve is opened to release the liquid oxygen remained in the line.

The absolute oxygen tank pressure is decreased to 4 bar for starting a new liquification phase. Hence the liquid nitrogen tank is connected to the air pressurization for the following test.

Once that liquid nitrogen outer tank is filled, the air cable is detached and attached to the air supply to externally cool the chamber.

When all the daily tests have been performed, the pressure regulators are set to zero bar and the bundles are closed and disconnected. The discharge upstream lines and the relief valve on top of inner liquifier tank are opened and let opened during the night. Liquid oxygen bypass valve and gaseous nitrogen discharge of LN₂ dewar are opened and let opened during the night as well.

Chapter 6

Results and Analysis

6.1 Cold Flow Test

The following Cold Flow test is performed at the nominal total oxygen tank pressure PTANK of 17 bar.

Since the tank pressure is manually set at the oxygen pressure regulator, the real value is different from the nominal point.

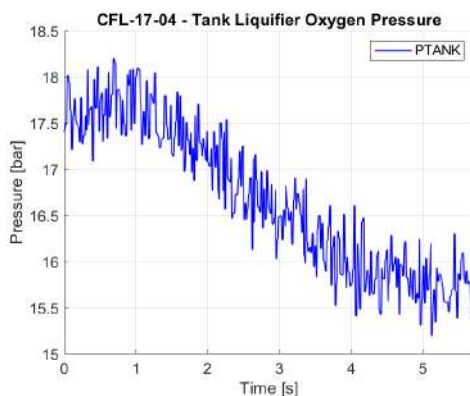
Figure 6.1a shows the tank pressure profile over the complete testing time.

One may notice that the initial value corresponds to the total, or stagnation, tank pressure since the fluid velocity inside the oxygen tank is zero.

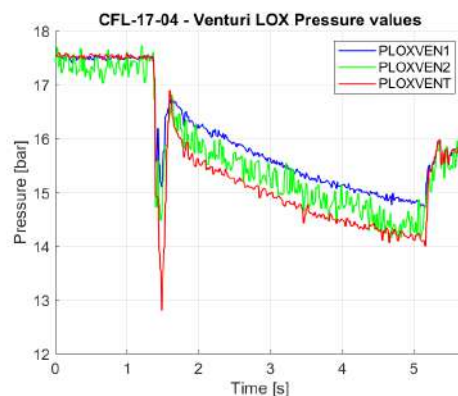
The measured value is equal to 17.7 bar, averaged from 0 to 1 seconds. The fluctuations in the pressure profile are imputable to the noise of the pressure transducer, whose offset remains lower than 1 bar.

Due to the fact that some amount of liquid oxygen is consumed during the test, gaseous oxygen inside the inner tank of the liquifier expands: hence the tank pressure decreases of up 10% from the initial value as in Figure 6.1a.

The pressures measured within the Venturi meter are shown in Figure 6.1b. The Venturi upstream pressure measured by PLOXVEN1 sensor shows a higher value than the value measured at the throat section, as expected. PLOXVENT registers the pressure drop as the fluid flows through a smaller section. The velocity at the throat section increases according to mass continuity, as previously computed in Eq. (3.4), hence the pressure decreases. The Venturi downstream pressure measured by PLOXVEN2 is higher than the throat pressure due to the increased area, but is lower than the upstream value due to line losses equal to 0.5 bar across the mass flow meter.



(a) Tank pressure profile during testing time.



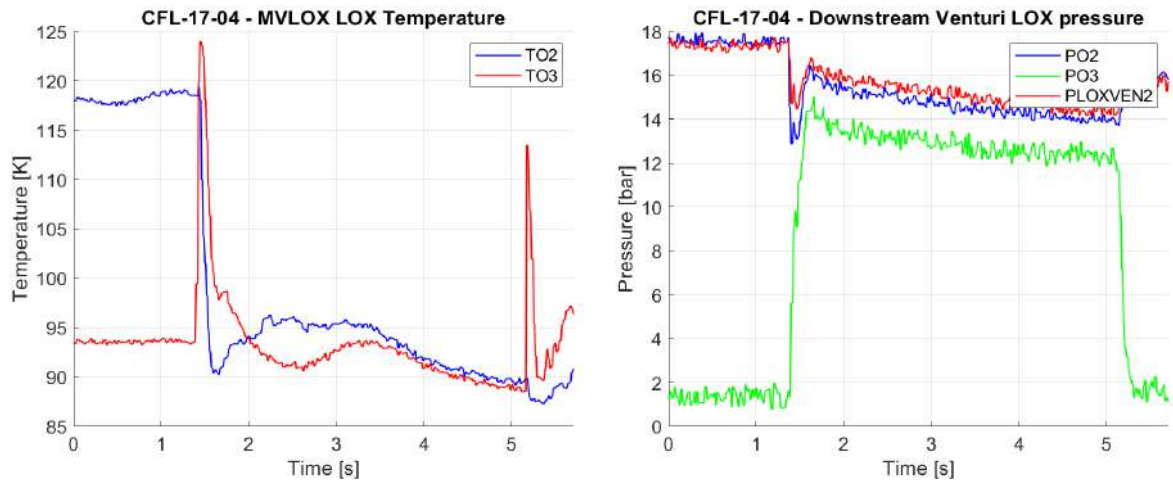
(b) Pressure profile within Venturi mass flow meter.

PLOXVEN2 sensor shows the pressure measured downstream the Venturi meter which trend follows the pressure upstream the LOX main valve PO2. Since the line is pressurized at a pressure equal to PTANK up until the main valve, the initial value is constant until the main valve remains closed.

A rough pressure decrease is recognizable at $t = 1.5$ s corresponding to main valve opening time and to the liquid oxygen increasing velocity. The slight different in pressure between PO2 and PLOXVENT2 during the test time from $t = 1.5$ s to $t = 5$ s is due to pressure line losses.

The pressure downstream the main valve measured by PO3 shows an initial value equal to the ambient pressure. Once that the main valve is opened, liquid oxygen pressure tends to reach the same value of the upstream flow.

However the pressure drop across the valve may be estimated equal to 2 bar, rather constant over the test time.



(c) Temperature upstream and downstream the MVLOX. (d) Pressure upstream and downstream the MVLOX - Pressure downstream Venturi meter.

Figure 6.1: Temperature and pressure profile through the MVLOX valve

The evaluation time is chosen after having ensured the liquid phase of the oxygen through the main valve. The values registered by the thermocouples TO2 and TO3 are examined, as well as the the pressure measurements PO2 and PO3, and compared with the oxygen saturation pressure in Figure 6.2.

The Figure 6.1c shows a constant value of 90 K from $t = 4$ s to $t = 5$ s; hence an evaluation time equal to $t = 4.3$ s is chosen with an evaluation window equal to ± 0.25 s.

From Figure 6.1c one may notice that the temperature downstream the main valve TO3 is lower than the upstream temperature TO2. From the test label CFL-17-04, one may recall that the test performed was the fourth consecutive at 17 bar. Hence the main valve had been previously opened three times, cooling down the downstream section whereas TO3 sensor is placed. Furthermore, the first test is always preceded by a short LOX pre-cooling phase, as described in Section 5.1.2.

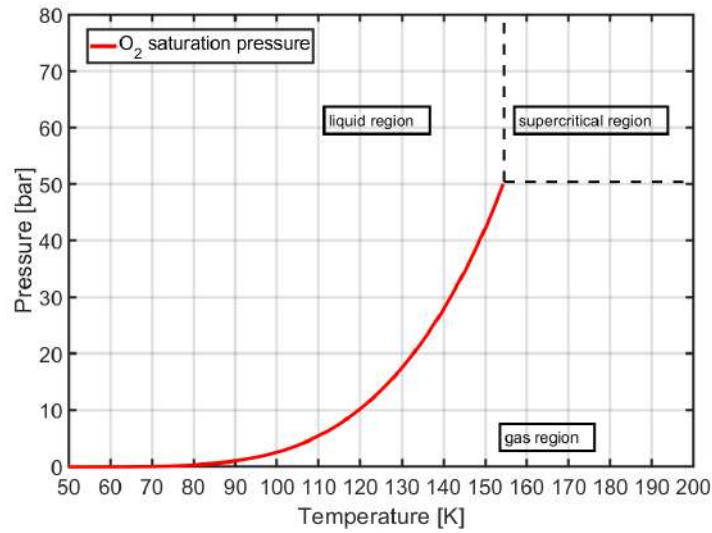


Figure 6.2: Saturation pressure curve for oxygen.

The LOX mass flow rate is computed as explained in Eq. (3.6) and plotted in Figure 6.3. The profile is constant during testing time with a peak corresponding to main valve opening and to liquid oxygen increasing velocity. During the testing time, LOX mass flow rate appears to be constant and equal to $\dot{m}_{LOX} = 100 \text{ g/s}$.

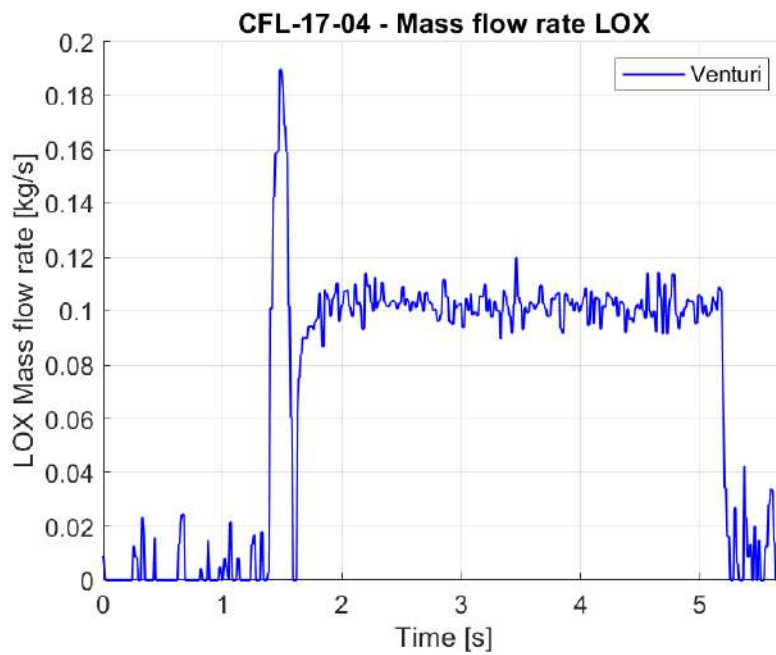


Figure 6.3: Liquid oxygen mass flow rate measured by Venturi meter during testing time.

6.2 Hot Fire Test Campaign LOX/CH4 with copper window

The following Hot Fire test TMC-20-34-30-20-5 is performed for the nominal point presented in Table 6.1. TMC label indicates *Test* with *Methane* as fuel and with *Copper* window. The first number 20 refers to the nominal chamber pressure, the second number 34 to selected OF ratio, the third number 30 to the burning time, the fourth number 20 to percentage of film cooling mass flow rate and the last number 5 is the number of the repetition of the test at the same conditions.

p_c	OF	t	$\%_F$	n°
[bar]	[-]	[s]	[-]	[-]
20	3.4	3.0	20	5

Table 6.1: Nominal load point for TMC-20-34-30-20-5 test.

6.2.1 Pressure setting

For the present nominal point liquid in Table 6.1 oxygen mass flow value is calculated as in Eq. (5.1) and PTANK pressure is calculated by Eq. (5.2) using the curve presented in Figure 5.2 obtained after the Cold Flow test campaign.

The calculations are carried out to get an idea of the value of pressure that has to be set at the corresponding pressure regulator. Despite a good agreement is expected between calculations and experimental results, pressure setting values can be adjusted after having analysed mass flow rate results and combustion efficiency values.

Hence the pressure is manually set at the oxygen pressure regulator. The pressures for methane and nitrogen line are manually set as described in section 5.2.1. Finally the igniter pressures are set according to igniter load point in Table 5.3.

Pressure are manually set at pressure regulators presented in the column of Table 6.2: the correct pressure value is ensured by opening the corresponding valve in the second column and reading the value shown by the corresponding pressure sensor in LabView, reported in the third column.

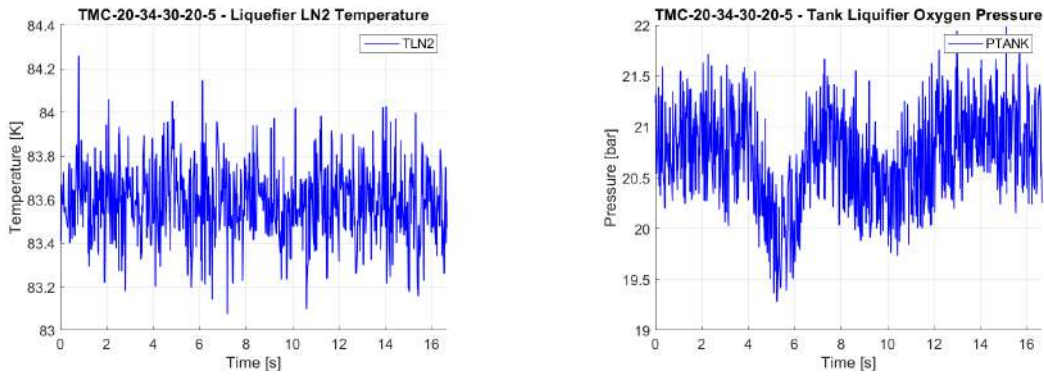
All the pressure values are considered relative to the ambient pressure.

PRESSURE REGULATOR	VALVE	UPSTREAM SENSOR		UNITS	VALUE
-	-	-	LOX mass flow rate	\dot{m}_{LOX} [g/s]	48.77
-	-	-	Relative OX tank pressure	$p_{tank,r}$ [bar]	2.25
-	-	PUMG	Ambient pressure	p_{amb} [bar]	0.96
DMO	MVLOX	PTANK	Absolute OX tank pressure	$p_{tank,a}$ [bar]	20.75
-	-	-	CH4 mass flow rate	\dot{m}_f [g/s]	14.34
DMM	MVM	PM2	Relative CH4 tank pressure	$p_{f,r}$ [bar]	52.74
-	-	-	GN2 film cooling mass flow rate	\dot{m}_F [g/s]	2.87
DMN	MVNZ	PF1	Relative GN2 tank pressure	$p_{F,r}$ [bar]	40.54
DMOZ	MVOZ	POZ	Relative OX pressure for igniter	$p_{ZO,r}$ [bar]	16.12
DMMZ	MVMZ	PMZ	Relative CH4 pressure for igniter	$p_{ZM,r}$ [bar]	19.17

Table 6.2: Nominal mass flow and pressure values for TMC-20-34-30-20-5 test.

6.2.2 Liquifier tanks measurements

Liquid nitrogen temperature in Figure 6.4a is measured by thermocouple K positioned inside the outer tank of liquifier. Temperature value reveals a liquid phase and a constant profile during the entire running test. Figure 6.4b shows the pressure profile inside oxygen tank. The profile shows a sudden decrease from $t = 4.5\text{ s}$ which corresponds to precooling phase with liquid oxygen. During the burning phase from $t = 7\text{ s}$ to $t = 10\text{ s}$, the pressure decays of approximately 1 bar, with a similar trend to the Cold flow plot in Figure 6.1a.

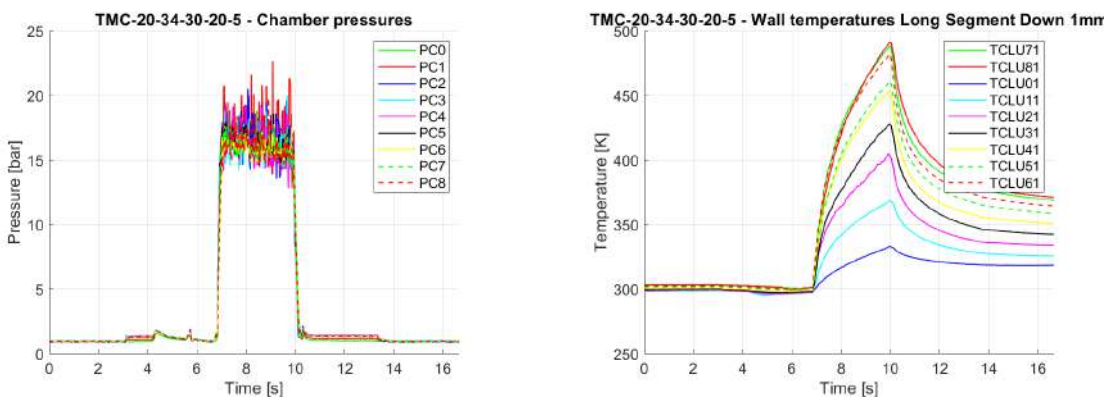


(a) Liquid nitrogen temperature inside the liquifier. (b) Oxygen tank pressure profile relative to the ambient.

6.2.3 Chamber temperature and pressure distribution

The chamber pressure measurements presented in Figure 6.4c show an average value equal to 16 bar whereas burning phase is running. The high fluctuations presented by all the pressure sensors highlight a rough combustion process. The roughness of the combustion together with the low medium chamber pressure achieved equal to 17 bar anticipates a loss in combustion performance. The pressures profile displays perturbations at time $t = 4.5\text{ s}$ due to film cooling mass flow rate interaction with liquid oxygen mass flow rate during last cooling phase.

The temperature profile show a steep gradient whereas ignition time occurs, here at time $t = 7.1\text{ s}$, and a peak equal to 480 K , at combustion end phase at time $t = 10\text{ s}$. From Figure 6.4d one may note that the highest values is reached by the thermocouples furthest downstream the injector.



(c) Pressure profile within combustion chamber. (d) Temperature profile within combustion chamber.

Figure 6.4: Combustion chamber measurements versus running time.

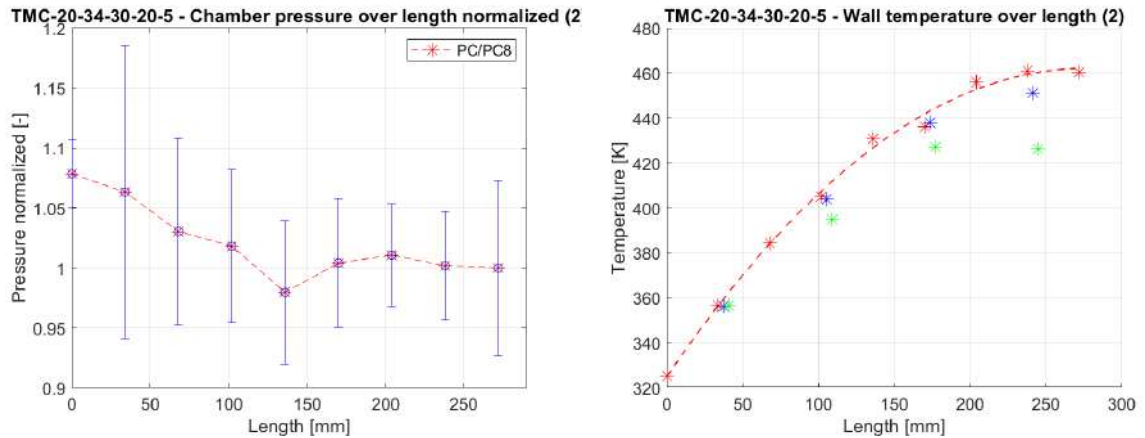
6.2.4 Chamber pressure and temperature distribution over length

Due to combustion process, heat is release and the temperature of mixture increases as well as its velocity. Hence the pressure decreases along the axial length of the combustion chamber. In Figure 6.5a the chamber pressures values for all 9 pressure sensors are plotted at a fixed time with relative uncertainties as described in Appendix A. The values are averaged over the evaluation window, centered in the evaluation time equal to $t = 8.9$ s for the present test.

In Figure 6.5a the chamber pressures over length are normalized to the last pressure sensor PC8: a decrease up to 7% is registered along the axial dimension. The dropping in static occurs also due to heat losses through chamber walls, friction losses and incomplete combustion mechanism.

Figure 6.5b shows, for a fixed instant of time, the temperature distribution along chamber z-axis measured by the thermocouples positioned within the first and the second segment of the combustion chamber at 1 mm from the wall. A continuous rise in wall temperature is detectable along the chamber length until a maximum is reached at position $z = 270$ mm whereas the combustion process appears to end.

The temperature values registered from the thermocouples placed at 2 mm and 3 mm from the wall represented respectively in blue and green show lower values, as predictable.



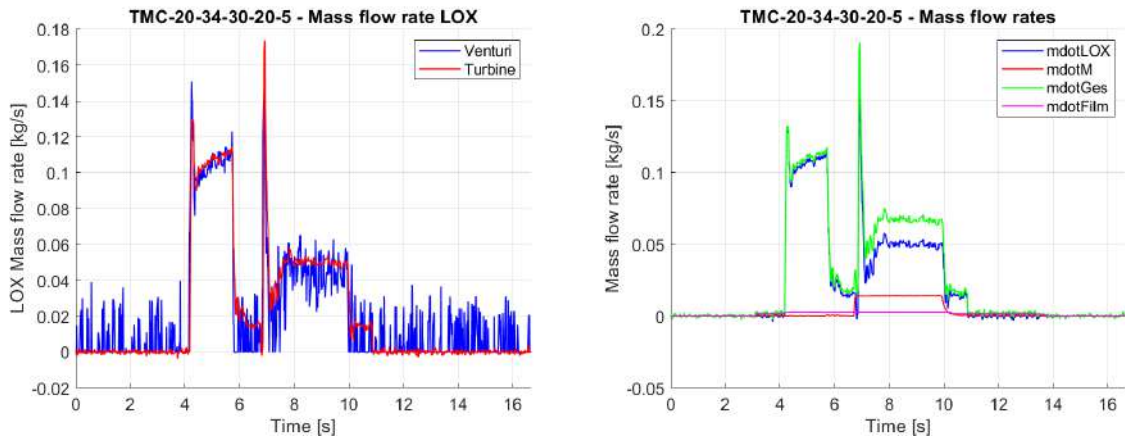
(a) Chamber pressure measurements along chamber length normalized with the last pressure sensor PC8. (b) Chamber temperature measurements along chamber length fitted for 1mm from the hot side wall measurements.

Figure 6.5: Normalized pressure and temperature profile along chamber axis.

6.2.5 Mass flow rate distribution

LOX mass flow rate displayed in Figure 6.6 is calculated thanks to the Venturi meter and measured with the turbine, as described in Section 3.6.1. The LOX mass flow rate in Figure 6.6a shows a peak at time $t = 4\text{ s}$ when MVLOX is opened for the precooling phase. During this phase, LOX reaches a pressure of 16 bar visible in Figure 6.7a and the mass flow rate ranges around 100 g/s , making reproducible the result obtained during the Cold Flow test in Figure 6.3. A second peak is registered at MVLOX opening corresponding to burning phase starting. During burning time from $t = 7\text{ s}$ to $t = 10\text{ s}$, mass flow rate profile is constant especially for turbine measurements, while Venturi meter shows an high fluctuation.

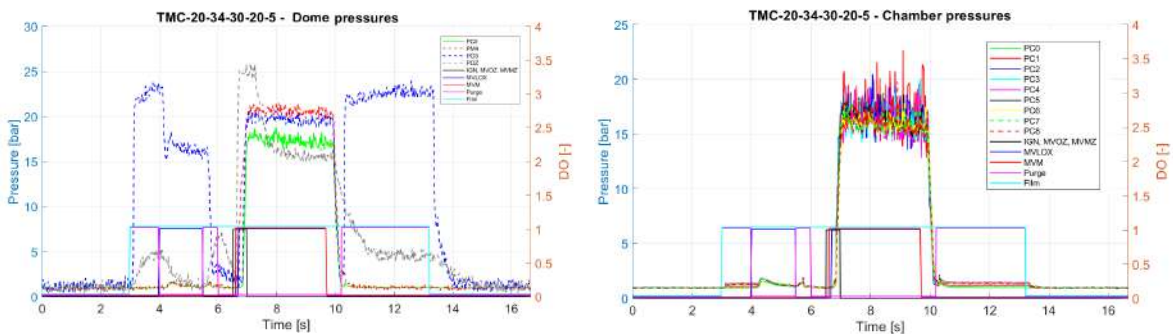
Gaseous mass flow rate as $mdot_{Film}$ and $mdot_M$ values in Figure 6.6b are calculated using ideal gas law, as described in Section 4.2.1.



(a) Liquid oxygen mass flow rate.

(b) Liquid oxygen, methane, total and film mass flow rates.

Figure 6.6: Mass flow rates



(a) Dome pressures profile over testing time with DO signals.

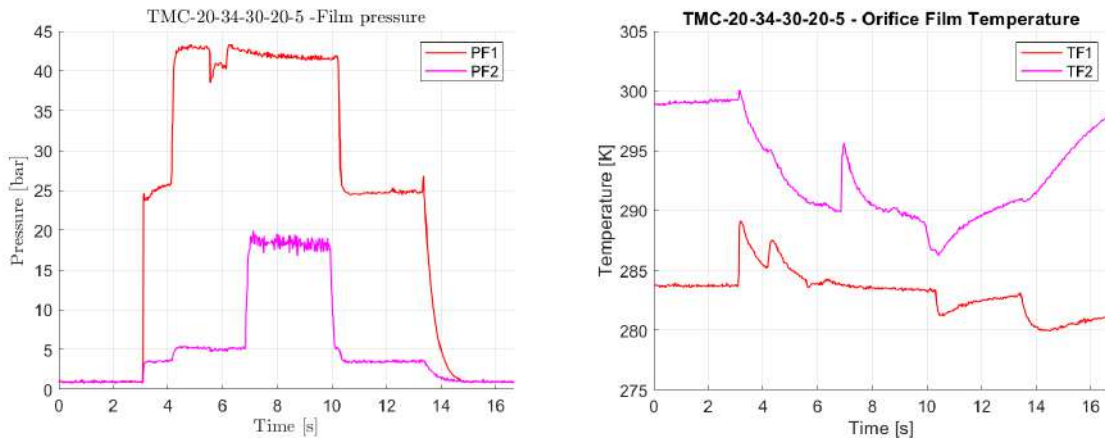
(b) Chamber pressure profile over testing time with DO signals.

Figure 6.7: Pressure profile over testing time with DO signals.

6.2.6 Film cooling pressure and temperature distribution

The pressure measurements for nitrogen film cooling upstream and downstream the orifice are presented in Figure 6.8a.

The downstream film temperature TF2 decrease whereas cooling phase with liquid oxygen is carried out. The peak at time $t = 7 \text{ s}$ corresponds to ignition time and highlights the combustion reaction starting. However one may notice an anomaly in Figure 6.8: downstream temperature TF2 is higher than upstream temperature TF1 for the entire running time. The initial TF2 value equal to 298 K proves that after several performed tests, the thermocouple is sitting directly on chamber hot wall. A correct film temperatures profile should show the same initial value equal to 270 K and TF2 higher than TF1 during burning time due to nitrogen interaction with combustion products.



(a) Pressure profile versus running time upstream and (b) Temperature profile versus running time upstream and downstream film cooling orifice.

Figure 6.8: Pressure and temperature measurements upstream and downstream nitrogen orifice.

6.2.7 Oxidizer to fuel ratio

From Figure 6.9 one may notice that the obtained OF corresponds with a good approximation to the nominal value equal to 3.4 during the evaluation window.

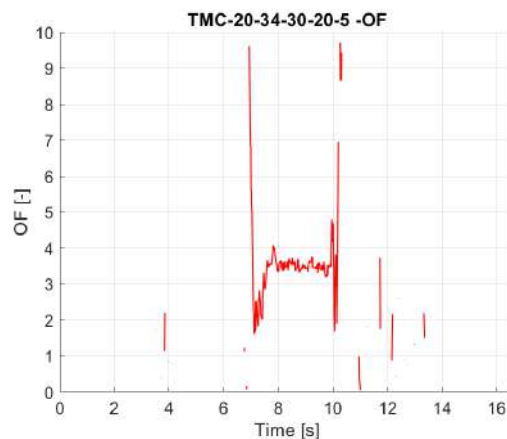


Figure 6.9: Oxidizer to fuel ratio during burning time.

	IDEAL	EXPERIMENTAL	UNITS	DEVIATION
\dot{m}_{LOX}	48.77	49.81	[g/s]	2.1 %
\dot{m}_{CH4}	14.34	14.28	[g/s]	0.42 %
v_{LOX}	6.02	6.33	[m/s]	5.1 %
v_{CH4}	116.18	134.33	[m/s]	15.6 %
VR	19.30	21.23	[-]	10 %
J	4.88	6.48	[-]	32.7 %
OF	3.4	3.48	[-]	2.35 %

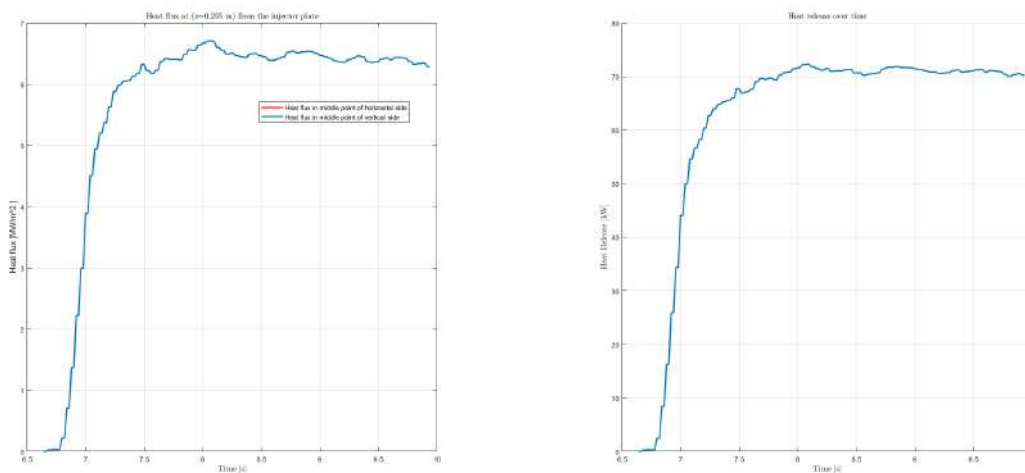
Table 6.3: Ideal and obtained quantities for TMC-20-34-30-20-5 test at the evaluation time.

From Table 6.3 a good agreement between theoretical values and obtained values from the TMC-20-34-30-20-5 test. The higher deviation is registered for the methane mass flow rate which in turns impacts on velocity ratio VR high deviation. Despite methane mass flow rate is slightly lower than expected, the velocity results higher due to the lower value of pressure achieved at the injector which impacts on fuel density. In computing OF ratio, liquid oxygen mass flow rate plays the biggest role: the resulting deviation is hence acceptable and equal to 2.35 %.

An increase in the velocity ratio VR or in the momentum flux J ratio leads to a smaller spreading angle and a more constricted flame, since the velocity of the methane flow is higher. The LOX core is denser and slower, however it is influenced by the methane velocity especially at the injection plane.

6.2.8 Heat flux distribution

The heat flux is analyzed in Figure 6.10a for a specific axial position equal to $q(t)_z = 0.255$ whereas the combustion process starts to end and for the middle point on the vertical y axis. The heat flux profile starts increasing when ignition occurs and continue to rise for approximately 500 ms. After some oscillations a constant value is reached from $t = 8.25$ s. Hence the heat flux is integrated over the chamber walls surface obtaining the heat release over time shown in Figure 6.10b.



(a) Heat flux distribution at position $z=0.255$ from the injector plate.

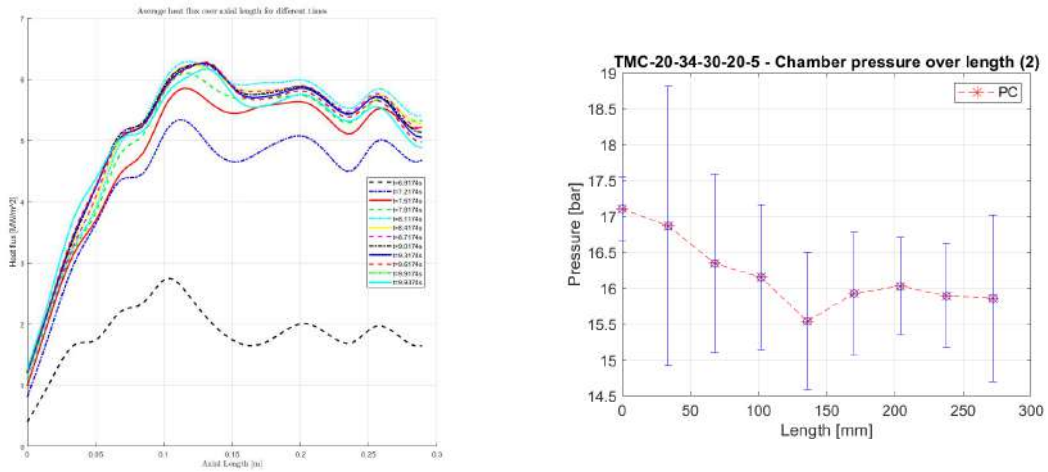
(b) Heat release over time.

Figure 6.10: Heat flux and heat release profile over time.

When analyzing Figure 6.11a, the highest value is registered for the last instant of time equal to $t = 9.93 \text{ s}$ until the first oscillation occurs at the axial position $z = 70 \text{ mm}$. After the second oscillation at $z = 130 \text{ mm}$, the highest values is registered for the time $t = 8.12 \text{ s}$ which best approach the evaluation time. The lowest value correspond to ignition time equal to $t = 6.91 \text{ s}$ when propellants have not yet reacted, as can be also seen in Figure 6.7b.

The heat flux peak is equal to 6.2 MW/m^2 occurring at position $z = 130 \text{ mm}$ along chamber axis. Along second segment, the heat flux show oscillation and a general decrease when considering the evaluation time.

When comparing the heat flux distribution over length with pressure over length, the heat flux maximum is reached whereas the pressure shows a minimum, as shown in Figure 6.11b at position $z = 130 \text{ mm}$. Afterwards, since the combustion is ended, no additional heat is released to accelerate the flow.



(a) Heat flux profile over length for different times averaged for horizontal positions.

(b) Pressure distribution over chamber length.

Figure 6.11: Heat flux profile over length for different film cooling percentage.

In Figure 6.12 the temperature field pattern is shown at $t = 8.9 \text{ s}$ at the end of the combustion chamber in plane xy . Higher value are observed at injector surface, wherein the temperature is equal to 440 K .

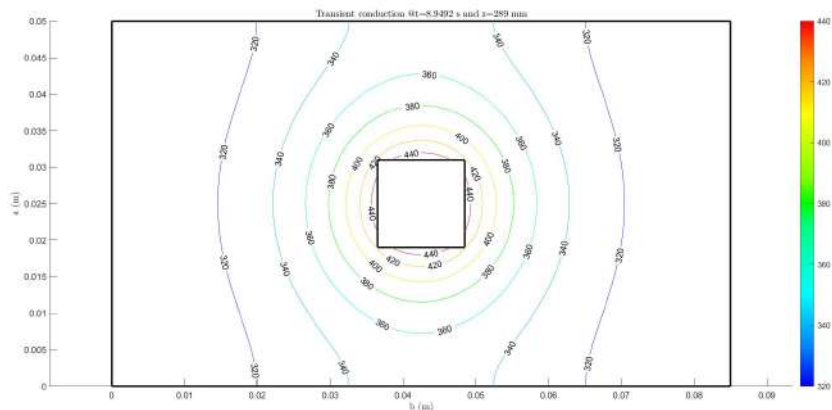


Figure 6.12: Temperature footprint at combustion chamber end section for $t = 8.9 \text{ s}$.

6.2.9 Combustion efficiency η_{c^*}

c_{th}^*	c_{calc}^*	η_{c^*}	$c_{th,AW}^*$	$c_{calc,AW}^*$	$\eta_{c^*,AW}$
[m/s]	[m/s]	[-]	[m/s]	[m/s]	[-]
1728.4	1401.6	0.81	1820.3	1396.8	0.76

Table 6.4: Combustion efficiency for test TMC-20-34-30-20-5.

The characteristic velocities both theoretical and calculated obtained with the assumption of adiabatic wall are named 'AW'. As explained in Section 4.2.2, the adiabatic values are lower than the values obtained after the correction carried out with the IHTM.

When comparing the combustion efficiency $\eta_{c^*,AW}$ obtained for LOX/CH4 with previous experimental works with GOX/CH4, significant lower results are obtained for the same nominal conditions. In fact the tests carried out with gaseous propellants led to a combustion efficiency which ranges from 0.9 to 0.97.

The phenomenon is studied more in depth, performing several tests at same nominal chamber pressure and same nominal OF ratio. The nominal point that is chosen is at chamber pressure $p_c = 20 \text{ bar}$ and OF ratio equal to 3.4 since presents lower VR. In fact, higher is the VR lower is the velocity of methane, hence better performance are expected as explained later in Section 6.5.2.

The low efficiency is thought to occur due to the low chamber pressure. In turns, the low combustion pressure may occur due to detached or fluttering flame. For this reason, a dynamic pressure sensor is placed within the combustion chamber to investigate the high frequency oscillations.

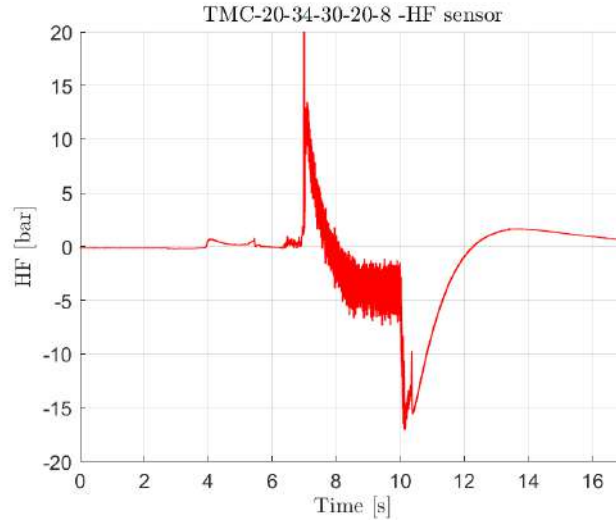


Figure 6.13: Signal registered by the dynamic pressure sensor for TMC-20-34-30-20-8 test.

After performing a Fourier transform, the dynamic pressure is readable from Figure 6.13. The dynamic pressure amplitude is approximately equal to 5 bar, which can indicate either an unstable combustion either a rough combustion. A smooth combustion with an anchored flame would show a pressure amplitude up to 1 bar.

To better understand how the methane velocity impacts on performance, a different ignition sequence is adopted. A first approach considers to shut off and on the methane main valve in order to slow down the flow. Further proposed solutions are exposed in detail in Appendix B.3.

The second approach is changing the igniter position, using spot the available along the first segment of the combustion chamber.

The third approach considers to add a cylinder between methane main valve and methane orifice.

6.3 Comparison among different OF ratios at same chamber pressure

6.3.1 Theoretical and experimental result

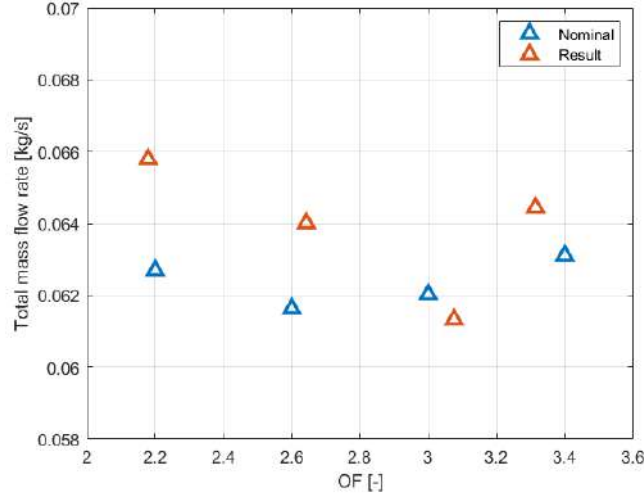


Figure 6.14: Nominal and obtained mass flow rate over OF ratio at same chamber pressure $p_c = 20$ and 20 % of film cooling.

Total mass flow rates are plotted in Figure 6.14 for the corresponding OF ratios from a sample of test performed at the same nominal chamber pressure equal to 20 bar and same percentage of film cooling equal to 20 %. The experimental results, both OF ratios values and total mass flow rates show a good agreement (up to 6 % of deviation from nominal value) with the predicted quantities. The discrepancy from theoretical values are higher for lower OF ratios, here 2.2 and 2.6.

6.3.2 Velocity Ratio

Having obtained the mass flow rate values, both liquid oxygen velocity and methane velocity are calculated from the experimental data. In experimental velocity calculation obtained by Eq. (6.2), propellants densities are calculated inputting pressure and temperature value at the injection conditions.

$$v_{LOX} = \frac{m_{LOX}}{\rho_{LOX} \cdot A_{th,LOX}} \quad (6.1)$$

$$v_{CH4} = \frac{m_{CH4}}{\rho_{CH4} \cdot A_{th,CH4}} \quad (6.2)$$

OF	2.2	2.6	3.0	3.4
Nominal VR	29.83	25.24	21.88	19.30
Obtained VR	25.5	23.2	22.75	21.23

Table 6.5: Nominal and obtained velocity ratios for a sample of test performed at different OF ratios but same nominal chamber pressure $p_c = 20$ bar.

The influence of the mixture ratio on the velocity ratio can be observed in Table 6.5. When considering the theoretical calculations, the higher is the selected OF ratio, the higher is the LOX velocity and the lower is the methane velocity. Since the methane velocity is one order of magnitude

higher than the LOX velocity, it plays the biggest role in VR value.

Hence higher is the OF, lower is the VR.

Furthermore, when comparing the maximum OF for different chamber pressure, the lowest VR corresponds to the highest pressure.

Since the velocity ratio VR is a measure of the difference in velocity between the propellants and shear forces, keeping a low value is believed to lead to a better behaviour of the flame, according to [29]. On the other hand, low VR could lead worst mixing accomplishment. Furthermore high chamber pressure could cause higher oscillations: higher chamber pressures lead to higher combustion temperatures which cause an increase in vibrational energy.

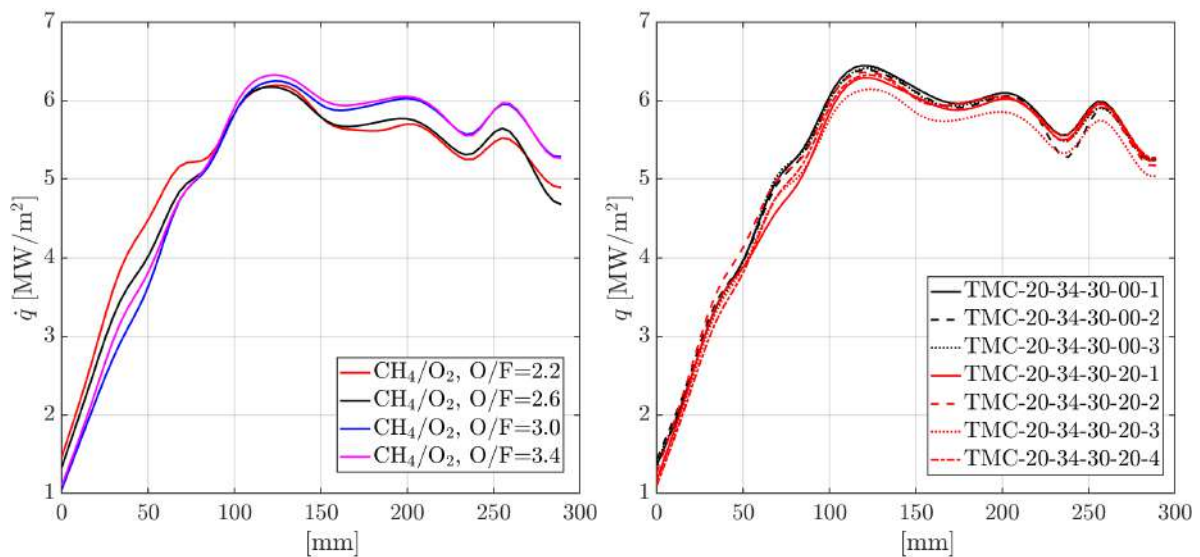
The theoretical behaviour is confirmed by experimental data: the higher VR is obtained for lower OF ratios. However the lowest OF ratios, here 2.2 and 2.6, present experimental VR values lower than the theoretical one. This behaviour is not merely observed for the sample of tests reported in Table 6.5, but also for all the test performed.

6.3.3 Heat flux comparison

Figure 6.15a shows the heat flux profile along chamber axial length for different OF ratios. One may notice that the lower the OF, the higher is the heat flux before combustion occurs at position $z = 130 \text{ mm}$. In fact along the first 130 mm, the mixture kinetics plays the main role in mixing process. As seen in Table 6.5 at lower OF ratios correspond to predominant shear forces. For 2.2 case the velocity ratio VR is the highest, hence the highest heat flux value of is reached.

After that the chemical reaction is completed at location $z = 130 \text{ mm}$, a trend reversal is registered. The OF ratio similar to the stoichiometric value, here 3.4 which approaches 4, produces the highest heat flux since larger combustion temperature and energy release are reached.

Observing the heat flux profile in Figure 6.15b for different film cooling percentages, in general higher heat flux values are registered for lower film cooling percentage.



(a) Heat flux profile over length for different OF ratios. (b) Heat flux profile over length for different film cooling percentage.

Figure 6.15: Heat flux over chamber length for different OF ratios and for different cooling percentages.

6.4 Hot Fire Test Campaign LOX/GH2 with copper window

The following Hot Fire test THC-20-68-30-20-1 is performed for the nominal point presented in Table 6.6. THC label indicates *Test* with *Hydrogen* as fuel and with *Copper* window.

The first number 20 refers to the nominal chamber pressure, the second number 68 to selected OF ratio, the third number 30 to the burning time, the fourth number 20 to percentage of film cooling mass flow rate and the last number 1 is the number of the repetition of the test at the same conditions.

p_c	OF	t	$\%_F$	n°
[bar]	[-]	[s]	[-]	[-]
20	6.8	3.0	20	1

Table 6.6: Nominal load point for THC-20-68-30-20-1 test.

6.4.1 Pressure setting

Film cooling, oxidizer and fuel mass flow rates for main line are calculated, as well as the mass flow rate for the igniter. Hence the tank pressures relative to the ambient for hydrogen, oxygen and nitrogen are calculated e manually set at the pressure regulators.

The curve in Figure 5.2 obtained from Cold Flow campaign is used to manually set oxygen tank pressure.

The pressure regulators, valves and upstream sensor maintain the same name as Table 6.2.

		UNITS	VALUE
LOX mass flow rate	\dot{m}_{LOX}	[g/s]	44.89
Relative OX tank pressure	$p_{tank,r}$	[bar]	3
Ambient pressure	p_{amb}	[bar]	0.96
Absolute OX tank pressure	$p_{tank,a}$	[bar]	21.5
H2 mass flow rate	\dot{m}_f	[g/s]	6.6
Relative H2 tank pressure	$p_{f,r}$	[bar]	68.36
GN2 film cooling mass flow rate	\dot{m}_F	[g/s]	1.32
Relative GN2 tank pressure	$p_{F,r}$	[bar]	18.14
Relative OX pressure for igniter	$p_{ZO,r}$	[bar]	17.23
Relative H2 pressure for igniter	$p_{ZM,r}$	[bar]	36.82

Table 6.7: Nominal mass flow and pressure values for THC-20-68-30-20-1 test.

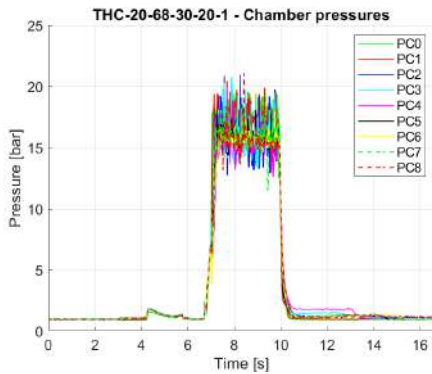
Since the injector element is not designed for LOX/H2 combustion as mentioned in 2.6, a rough combustion is expected. A different geometry would suit the LOX/H2 combustion, with a higher injection area for oxygen.

For higher OF ratios and higher chamber pressure a better behaviour is expected since the velocity ratio is lower.

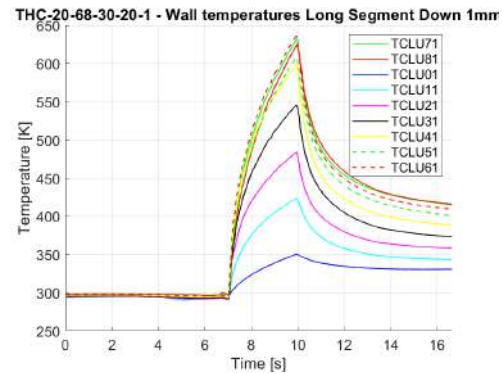
6.4.2 Chamber temperature and pressure distribution

From the pressure profile in Figure 6.16a, a high level of noise in pressure sensors is detectable, as expected. Despite the pressure set at the oxidizer pressure regulator is equal to 21.5 bar as shown in Table 6.7, the obtained chamber pressure has an average value of 16 bar approximately. As previously seen for CH₄ campaign, the pressure value reached inside the combustion chamber has a significant impact on combustion performance.

When comparing temperature profile in Figure 6.16b for LOX/H₂ test with LOX/GCH₄ temperature profile in Figure 6.4d, higher combustion temperature are reached with H₂ combustion. For LOX/GCH₄ case the temperature peak is approximately equal to 490 K, while H₂ combustion allows a maximum temperature of 640 K.



(a) Pressure profile within combustion chamber.



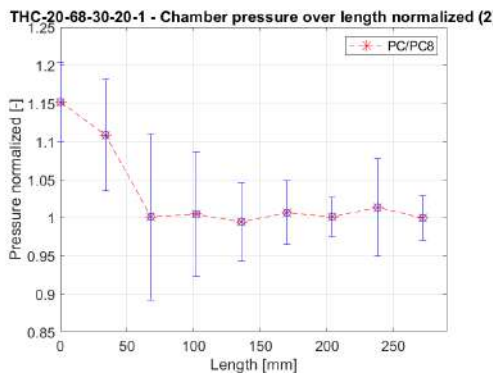
(b) Pressure profile within combustion chamber.

Figure 6.16: Combustion chamber measurements versus running time.

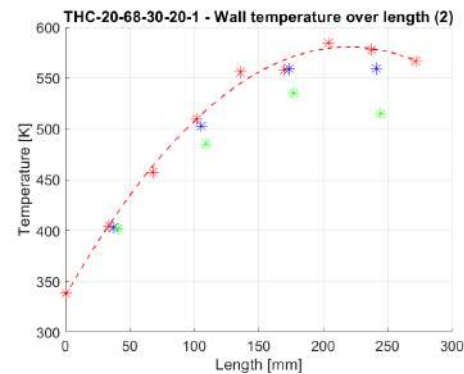
6.4.3 Chamber temperature and pressure distribution over length

The values of the pressure sensors are averaged over the evaluation window, centered in the evaluation time equal to $t = 8.9\text{ s}$ for the present test. Chamber pressure measurements normalized with the last sensor PC8 value show a decrease of 15%, the double if compared with CH₄ case.

When comparing the profile temperature along z -axis in Figure 6.17b with the same plot for CH₄ in Figure 6.5b one may notice that that H₂ temperature curve presents a maximum for a position further upstream, equal to $z = 225\text{ mm}$. After that the maximum of temperature has been reached, the temperature starts to decrease before the nozzle section, indicating that the combustion process is ended.



(a) Chamber pressure measurements along chamber length normalized with the last pressure sensor PC8.



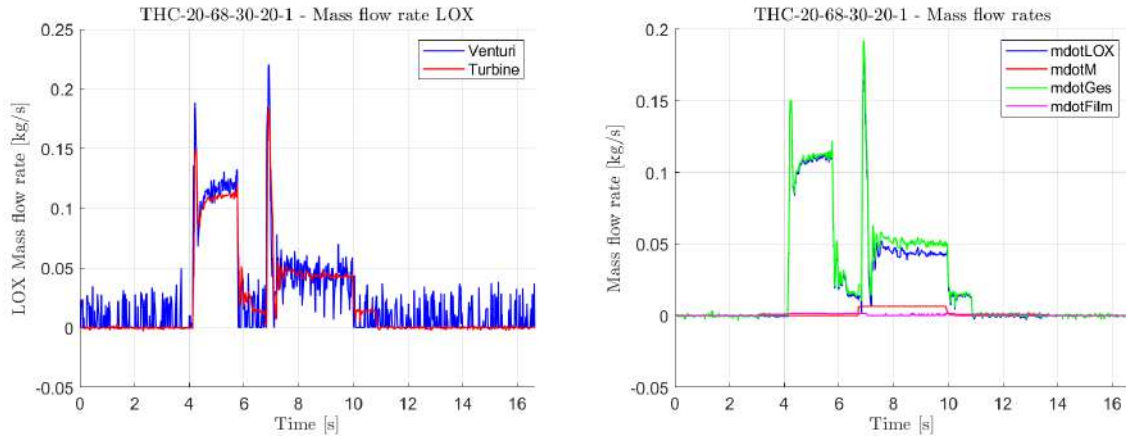
(b) Chamber temperature measurements along chamber length fitted for 1mm from the hot side wall measurements.

Figure 6.17: Normalized pressure and temperature profile along chamber axis.

6.4.4 Mass flow rate distribution

Mass flow rate distribution is obtained both with Venturi calculation and turbine measurement. The two spikes in Figure 6.18a occur when the LOX main valve is opened, once for the precooling phase and once for the ignition. During the burning time from $t = 7\text{ s}$ to $t = 10\text{ s}$ oxygen mass flow rate is fairly constant.

In Figure 6.18b one may appreciate the large difference between hydrogen mass flow rate represented in red and liquid oxygen mass flow rate represented in blue. In fact between the two quantities there is one order of magnitude. Film cooling mass flow rate is depicted in pink with a mean mass flow rate equal to 4 g/s



(a) Liquid oxygen mass flow rate.

(b) Liquid oxygen, methane, total and film mass flow rate.

Figure 6.18: Mass flow rates.

6.4.5 Oxidizer to fuel ratio

During burning time, the obtained OF in Figure 6.19 is 4.5% lower than the nominal value equal to 6.8.

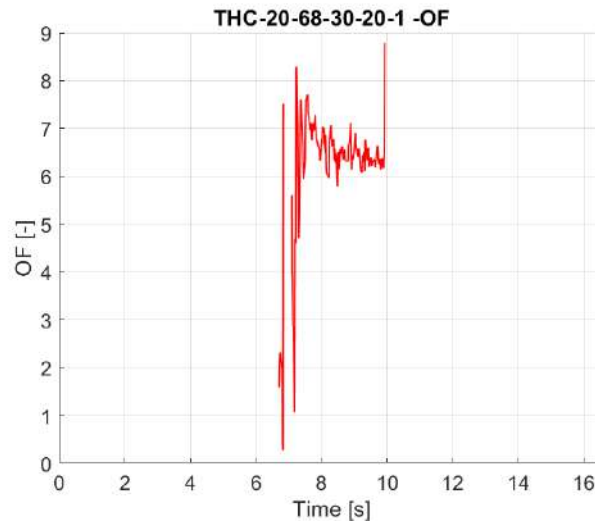


Figure 6.19: Oxidizer to fuel ratio during burning time.

From Table 6.8 a good agreement between calculated and experimental data is obtained for mass flow rates and OF ratio. The higher deviation is once again registered for the fuel velocity, which impacts on the momentum flux ratio J and on the velocity ratio VR . All experimental values are higher than the calculations, except the oxygen mass flow rate which present a slight lower value than the expected one.

	IDEAL	EXPERIMENTAL	UNITS	DEVIATION
\dot{m}_{LOX}	44.89	44.00	[g/s]	2 %
\dot{m}_{CH4}	6.60	6.8	[g/s]	3 %
v_{LOX}	5.54	5.63	[m/s]	1.6 %
v_{CH4}	425.43	530.78	[m/s]	24.7 %
VR	76.79	94.13	[-]	22.6 %
J	9.12	15.43	[-]	69 %
OF	6.8	6.49	[-]	4.5 %

Table 6.8: Ideal and obtained quantities for THC-20-68-30-20-1 test at the evaluation time.

6.4.6 Injector pressure drop

The pressure drop across the injector is presented in Figure 6.20 since it has an impact on flame anchoring and flame behaviour. The difference between PM3 and PM4 pressure, here blue and red plots, during burning time represents the pressure drop across the fuel orifice, quantifiable in approximately 2.5 bar. The difference between PM4 and PC0 sensors represents the pressure drop across the injector, since PC0 is the first sensor placed inside the combustion chamber. The difference between red and green plots is about 5 bar, which is the double if compared with CH4 injector pressure drop in Figure 6.7a. Furthermore, a delay in reaching the maximum value is observed from PC0 pressure sensor, which does not follow the raise at time $t = 6.8$ s as PM3 and PM4. This fact could be explained by the delay that PM3 and PM4 present in reaching the maximum value after a small step at the same time after the ignition.

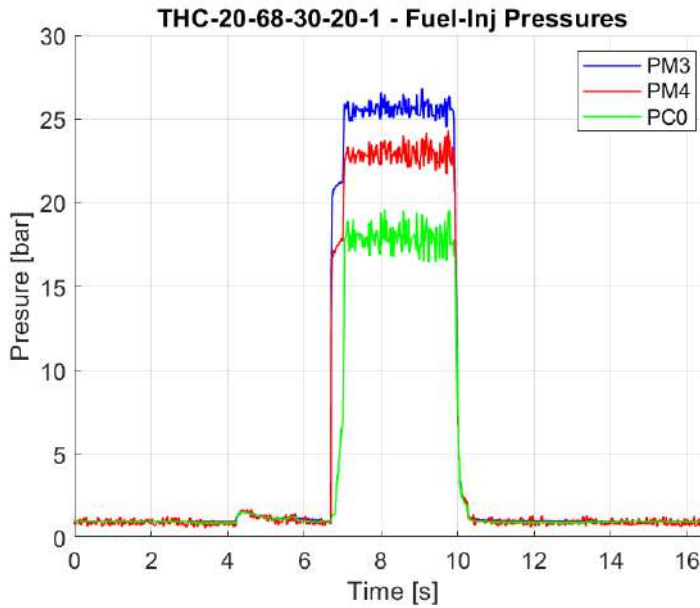
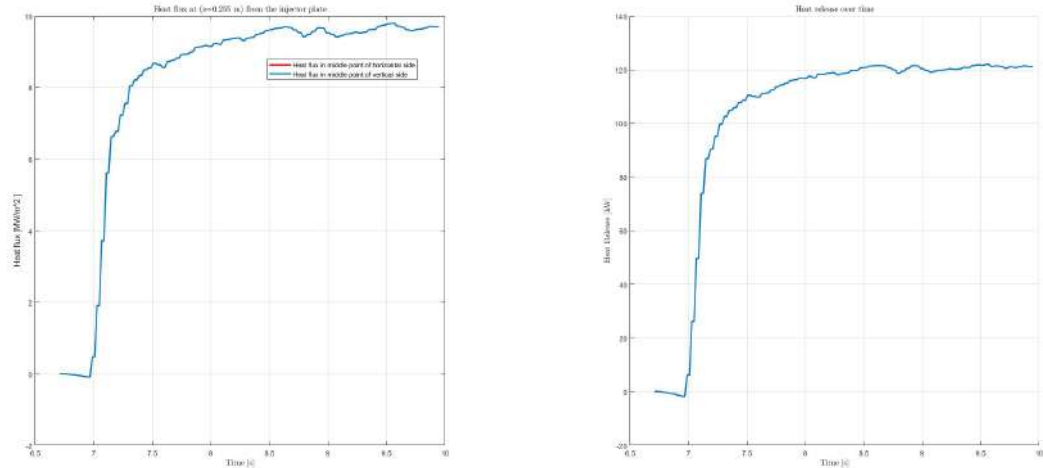


Figure 6.20: Hydrogen pressure drop across the orifice and across the injector.

6.4.7 Heat flux distribution

When comparing heat release in Figure 6.21a and Figure 6.10a, higher values are reached for H₂ combustion. For the position $z = 255 \text{ mm}$ from the injector plate the heat flux value is equal to 9.5 MW/m^2 during burning time. However, having analysed the temperature profile along chamber length in Figure 6.17b led to the conclusion that the combustion process ends further upstream the position at $z = 255 \text{ mm}$. As seen for the CH₄ case, the heat flux undergoes some fluctuations along chamber length: hence the heat flux plotted over length in Figure 6.21 would add more information. In Figure 6.21b the average heat flux is integrated over wall surface obtaining the heat release over time, which presents a maximum value equal to 120 kW . This value is fairly constant from time $t = 8.9 \text{ s}$ on, when the chemical reaction occurs.

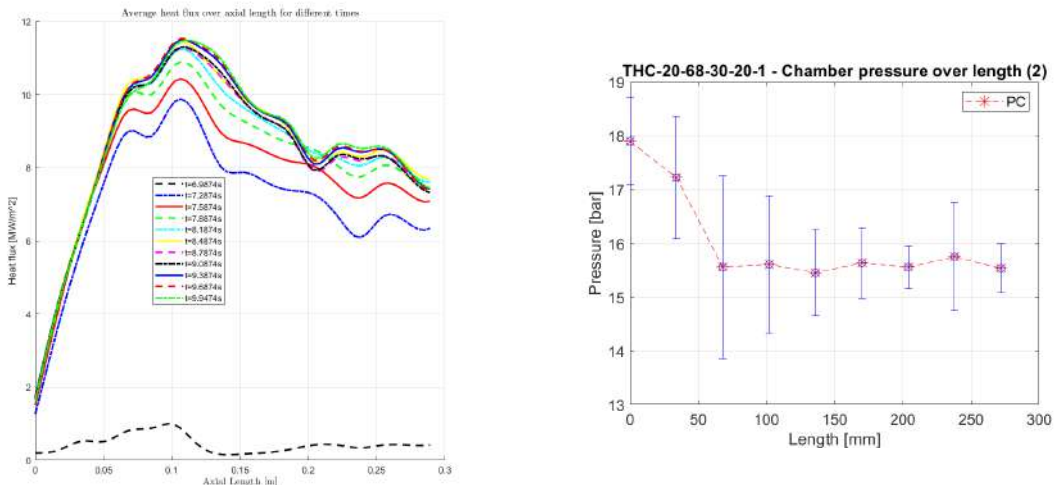


(a) Heat flux distribution at position $z=0.255$ from the injector plate.

(b) Heat release over time.

Figure 6.21: Heat flux and heat release profile over time.

In Figure 6.22a heat flux over length is plotted for different instants of time. The maximum equal to 11.5 MW/m^2 is reached for the axial position $z = 110 \text{ mm}$ for the time $t = 8.78 \text{ s}$.



(a) Heat flux profile over length for different times averaged for horizontal positions.

(b) Pressure distribution over chamber length.

Figure 6.22: Heat flux profile over length for different film cooling percentage.

In Figure 6.23 heat flux is plotted over chamber length for both LOX/CH₄ and LOX/H₂ cases. For LOX/H₂ combustion higher values are reached and for a backward position, meaning that a faster combustion is achieved using hydrogen as fuel. Higher heat flux values are expected since the LOX/H₂ combination is known to reach higher combustion temperature.

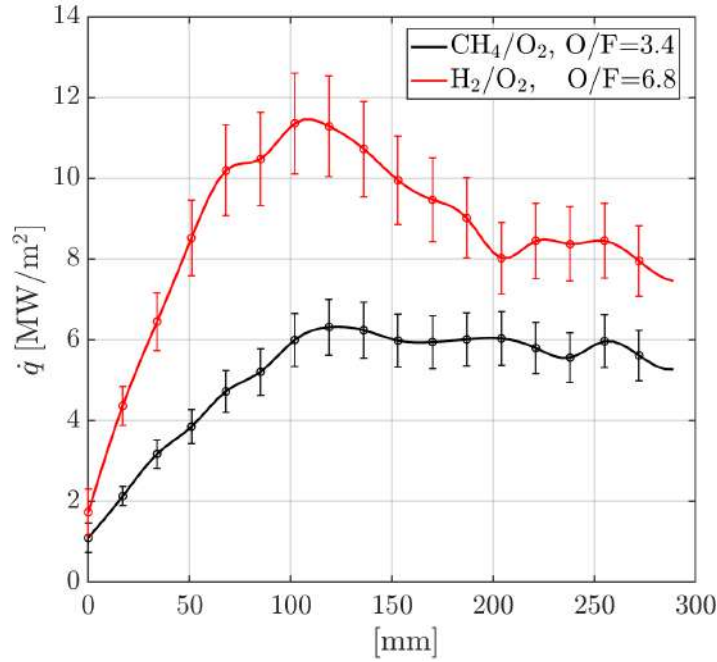


Figure 6.23: Heat flux over chamber length comparison between H₂ and CH₄.

6.4.8 Combustion efficiency η_{c^*}

c_{th}^*	c_{calc}^*	η_{c^*}	$c_{th,AW}^*$	$c_{calc,AW}^*$	$\eta_{c^*,AW}$
[m/s]	[m/s]	[-]	[m/s]	[m/s]	[-]
2117.9	1762.7	0.83	2261.0	1762.9	0.78

Table 6.9: Combustion efficiency for test THC-20-68-30-20-1.

Since the injector element is not specifically designed for LOX/H₂ combustion as mentioned in 2.6, a rough combustion is expected. A different geometry would suit the LOX/H₂ combustion, with a higher injection area for hydrogen. Since the cross sectional area is lower than the optimum one, the fuel velocity is higher, hence the velocity ratio VR defined as in Eq. (2.25) is higher. As the velocity ratio plays the main role in the shear forces between fuel and oxidizer, the flame behaviour is strongly influenced by the obtained value. The role of velocity ratio becomes even more important for lowest OF ratios.

The theoretical characteristic velocity obtained with IHTM is higher if compared with the adiabatic one. Since the characteristic velocity calculated with the experimental data has the same value, the resulting combustion efficiency with IHTM correction is higher.

Comparing combustion efficiency for CH₄ case and H₂ case is qualitatively possible since the tests presented are run at the same nominal chamber pressure and at the maximum OF ratio. Despite higher temperatures are reached with H₂ combustion, the obtained efficiency is lower due to the high noise and the rough combustion which cause the high pressure decay.

6.5 Comparison among different OF ratios at same chamber pressure

6.5.1 Theoretical and experimental result

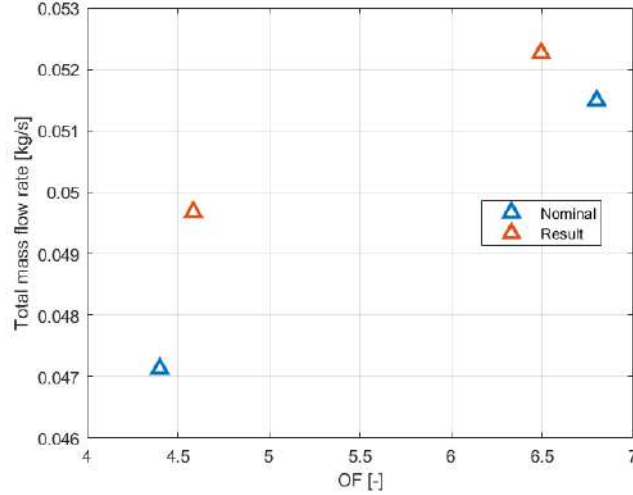


Figure 6.24: Nominal and obtained mass flow rate over OF ratio at same chamber pressure $p_c = 20$ and 20 % of film cooling.

The values reported in Figure 6.24 correspond to the lowest and the highest oF ratio, here 4.4 and 6.8. The total mass flow rate obtained from the tests shows a higher deviation from the calculated one for the lowest OF ratio value. Indeed for the tests performed at OF ratio equal to 4.4 a large noise occurred within the combustion chamber.

6.5.2 Velocity Ratio

Propellants velocities are calculated once again by Eq. (6.2): propellants densities are calculated inputting pressure and temperature value at the injection conditions.

$$v_{LOX} = \frac{m_{\dot{L}OX}}{\rho_{LOX} \cdot A_{th,LOX}} \quad (6.3)$$

$$v_{H2} = \frac{m_{\dot{C}H4}}{\rho_{CH4} \cdot A_{th,H2}} \quad (6.4)$$

OF	4.4	6.8
Nominal VR	118.68	76.79
Obtained VR	111.9	94.13

Table 6.10: Nominal and obtained velocity ratios for a sample of test performed at different OF ratios but same nominal chamber pressure $p_c = 20$ bar.

The results obtained in Table 6.10 have the same trend of CH results. The obtained VR decreases with increases OF ratio, but for the lowest OF ratio the experimental value is lower than the predicted one. Note that VR is the ratio between liquid oxygen velocity and hydrogen velocity: both experimental velocity of oxygen and hydrogen are higher than the theoretical quantities, for both the considered OF ratios. Thus the resulting experimental VR at 4.4 is lower merely because liquid oxygen velocity is higher than the expected one.

6.5.3 Heat flux comparison

The average heat flux is plotted over z-axis in Figure 6.25 for the lowest and highest OF considered for LOX/H₂ combustion.

The same behaviour of the heat flux over time for different OF ratio is observed, if compared with CH₄ case. Before the mixture starts to react, the higher heat flux value is presented by the 4.4 case, since the velocity of hydrogen is higher and enhances the mixing process thanks to higher shear forces. When combustion occurs, the heat flux has a maximum for the 6.8, here the OF ratio which approaches the stoichiometric value equal to 8.

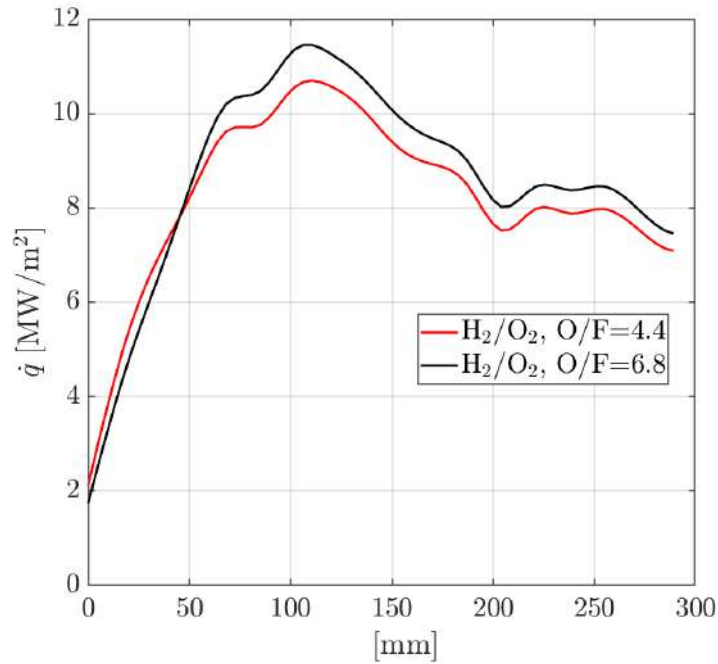


Figure 6.25: Heat flux profile over length for different OF ratios.

6.6 Hot Fire Test Campaign LOX/CH₄ with glass window and Panasonic camera

The following Hot Fire test TMW-20-34-25-20-7 is performed with the quartz-glass window and with the Panasonic camera. TMW label indicates *Test* with *Methane* as fuel and with *Window*. One may note that the burning time is reduced to 2.5 seconds to prevent window breaking.

This section is dedicating to the optical visualization of the flame, hence no further analysis are carried out to investigate the pressure and temperature distribution, the mass flow rates and the heat flux profile.

p_c	OF	t	$\%_F$	n°
[bar]	[-]	[-]	[s]	[-]
20	3.4	2.5	20	7

Table 6.11: Nominal load point for TMW-20-34-30-20-7 test with glass window.

Since the nominal point is the same as fro the Hot Fire test with copper window presented in Table 6.1, the pressure settings in Table 6.2 are valid for the present test. The obtained results are shown in Table 6.12.

	UNITS	VALUE
\dot{m}_{LOX}	[g/s]	51.6
\dot{m}_{CH_4}	[g/s]	14.4
\dot{m}_{FILM}	[g/s]	28.9
OF	[-]	3.58
PTANK	[bar]	21.27
PM2	[bar]	57.32
PC0	[bar]	17.97
TLOXVEN2	[K]	83.88
TO3	[K]	105.78
Q	[kW]	75
η_{c^*}	[-]	0.79

Table 6.12: Obtained mass flow, pressure and temperature values for TMW-20-34-25-20-7 test.

In Figure 6.26 the jet flame is shown in several frames to cover the testing time. The precooling phase with liquid oxygen is visible in the first frame. Oxygen jet expands radially. In the second frame the reaction instant of time is captured: the emitted light has a high intensity that make flame shape difficult to distinguish.

In the third frame flame shape is clearly visible. The flame presents a straight path until approximately one diameter from the injector plane. A this location the inflection point can be located. Then a spreading angle is visible. Afterwards, the flame develops fairly symmetrical and straight along z-axis. The fourth and fifth frames present a proceeding of the bluish region which highlights the extinction of the flame.

The last frame shows a weak brightness when the last chemical reactions occur. The spreading angle is reduced and the flame presents a divergent profile along chamber main axis.

When considering GOX/CH₄ flame from previous experimental campaign, a divergent shape of the flame similar to last frame is register for the entire burning time. The change in concavity is typical of LOX flame.

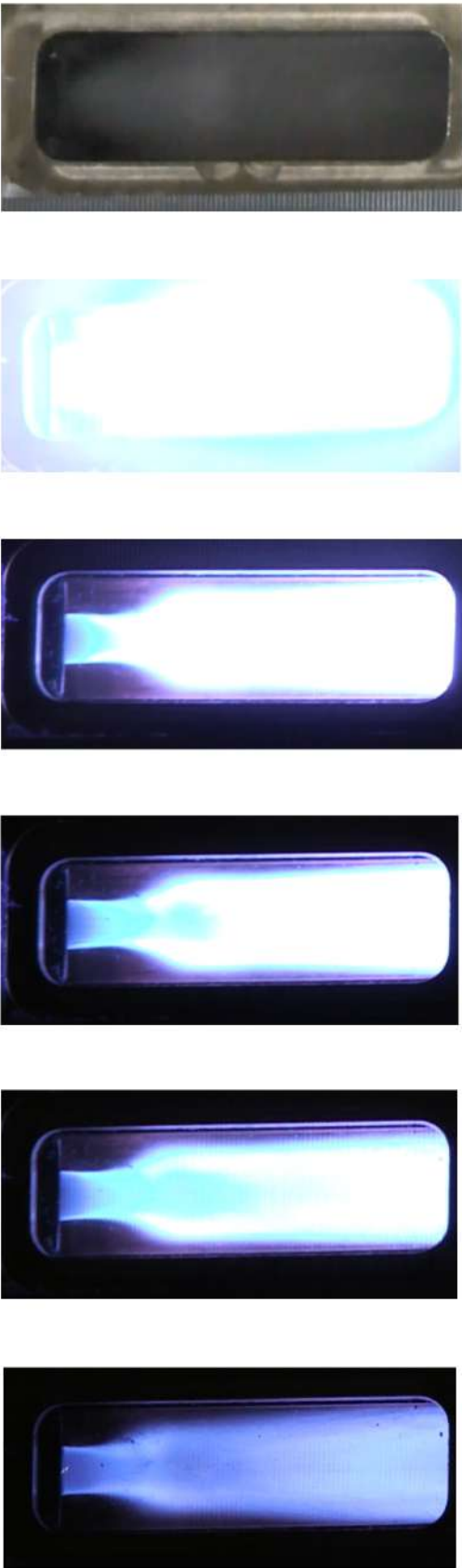


Figure 6.26: Flame top view from glass window with Panasonic camera.

6.7 Hot Fire Test Campaign LOX/CH₄ with glass window and FlameStar2 camera

6.7.1 Chemiluminescence Technique

The following Hot Fire test TMW-20-34-25-20-10 is performed with the quartz-glass window and with the Flame Star2 camera. TMW label indicates *Test* with *Methane* as fuel and with *Window*.

In Figure 6.27 the raw images captured by Flame Star 2 camera are presented. Raw images are converted from 24 bit format to 8 bit format in order to obtain the colormap relative to the images.

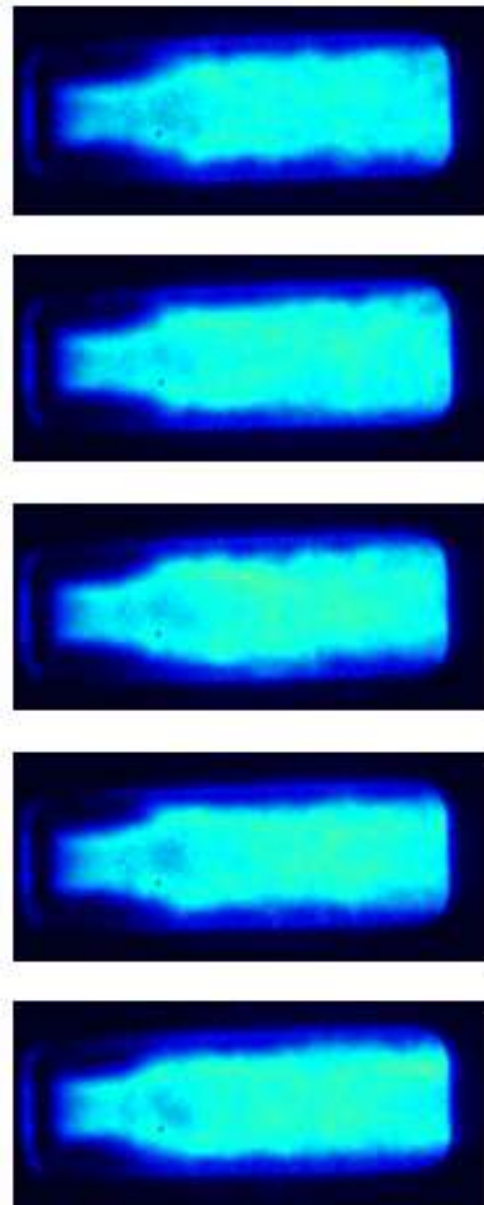


Figure 6.27: Raw images of flame emission captured by Flame Star 2 camera and OH* filter.

Raw images are hence rotated at an angle of -1° and resized of $[z=70:360, x=332:436]$ pixels as in Figure 6.28 using the *Image Importing* function in AVERAGED IMAGES ROUTINE. Once that the images have been indexed, i.e. a level of brightness has been allocated, the index is scaled with a gray scale and a gray map is applied.

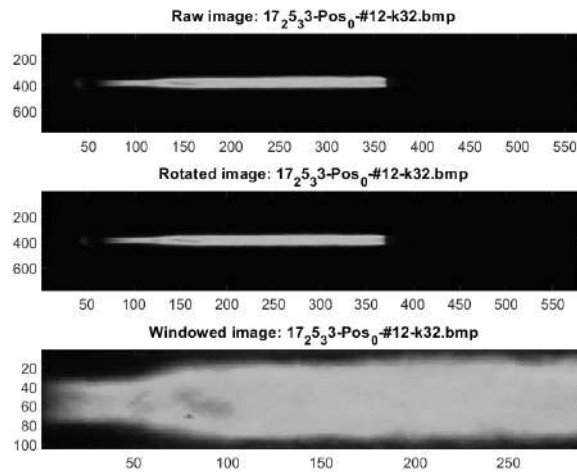
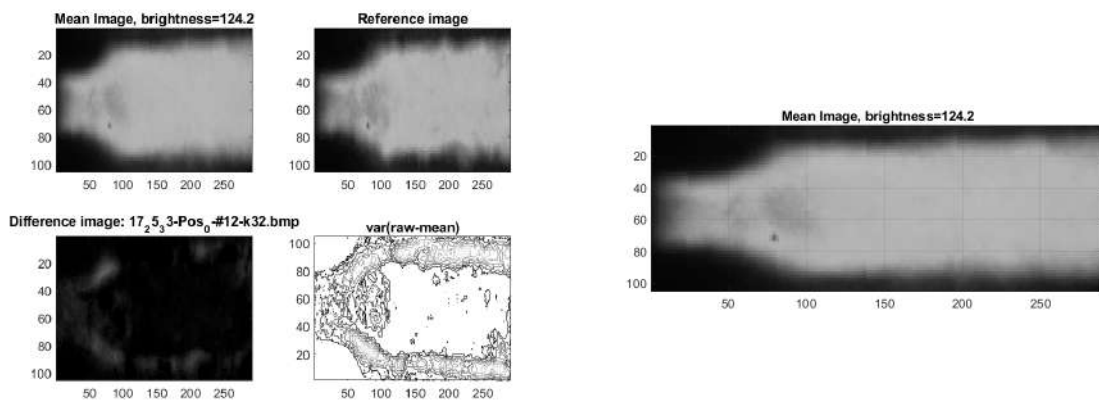


Figure 6.28: Raw image - Rotated image - Resized image.

The first image is selected as the reference image. Hence the mean image in term of brightness is calculated and shown in Figure 6.29b. In Figure 6.29a the difference (mean-reference) and the counted variance (raw-mean) are depicted. Note that images axes refer to the number of pixels. When comparing the mean image with the reference image, a lower level of brightness is observed for the reference image as well as more jagged edges. Since the reference image corresponds to the first image, the brightness is lower due to the fact that the full combustion is not been reached yet. The mean image results also more homogeneous. A small black dot is visible, that is a crack full of soot not allowing the passage of light.

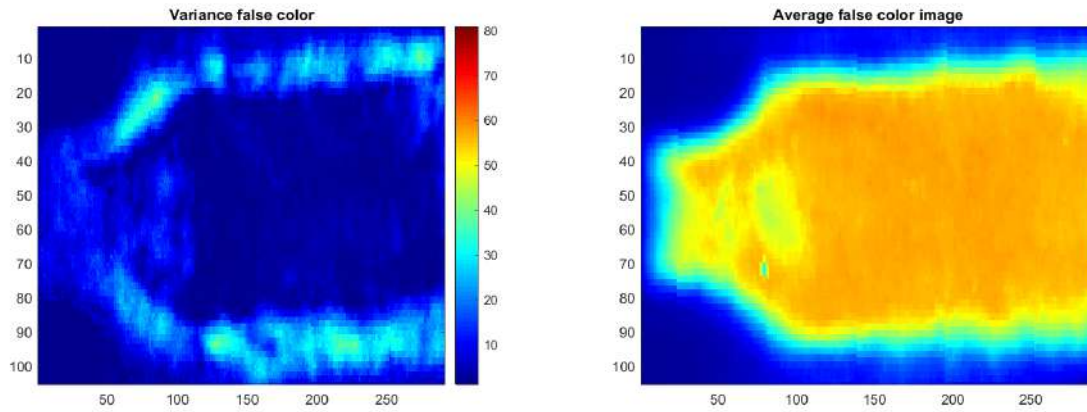


(a) Average image - Reference Image - Difference image - Variance image.

(b) Average image.

Figure 6.29: Images obtained with *Image Processing* function AVERAGED IMAGES ROUTINE.

In Figure 6.30a the variance is highlighted with jet colormap. In this picture a measure of the difference among the raw image and the mean image which is higher for the bottom half of the image. In Figure 6.30b is possible to distinguish the different regions of the flame. The green circular region indicates a portion of flame where lights is not emitted due to soot formation on glass surface or either the LOX core OH^{*}-free.



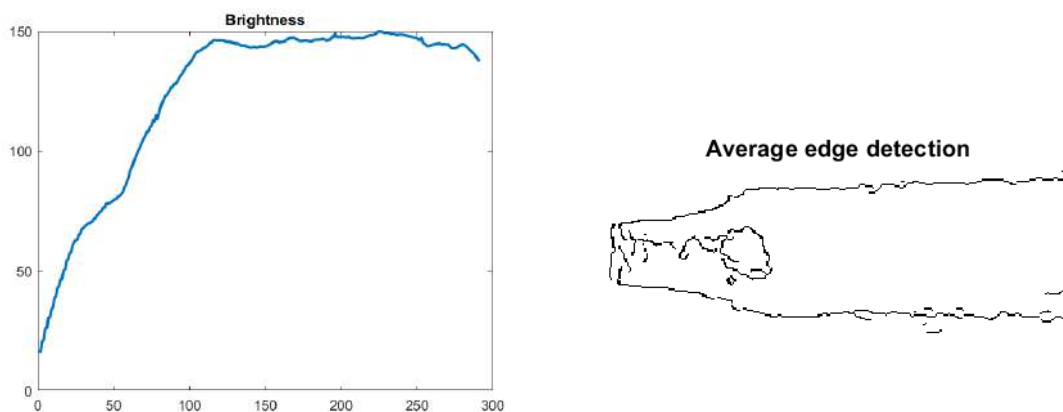
(a) Variance image with colormap.

(b) Average image with colormap.

Figure 6.30: Images obtained with *Chemiluminesce* function in AVERAGED IMAGES ROUTINE.

In Figure 6.31a the average image is considered: the mean brightness is calculated for each column of the image, that is the mean among different radial position x . Hence is plotted for different axial positions along z axis.

Figure 6.31b shows the edges of the flame and of the central bluish region. No further edges are visible since the resizing is made excluding just graphite foils edges.



(a) Average Brightness along chamber length.

(b) Flame edges detection.

Figure 6.31: Images obtained with *Chemiluminesce* function in AVERAGED IMAGES ROUTINE.

The brightness is plotted for different axial positions from the injector plane in Figure 6.32. The brightness considered is referred to the average image. The axial positions are equally spaced of 20 pixels, corresponding to 4 mm along z axis. For the first axial position equal to $z = 2 \text{ mm}$ from the injector the lowest value in brightness is observed. The radial brightness presents a non-linear distribution with increasing axial position, as can be also seen from Figure 6.31a. The plot presents an overall symmetry. Focusing on on axial position, initially the brightness raises since at the top edge of the flame the gaseous methane react with the oxygen. Proceeding towards the center of the jet, a lower brightness is register since less OH* emission is present whereas the oxygen core is located. To get a better visualization of the inner flame, an Abel inverse transform is needed.

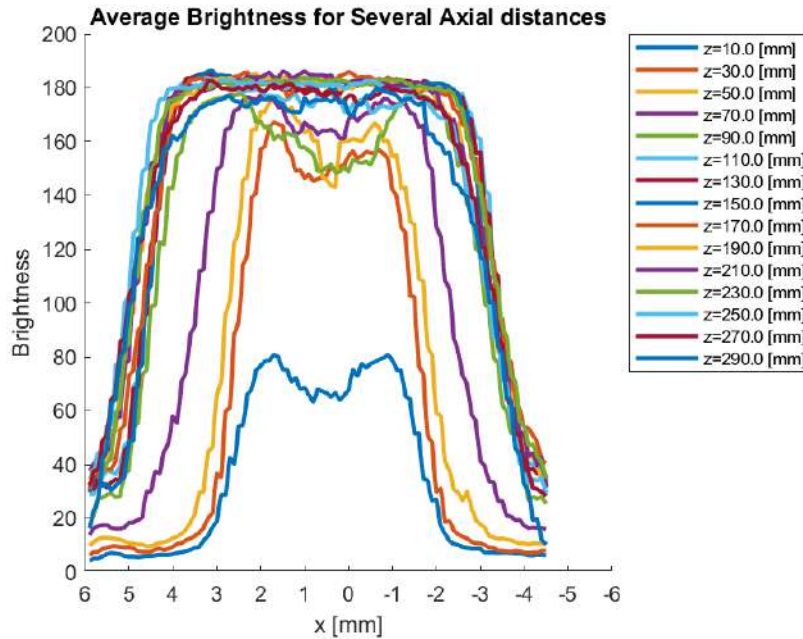


Figure 6.32: Mean brightness for several axial positions.

6.7.2 Abel Inverse Transform

In Figure 6.33 the measured emitted intensity is plotted for the bottom half and for the top half of the image. Since the Abel inverse transform is not been applied yet, the 3D plot shows the "external" brightness of the flame. Starting from position $z = 0 \text{ mm}$, the level of brightness raises and remains constant with the exception of a central circular zone of lower brightness due to soot formation. Comparing bottom and top emission, the bottom half seems to have a less steeper gradient and a less homogeneous path, probably due to the fact that the igniter is placed on top half side. Hence the average is calculated and shown is Figure 6.33c.

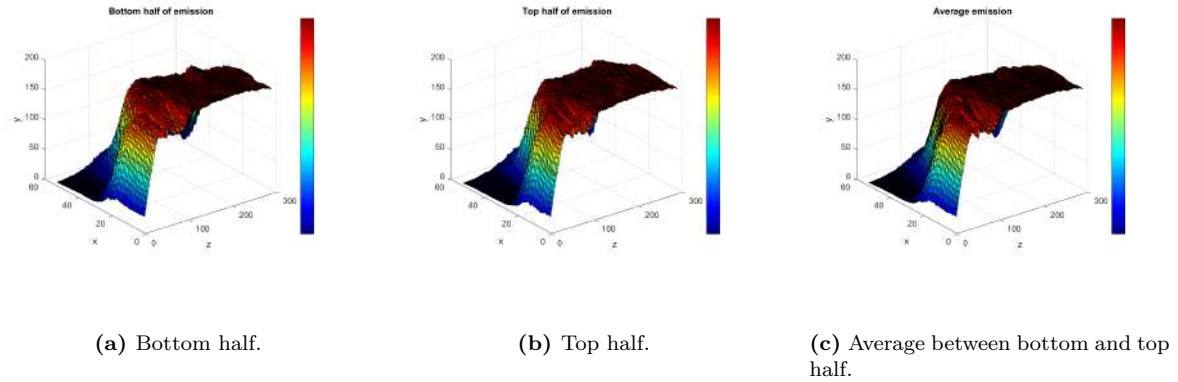


Figure 6.33: Visualization of the measured OH^* emission.

The Abel inverse transform is carried out as described in Section 4.4.4 and 4.4.5. In Figure 6.34 the Abel inverse transform has been carried out, leading to a 3D projection of the flame brightness. As expected, the brightness is higher at the corners where the OH^* emission is more significant due to the combustion process occurring in the external region. In the central region OH^* emission decreases. A peak in brightness is observed neat the injector plane and needs further investigations. Abel inverse transform is carried out for the two halves of the image separately, hence the average between the two halves is calculated and shown in Figure 6.34c. The average is carried out due to the fact that the Abel inversion is high sensitive to the asymmetry.

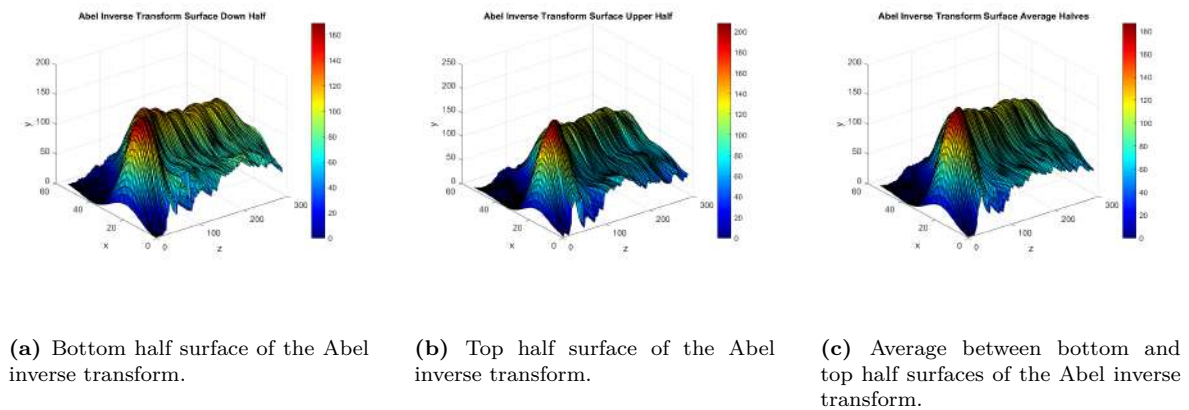


Figure 6.34: 3D visualization of the Abel inverse transform.

The 2D Abel inverse transform represents the projection on a plane of the inner flame. In Figure 6.35 is the resulting image from the average between upper and down halves. The projection reveals a higher brightness at the external annulus of the flame. Proceeding forward the axial length the external region is less brighter since the main reactions involving OH^* production occur until approximately 6 diameter from the injection plane. The internal region appears poor of OH^* emission, since the oxygen core does not take part in the reaction. The peak of OH^* in the near injection zone up until 2 diameters, was not expected if GOX/GCH4 results are taken as reference.

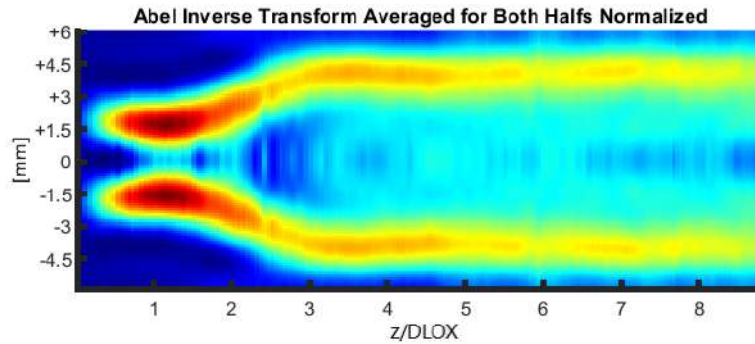
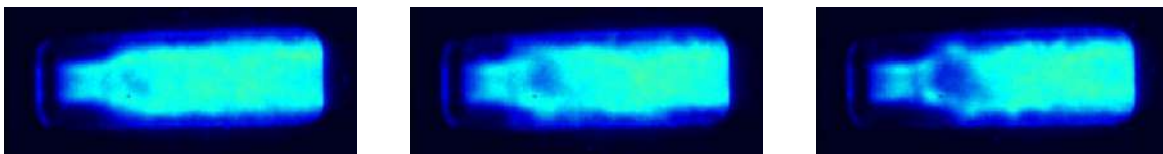


Figure 6.35: 2D Abel inverse transform.

6.7.3 OF comparison

Comparing different OF ratios, a larger bluish region, that is a larger liquid oxygen core, is detectable in the near injection region for higher OF ratio. In this case oxygen mass flow rate is higher, however the main role is played by the velocity and the momentum flux ratios. The higher is the OF the lower is the velocity ratio VR and the momentum flux ratio J . Hence at higher OF ratio the liquid oxygen core is less constricted by the slower methane. In Figure 6.36, despite the nominal OF ratio is 3.4 for both tests, the obtained value is 3.0 for the picture on the left and 3.4 for the picture on the right. On the other hand, with proceeding in experiments soot formation absorbs the light causing the central darker region.



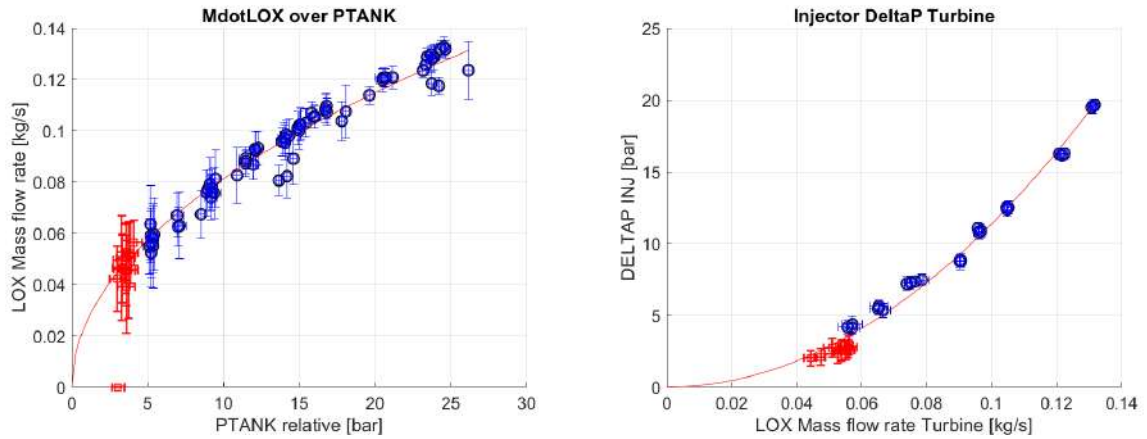
(a) OF=3.0

(b) OF=3.3.

(c) OF=3.6.

Figure 6.36: Flame OH^* emission for different obtained OF ratios.

6.8 Hot Fire results over Cold Flow curve



(a) LOX mass flow rate over oxygen tank relative pressure (b) Injector pressure drop over LOX mass flow rate measured with turbine for Cold Flow and Hot Fire results.

Figure 6.37: Heat flux profile over length for different film cooling percentage.

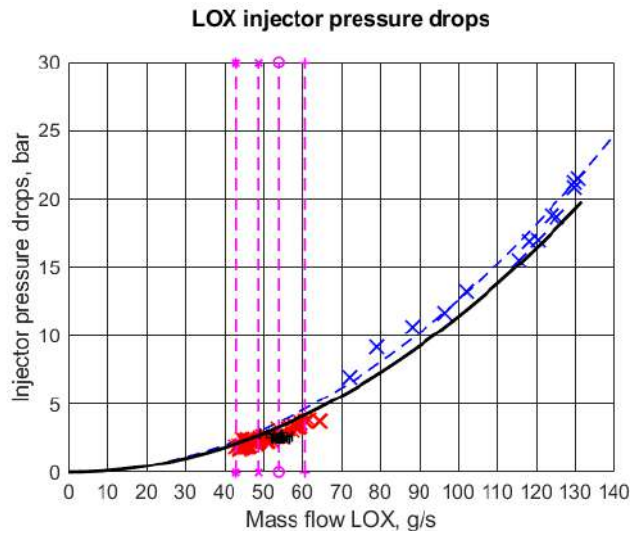


Figure 6.38: Injector pressure drop over LOX mass flow rate -Cold flow and Hot Fire - Comparison with previous tests performed by Christoph von Sethe.

In Figure 6.38 the black curve indicates the Cold Flow fitted curved obtained from tests performed for this thesis aim. Hot Fire results are plotted in black crosses which represent the pressure drop across the injector section over the LOX mass flow rate. The curve is compared with the blue curve obtained from previous testes performed with a multi-injectors round combustion chamber operating with liquid oxygen and gaseous methane. The comparison show a good agreement, especially for low pressure drops up to 5 bar, where the Hot Fire test are confined.

Chapter 7

Conclusions

This work of thesis aims to enrich the knowledge in oxygen and methane combustion, having considered the raising trend of Green Propellants. From the previous works with gaseous oxygen at the Lehrstuhl für Turbomaschinen und Flugantriebe of the Technische Universität München valuable information and data have been used to upgrade the facility implementing liquid oxygen usage.

From Cold Floe tests campaign a not negligible pressure drop has been observed across the injector. Furthermore the high uncertainty of the Venturi mass flow rate first made a geometry optimization necessary and subsequently a volumetric turbine positioning.

During the Hot Fire test campaign with methane as fuel and copper window, a lower combustion efficiency than expected was observed. The reason was attributed to the roughness of the combustion due to unstable or detached flame within the combustion chamber.

When comparing hydrogen and methane tests campaign, higher temperatures and hence higher heat flux profile have been observed for hydrogen case. However the pressure profile during time showed a high level of noise for both campaigns. Having placed a dynamic pressure sensor highlighted the roughness of the combustion process.

From recorded videos a greenish plume is observed especially in case of hydrogen combustion, revealing copper reaction with combustion products during burning phase. Copper may participate to combustion if the boundary layer has been consumed by the pressure and heat peaks as described in Section 2.8. For future work, an injector element designed for hydrogen should be taken into consideration.

From Hot Fire test campaign with glass window, either an oscillation in the flame or a lifted flame was hence expected.

The Panasonic camera did not reveal a combustion instability. However the combustion instability may have occurred at high frequency: a high speed camera would have been necessary. However, it has been demonstrated that for higher velocity ratios the roughness of the combustion decreases. The roughness of combustion is still an open topic to be analyze with more sophisticated equipment. Furthermore, a PDI, here a Phase Doppler Interferometry may be considered to analyze drops size.

During the Hot Fire tests campaign with glass window and methane as fuel, a rapid soot formation onto glass surface as been observed. This phenomenon could have influenced the Abel inverse transform results. An higher value of brightness has been registered in the near injection zone, which is physically unexpected. Further investigation is needed to prove that the code developed is suitable for the flame obtained with liquid oxygen as oxidizer. In alternative, splitting the flame image before the inflection point could lead to further clarification.

While dealing with the glass window, special attention has been kept. Longer time has been waited between two consecutive tests. Cooling phase of combustion chamber has been made to last longer to ensure lower temperatures. Particular attention in screwing the holding plate placed onto the window has been paid to prevent the breaking.

Despite the precautions, the Hot Fire tests campaign with glass window using H₂ as fuel could not be performed due to window breaking during last test with CH₄.

Appendix A

Uncertainty Analysis

A.0.1 Venturi mass flow rate uncertainty

According to Eq. (A.0.1), the mass flow rate is a function of upstream, downstream pressure and the density:

$$\dot{m} = f(p_{th}, p_{line}, \rho)$$

As pressure and temperature values are measured quantities, the uncertainty is calculated using the standard deviation, defined as:

$$s_T = \sqrt{\frac{1}{N-1} \sum_i^N (T_i - \bar{T})^2}$$

$$s_p = \sqrt{\frac{1}{N-1} \sum_j^N (p_j - \bar{p})^2}$$
(A.1)

where \bar{p}, \bar{T} are the mean of temperature and pressure values in the evaluated time interval. The mass flow uncertainty is calculated implementing the error propagation as followings:

$$\delta \dot{m} = \sqrt{\left(\frac{\partial \dot{m}}{\partial p_{line}} \cdot \delta p_{line} \right)^2 + \left(\frac{\partial \dot{m}}{\partial p_{th}} \cdot \delta p_{th} \right)^2 + \left(\frac{\partial \dot{m}}{\partial \rho} \cdot \delta \rho \right)^2}$$
(A.2)

Since the density depends on pressure and temperature, the error propagation is applied:

$$\delta \dot{m} = \sqrt{\left(\frac{\partial \rho}{\partial p_{line}} \cdot \delta p_{line} \right)^2 + \left(\frac{\partial \rho}{\partial T} \cdot \delta T \right)^2}$$
(A.3)

The density partial derivatives are computed with the finite difference method at second order:

$$\frac{\partial \rho}{\partial p} \approx \frac{\rho(p + \delta p, T) - \rho(p - \delta p, T)}{2 \cdot \delta p}$$
(A.4)

$$\frac{\partial \rho}{\partial T} \approx \frac{\rho(p, T + \delta T) - \rho(p, T - \delta T)}{2 \cdot \delta T}$$
(A.5)

The mass flow partial derivatives are computed deriving the mass flow equation (venturi incompressible):

$$\frac{\partial \dot{m}}{\partial p_{line}} \approx \frac{1}{2} \rho C_d A_{th} \sqrt{\frac{2}{\rho(1 - \beta^4)(p_{line} - p_{th})}}$$
(A.6)

$$\frac{\partial \dot{m}}{\partial p_{th}} \approx -\frac{1}{2} \rho C_d A_{th} \sqrt{\frac{2}{\rho(1 - \beta^4)(p_{line} - p_{th})}}$$
(A.7)

$$\frac{\partial \dot{m}}{\partial \rho} \approx \frac{1}{2} C_d A_{th} \sqrt{\frac{2 \cdot (p_{line} - p_{th})}{\rho(1 - \beta^4)}}$$
(A.8)

A.0.2 OF uncertainty

The oxidizer to fuel ratio is defined as follows:

$$OF = \frac{\dot{m}_{LOX}}{\dot{m}_f}$$

The OF uncertainty is defined as:

$$\delta OF = \sqrt{\left(\frac{\partial OF}{\partial \dot{m}_{LOX}} \cdot \delta \dot{m}_{LOX}\right)^2 + \left(\frac{\partial OF}{\partial \dot{m}_f} \cdot \delta \dot{m}_f\right)^2} \quad (\text{A.9})$$

The partial derivatives are computed deriving the OF equations:

$$\frac{\partial OF}{\partial \dot{m}_{LOX}} \approx \frac{1}{\dot{m}_f} \quad (\text{A.10})$$

$$\frac{\partial OF}{\partial \dot{m}_f} \approx -\frac{\dot{m}_{LOX}}{\dot{m}_f^2} \quad (\text{A.11})$$

Components

A.1 MoRaP

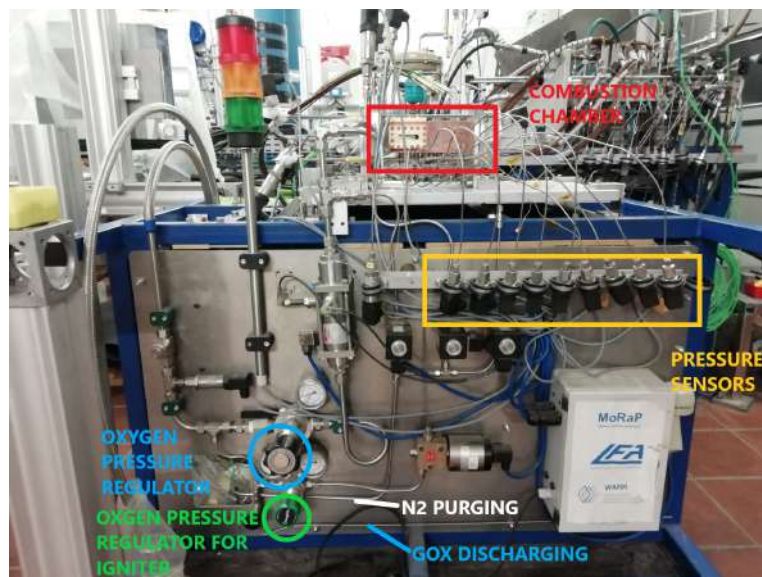
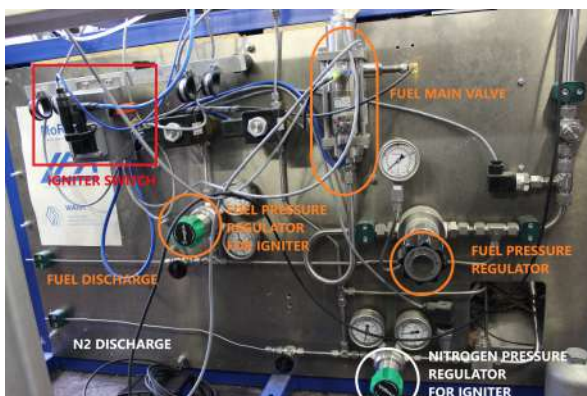


Figure A.1: MoRaP supply line: oxygen side.

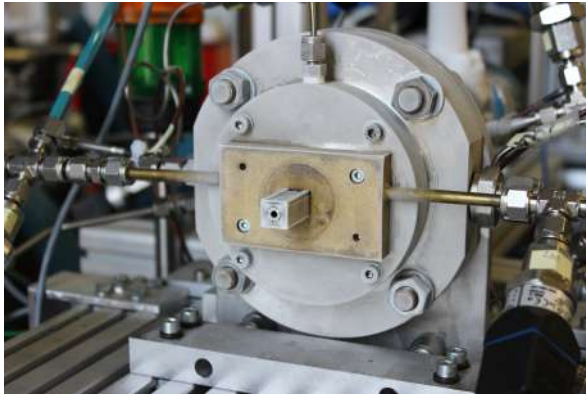


(a) MoRaP supply line: fuel side.

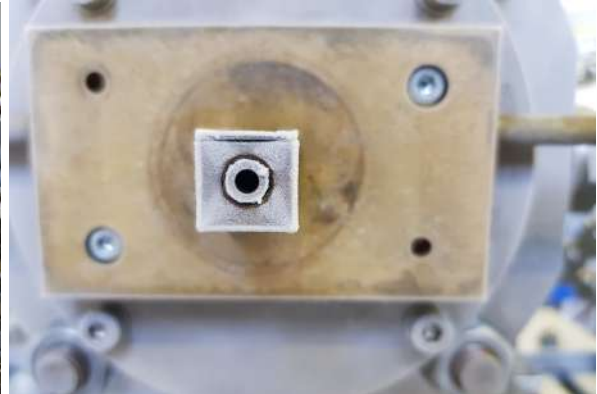


(b) Pressure setting.

A.2 Thrust chamber components

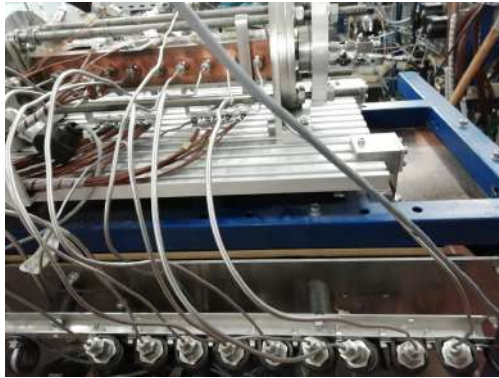


(c) Injector element and faceplate.



(d) Injector element and film applicator.

Figure A.2: Shear coaxial injector mounted with the injector head and faceplate during Cold Flow test.

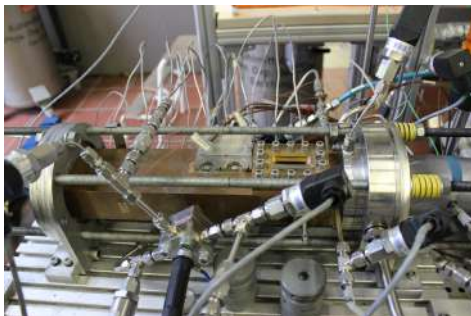


(a) Combustion chamber pressure sensors.



(b) Combustion chamber thermocouples.

Figure A.3: Measurements set up configuration.



(a) Combustion chamber complete set up.



(b) Detail of springs holding the combustion chamber.



(c) Igniter element mounted in the second position.



(d) Igniter switch.

Figure A.4: Igniter element and igniter switch.



(a) Thermocouples inserted into the cart module.



(b) Cart module inserted into MoRap.

Figure A.5: Thermocouples type T.

A.3 Calibration



Figure A.6: Calibration facility.

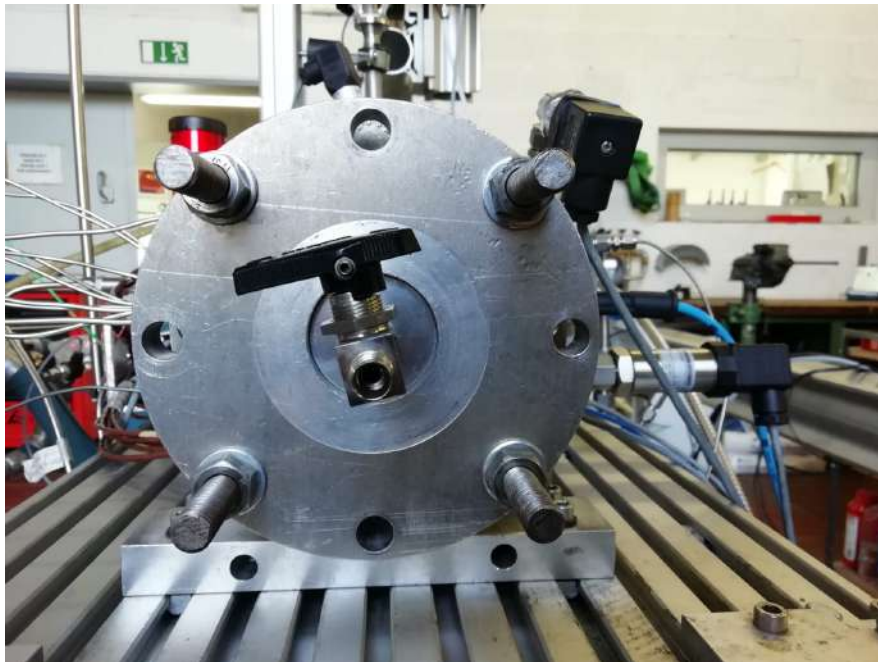
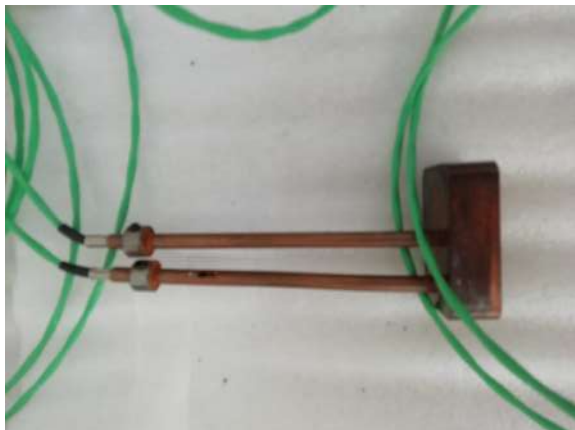


Figure A.7: Plug for pressurization.

A.4 Windows



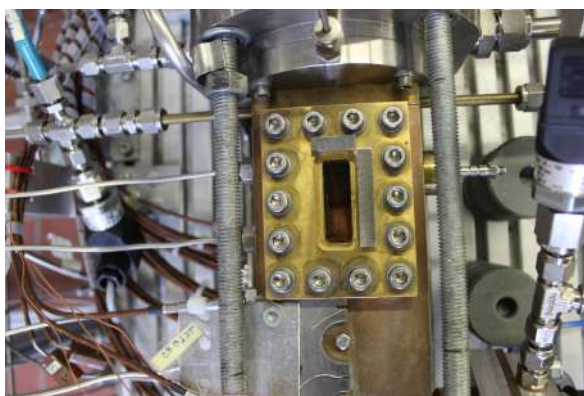
(a) Copper window.



(b) Screwing the window holding.



(c) Glass window.



(d) Window holding.



Figure A.8: Film applicator.

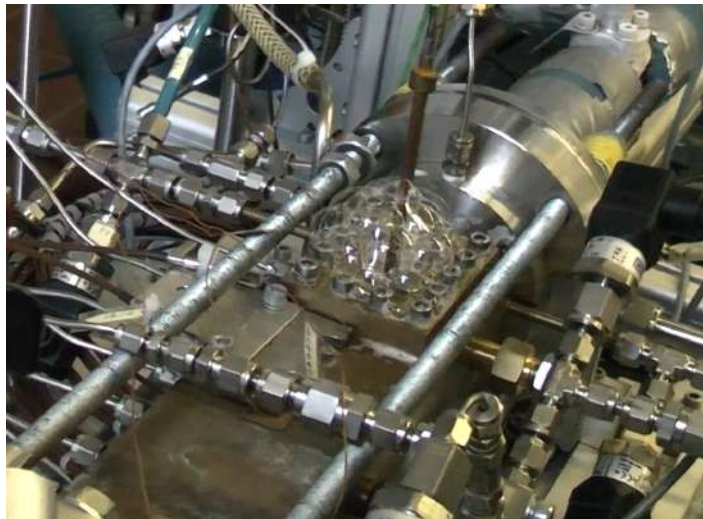


Figure A.9: Window leakage.



(a) Nozzle upstream section.

(b) Nozzle exit section.

Figure A.10: Nozzle truncated trapezoidal prism.



(a) Nozzle holding plate: upstream face.

(b) Nozzle holding plate: downstream face.

Figure A.11: Nozzle holding plate.

A.5 LOX supply line components



(a) Dismounted Venturi meter.



(b) Mounted Venturi meter.

Figure A.12: Venturi meter.



(a) LOX main valve.



(b) LOX supply valve.



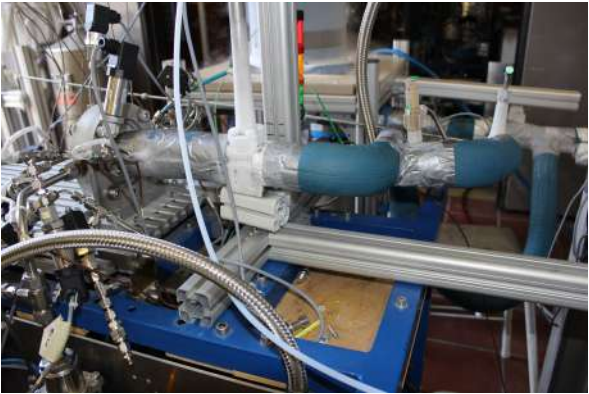
Figure A.13: LN2 check valve.



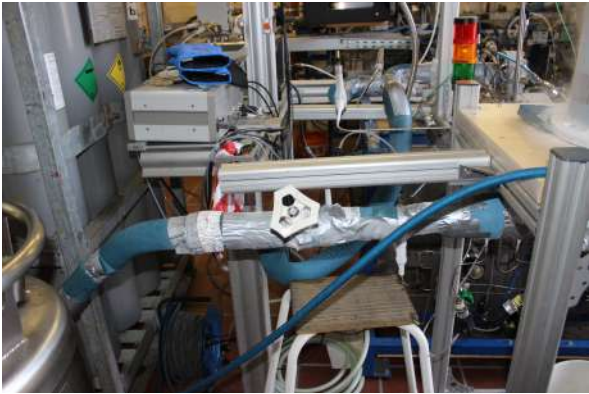
(a) Bypass valve.



(b) Bypass pipe.



(c) Insulation across the main valve.



(d) Insulation across the supply valve.



(e) Over pressure valve - Check valve - Release valve.



(f) LOX exit valve.

A.6 Complete Cold Flow Set Up

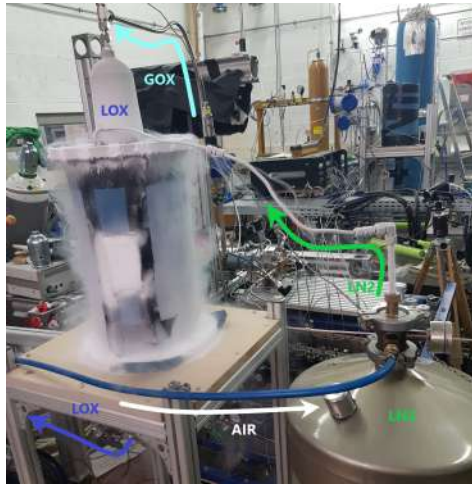


Figure A.14: Cold Flow complete set up.



Figure A.15: Control room.

A.7 Cold Flow Test Operating



(a) Liquification supply line.



(b) Liquifier filled with liquid nitrogen.

Figure A.16: Experimental set up for oxygen liquification.

(a) Closed set up.



(b) Open set up.

Figure A.17: Experimental set up for precooling with LN2.

A.8 Hot Fire

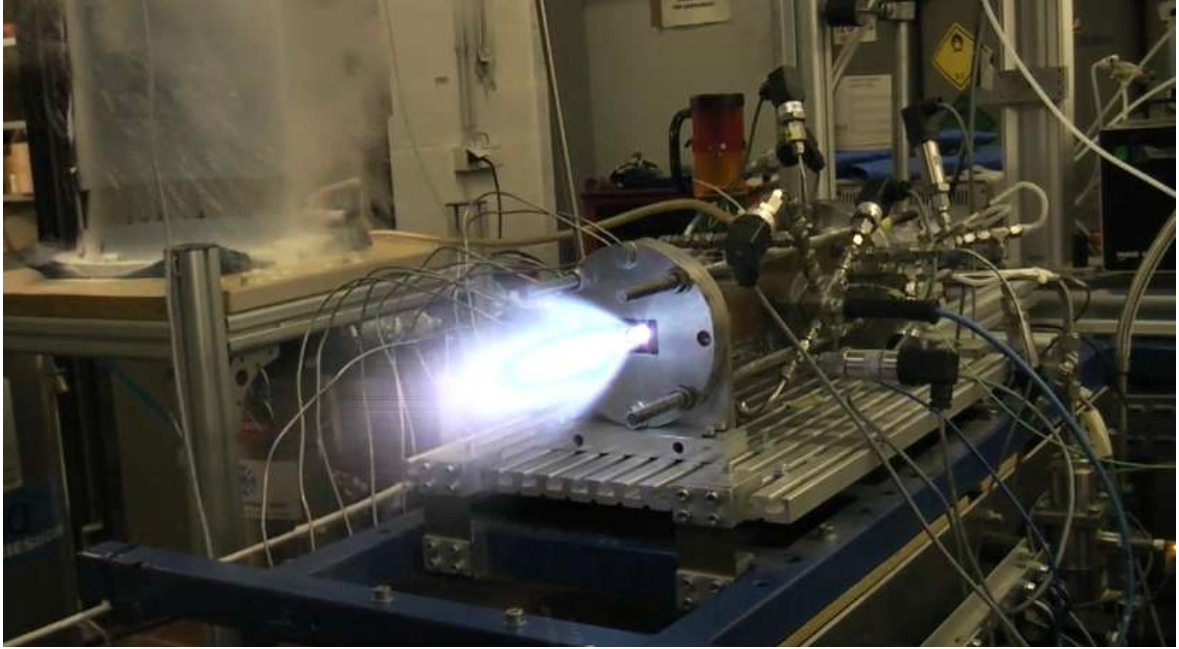


Figure A.18: Hot Fire test LOX/CH₄.

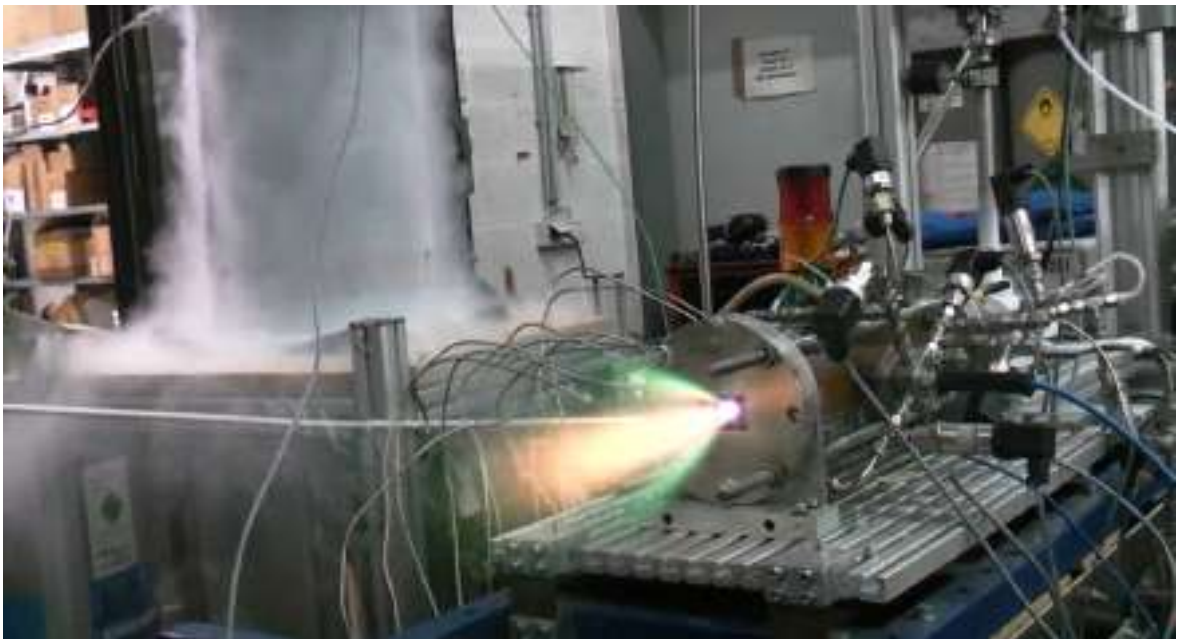


Figure A.19: Hot Fire test LOX/H₂.



(a) Glass window breaking during Hot Fire.

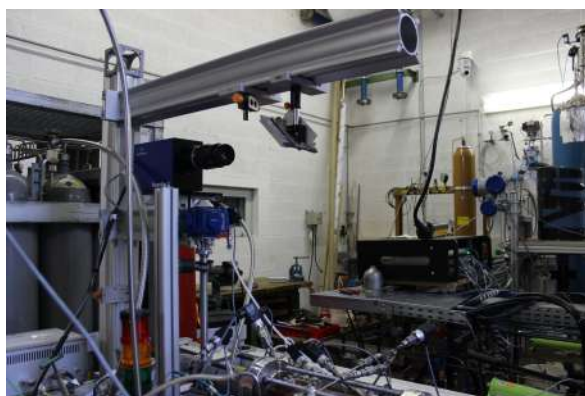


(b) Window breaking after Hot Fire test.

A.9 Optical Set Up



(c) Flame Star 2 camera.



(d) Optical Set Up.

Figure A.20: Experimental set up for precooling with LN₂.

Appendix B

Measurement Set Up

B.1 Thermocouples

	TYPE T
Material	Cu/CuNi
Inner diameter [mm]	0.5
Temperature Range [K]	233 ÷ 623
Color	Brown

Table B.1: Type T thermocouples.

	TYPE K
Material	CrNi/NiAl
Inner diameter [mm]	1
Temperature Range [K]	233 ÷ 1500
Color	Green

Table B.2: Type K thermocouples.

T	Thermocouple
C	Combustion chamber
L/S	Long Segment/Short Segment
U/O	Unten/Oben
First Digit	Axial Position
Last Digit	Distance from hot gas side

Table B.3: Thermocouples label.

B.2 Pressure sensor distribution

Description	z[mm]	Type	Maximum Pressure [bar]	Output
PC0		A10 WIKA	40	0 - 10 V
PC1		A10 WIKA	40	0 - 10 V
PC2		A10 WIKA	60	0 - 10 V
PC3		A10 WIKA	40	0 - 10 V
PC4		A10 WIKA	40	0 - 10 V
PC5		A10 WIKA	40	0 - 10 V
PC6		A10 WIKA	40	0 - 10 V
PC7		A10 WIKA	40	0 - 10 V
PC8		A10 WIKA	40	0 - 10 V

Table B.4: Pressure sensors position within the combustion chamber.

B.3 Window Set up

GLASS WINDOW	
Material	Quartz Glass Silux
Dimensions [mm]	49.5x32.5x14.8
Company	Sico Technology GmbH
Color	Brown

Table B.5: Glass window specifications.

Part	Number of pair	Foil Thickness [mm]
Bottom	1	0.21
Side	1	0.26
Front/Back	1	0.26

Table B.6: Graphite foils instruction for copper window.

Part	Number of pair	Foil Thickness [mm]
Bottom	1	0.21
Bottom	2	0.26
Side	1	0.26
Front/Back	1	0.26

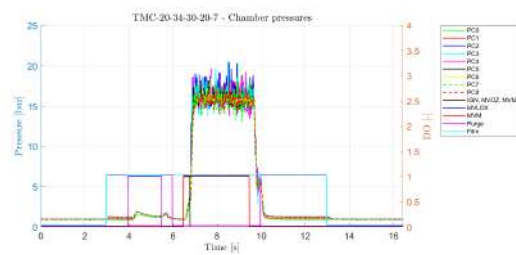
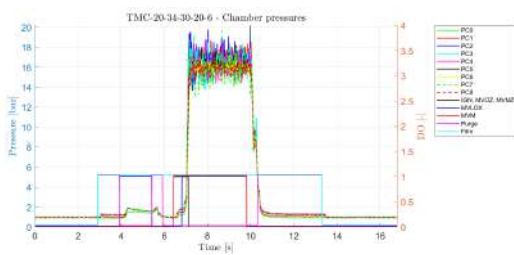
Table B.7: Graphite foils instruction for glass window.

Ignition Sequence

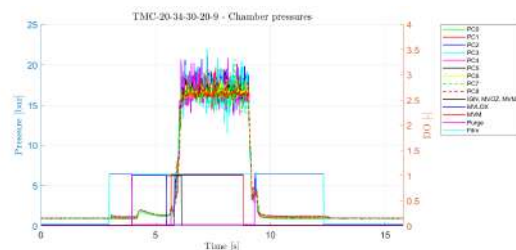
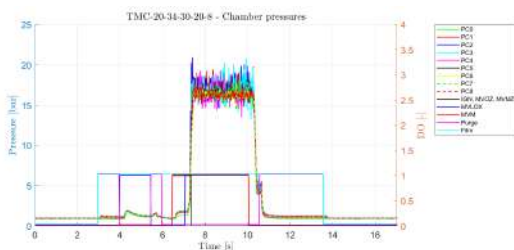
The ignition sequence is divided in three intervals:

1. Start up and ignition;
2. Main combustion;
3. Shutdown.

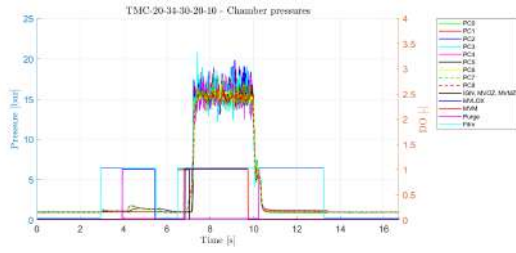
The duration of each valve opening time has been modified to achieve a stable combustion. The following plots present the different combination of sequences compared with the obtained combustion pressure for methane tests with copper window.



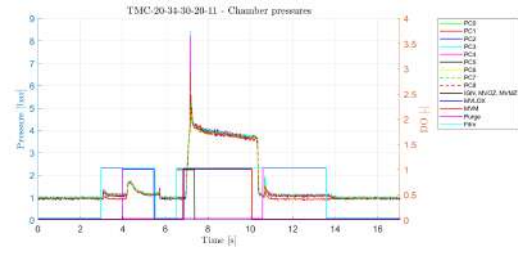
(a) TMC-20-34-30-20-6: Igniter and methane at same time. (b) TMC-20-34-30-20-7: Igniter and oxygen at same time.



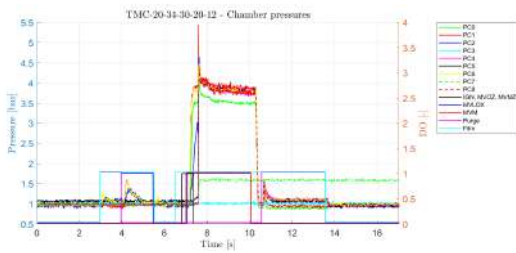
(c) TMC-20-34-30-20-8: Delay between methane and (d) TMC-20-34-30-20-9: Shorter delay between methane and oxygen.



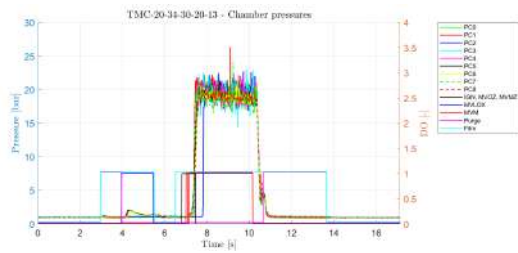
(e) TMC-20-34-30-20-10: Film cooling shut off and on.



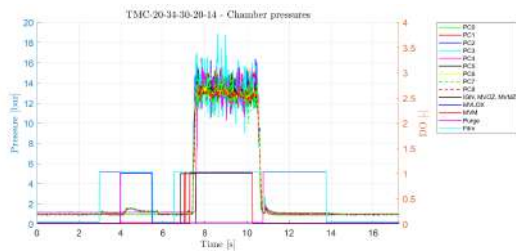
(f) TMC-20-34-30-20-11: Igniter dealy - No ignition.



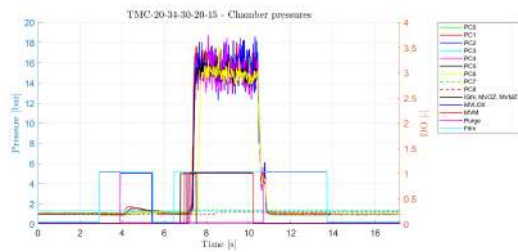
(g) TMC-20-34-30-20-12: Igniter and fil cooling shut off and



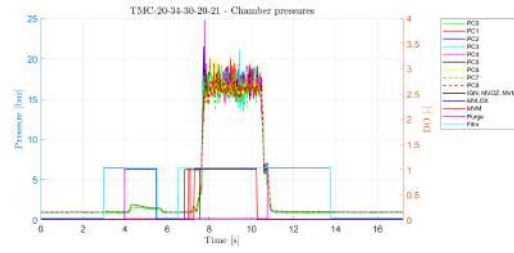
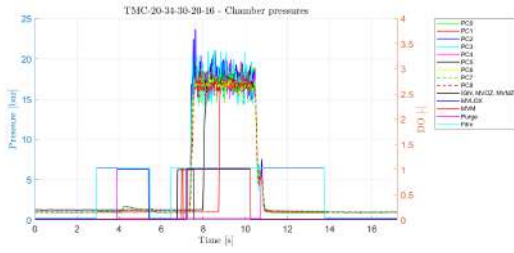
(h) TMC-20-34-30-20-13: Methane shut off and on. Film cooling shut off and on.



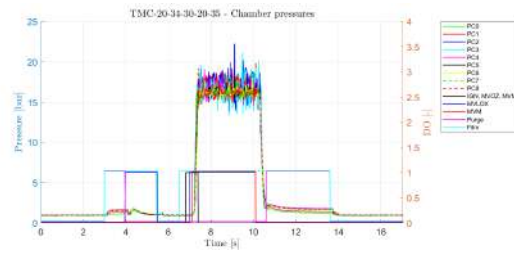
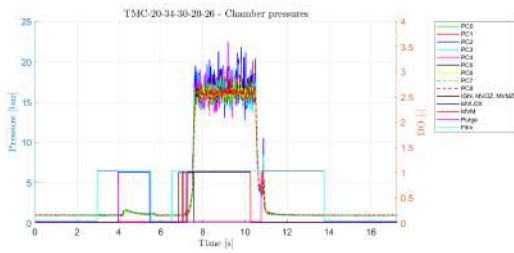
(i) TMC-20-34-30-20-14: Longer delay in methane shut off and on.



(j) TMC-20-34-30-20-9: LOX opening between methane shut off and on.



(k) TMC-20-34-30-20-16: Longer delay for LOX opening (l) TMC-20-34-30-20-21: Methane shut off and on with igniter changed position.



(m) TMC-20-34-30-20-26: Methane shut off and on with cylinder. (n) TMC-20-34-30-20-35: Methane after LOX.

LabView

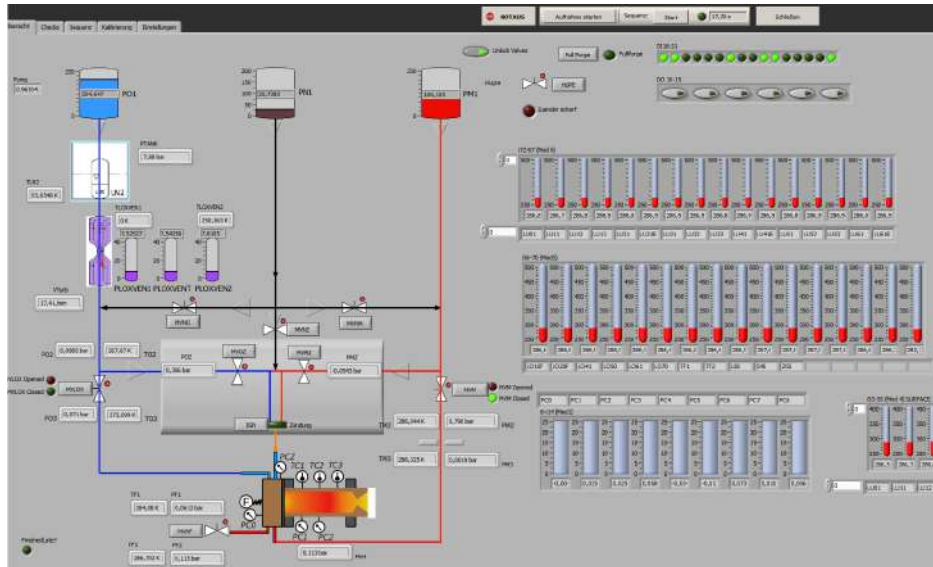


Figure B.1: Labview tool.

```

P01 0.000000 0.000000 35.000000 -0.500000
vturb 0.000000 0.000000 1.000000 0.000000
PM1 0.000000 0.009589 24.981631 -0.674511
PM3 0.000000 0.008300 3.950000 -0.084100
PM1 0.000000 0.007584 25.016769 -0.850579
PM2 0.000000 0.006270 9.974375 -0.239389
PC0 0.000000 0.001755348 3.99206337 -0.083617214
PC1 0.000000 0.000458128 4.002102968 -0.6000000
PC2 0.000000 -0.004803169 7.54441265 -15.11119709
PC3 0.000000 0.000508087 4.002730579 -0.124511745
PC4 0.000000 0.001125834 4.000023794 -0.070765982
PC5 0.000000 0.001997615 3.990394011 -0.197754166
PC6 0.000000 0.002210579 3.99085908 -0.101066621
PC7 0.000000 0.00015288 4.007525288 -0.160974355
PC8 0.000000 0.000506775 4.00465872 -0.079263995
P115 0.000000 0.000000 3.030300 -0.303000
P116 0.000000 0.000000 1.000000 0.000000
P117 0.000000 0.000000 1.000000 0.000000
P118 0.000000 0.000000 1.000000 0.000000
P119 0.000000 0.000000 1.000000 0.000000
P120 0.000000 0.000000 1.000000 0.000000
PF1 0.000000 0.002600 9.996900 -0.222000
PLOXVENT 0.000000 0.004700 5.973400 -0.242300
PLOXVEN1 0.000000 0.005400 4.970600 -0.118200
Pump 0.000000 0.000000 0.060000 0.800000
P125 0.000000 0.000000 1.000000 0.000000
P126 0.000000 0.000000 1.000000 0.000000
P127 0.000000 0.000000 1.000000 0.000000
P128 0.000000 0.000000 1.000000 0.000000
P129 0.000000 0.000000 1.000000 0.000000
P130 0.000000 0.000000 1.000000 0.000000
P131 0.000000 0.000000 1.000000 0.000000
PO2 0.000000 -8712.500000 6400.700000 -25.555000
PO3 0.000000 31876.000000 5971.200000 -24.360000
PM2 0.000000 1301.900000 3102.800000 -12.344000
PM4 0.000000 -3383.400000 6325.900000 -24.912000
PM4 0.000000 1290.300000 3735.000000 -15.356000
PLOXVEN2 0.000000 12355.000000 3555.200000 -14.420000
PF2 0.000000 -15612.000000 2741.400000 -10.718000
PTANK 0.000000 -21266.000000 4708.800000 -18.639000
    
```

Figure B.2: Calibration data file .txt: input to LabView.

Bibliography

- [1] Sanford Gordon and Bonnie J McBride. *Computer program for calculation of complex chemical equilibrium compositions and applications*. 1994.
- [2] David Greatrix, Ivett Leyva, Dario Pastrone, Valsalayam Sanal Kumar, and Michael Smart. Chemical rocket propulsion. *International Journal of Aerospace Engineering*, 2012, 2012.
- [3] G.P. Sutton and O. Biblarz. *Rocket Propulsion Elements*. John Wiley & Sons, 1994.
- [4] SS Penner. Similarity analysis for chemical reactors and the scaling of liquid-fuel rocket engines. Technical report, CALIFORNIA INST OF TECH PASADENA GUGGENHEIM JET PROPULSION CENTER, 1954.
- [5] D Haeseler, V Bombelli, P Vuillermoz, R Lo, T Marée, and F Caramelli. Green propellant propulsion concepts for space transportation and technology development needs. In *ESA Special Publication*, volume 557, 2004.
- [6] Eads signs kerosene research deal with russians. *Flight International*, 2003.
- [7] Holger Burkhardt, Martin Sippel, Armin Herbertz, and Josef Klevanski. Kerosene vs. methane: A propellant tradeoff for reusable liquid booster stages. *Journal of Spacecraft and Rockets*, 41(5):762–769, 2004.
- [8] William M Marshall and Julie E Kleinhenz. Hot-fire testing of 100 lb (sub f) lox/lch4 reaction control engine at altitude conditions. 2010.
- [9] Shuichi Ueda, Takeo Tomita, Takuo Onodera, Yasuhito Kano, Isao Kubota, and Takao Munenaga. *Hot-Firing Test of Methane-Fueled Rocket Engine under High Altitude Condition*.
- [10] Richard Strunz, Gerald Hagemann, Frank Grauer, Ludwig Brummer, Dieter Preklik, Eric Biojoux, Xavier Viot, Gilles Dantu, Ubaldo Staffilano, Franscesco Cuoco, and Massimo Santilli. Main stage liquid propulsion activities within europe’s future launcher preparatory programme flpp. 07 2006.
- [11] S.R. Turns. *An Introduction to Combustion: Concepts and Applications*. McGraw-Hill Education, 2011.
- [12] Fernanda Winter, Nikolaos Perakis, and Oskar J Haidn. Emission imaging and cfd simulation of a coaxial single-element gox/gch4 rocket combustor. In *2018 Joint Propulsion Conference*, page 4764, 2018.
- [13] Jin Ping, Li Mao, and Cai Guo-Biao. Numerical and experimental study on shear coaxial injectors with hot hydrogen-rich gas/oxygen-rich gas and gh2/go2. *Chinese Physics B*, 22(4):044701, 2013.
- [14] C. Pauly, J. Sender, and M. Oswald. *Ignition of a Gaseous Methane/Oxygen Coaxial Jet*, volume 1, pages 154–170. 09 2009.
- [15] Luc Potier. *Large Eddy Simulation of the combustion and heat transfer in sub-critical rocket engines*. PhD thesis, 2018.
- [16] S.S. Penner and P.P. Datner. Combustion problems in liquid-fuel rocket engines. *Symposium (International) on Combustion*, 5(1):11 – 29, 1955.

- [17] Robert Kenny, Marlow Moser, James Hulka, and Gregg Jones. Cold flow testing for liquid propellant rocket injector scaling and throttling. volume 5, 07 2006.
- [18] Simona Silvestri, Maria P Celano, Christoph Kirchberger, Gregor Schlieben, Oskar Haidn, and Oliver Knab. Investigation on recess variation of a shear coax injector for a single element gox-gch4 combustion chamber. *Transactions of the Japan Society for Aeronautical and Space Sciences, Aerospace Technology Japan*, 14:13–20, 2016.
- [19] Maria Palma Celano, Simona Silvestri, Christian Bauer, Nikolas Perakis, Gregor Schlieben, and Oskar J. Haidn. *Comparison of single and multi-injector GOC/CH₄ combustion chambers*.
- [20] Simona Silvestri, Maria Palma Celano, Gregor Schlieben, and Oskar J. Haidn. *Characterization of a Multi-Injector GOX/CH₄ Combustion Chamber*.
- [21] Brunno Barreto Vasques. *Development of a Rocket Engine Injection System with Throttling Capability Based on the LO₂/LCH₄ Propellant Combination*. Dissertation, Technische Universität München, München, 2019.
- [22] Nikolaos Perakis, Maria Palma Celano, and Oskar J Haidn. Heat flux and temperature evaluation in a rectangular multi-element gox/gch4 combustion chamber using an inverse heat conduction method. In *7th European Conference for Aerospace Sciences*, 2017.
- [23] COMBUSTION DIAGNOSTICS. *Advanced Optical Measurement Solutions*. Number 247-v5. Dante Dynamics and Nova Instruments.
- [24] Thomas Fiala. *Radiation from high pressure hydrogen-oxygen flames and its use in assessing rocket combustion instability*. PhD thesis, Technische Universität München, 2015.
- [25] Pasquale Difficile. *Performance and Emission Imaging of a Coaxial Single Element GO₂/GCH₄ Rocket Combustion Chamber*. PhD thesis, Politecnico di Torino, 2018.
- [26] Graziano Laera. *Emission Imaging of a Coaxial Single Element GOX/GH₂ Rocket Combustion Chamber*. PhD thesis, Politecnico di Torino, 2018.
- [27] R.N. Bracewell. *The Fourier Transform and its Applications*. McGraw-Hill Kogakusha, Ltd., Tokyo, second edition, 1978.
- [28] Georg Pretzier. A new method for numerical abel-inversion. *Zeitschrift für Naturforschung A*, 46(7):639–641, 1991.
- [29] Simona Silvestri. *Investigation on Heat Transfer and Injector Design Criteria for Methane/Oxygen Rocket Combustion Chambers*. PhD thesis, Technische Universität München, 2019.